This is to certify that the

dissertation entitled

"Scanning Tunneling Microscope Study of Surface Diffusion and Dislocation Motion in Atomically Flat Gold Films"

presented by

Jeeseong Hwang

has been accepted towards fulfillment
of the requirements for

Ph.D. degree in Physics

M. Dubson
Major professor

Date March 17, 1993

SCANNING TUNNELING MICROSCOPE STUDY OF SURFACE DIFFUSION AND DISLOCATION MOTION IN ATOMICALLY FLAT GOLD FILMS

By

Jeeseong Hwang

A DISSERTATION

Submitted to
Michigan State University
in partial fulfillment of the requirements
for the degree of

DOCTOR OF PHILOSOPHY

Department of Physics and Astronomy

1993

ABSTRACT

SCANNING TUNNELING MICROSCOPE STUDY OF SURFACE DIFFUSION AND DISLOCATION MOTION IN ATOMICALLY FLAT GOLD FILMS

By

Jeeseong Hwang

A simple scanning tunneling microscope (STM) which works well from room temperature to 4K is described. It is relatively easy to build, repair or modify, and works very reliably. With this STM, we study mass flow on (111)Au and find that the rate of decay of the area of monolayer islands produced by STM lithography is linear in time. We demonstrate by Monte Carlo simulations that a proper accounting of the detachment and reattachment rates of kink site atoms produces a linear decay. To observe the decay rate of a monolayer gold island, one needs a sample with large isolated grains with large facets showing atomically flat terraces separated by monatomic steps. We find that thermal evaporation of Au onto heated glass substrates satisfies these conditions. At room temperature in air, these films show low angle grain boundaries and other dislocation arrays which move under an applied stress introduced either by handling the sample or by crashing an STM tip on the sample surface.

To my parents

ACKNOWLEDGEMENTS

I wish to thank Michael A. Dubson for his invaluable guidance, inspiration, assistance, and encouragement as a supervisor, a teacher, and a friend in all aspects of my graduate years. In, particular, he taught me how to create exciting, and enjoyable moments out of long and dry-looking physics. I thank Professors Norman Birge, Phillip Duxbury, William Hartmann, and Michael Thoennessen for serving on my graduate committee.

There are several people to whom I owe acknowledgement: Martine Kalke for writing the Monte Carlo simulation program for the cubic lattice solid-on-solid model; the machine shop staff, Thomas Palazzolo, Jim Muns, and Tom Hudson for their assistance in construction of experimental apparatus and in teaching me machine shop skills; Electronic shop staff, Barry Tigner and Bob Raine for their technical support in building electronics and cleaning notorious viruses in my PC; Reza Loloee for his efforts to teach various measurement skills and organize a hazard-free chemical room.

I would like to extend my thanks to my fellow graduate students; Qifu Zhu, for useful conversations regarding experiments and sharing the spirit of the orient; Lowell McCann who is a creative participant in the 'STM next generation', for his assistance of measurements, useful discussions in small particle experiments and critical proof reading of this manuscript; George Jeffers, for divulging his own secrets in making thin films and careful reading of this thesis; Sangil Hyun, for drawing the STM shop drawings in the appendix; and all the graduate students in department.

I am also grateful for the encouragement and support that I received from my parents, parents-in-law, brothers and sisters. Their many prayers and support on my behalf are appreciated.

My special thanks go to my wife, Miyoung for her prayers, patience, sacrifice, and love over the last six years.

Finally, I want to thank MSU and the National Science Foundation for financial support during my graduate studies.

TABLE OF CONTENTS

LIST OF TABLES

LIST OF FIGURES

Chapter 1

INTRODUCTION

Atomic resolution observations of mass flow on a metal surface provide important clues about the microscopic mechanism of surface self diffusion. Direct 3-D observations of diffusing atoms or molecules on metal surfaces have been accomplished using a Field Ion Microscope (FIM), Scanning Tunneling Microscope (STM), and Atomic Force Microscope (AFM). A direct measurement of the surface self diffusion coefficient can be made by observing the motion of an individual atom diffusing on an atomically flat surface. If the surface is ideal the atomistic motion can be considered as a 2-D random walk amongst sites separated by potential barriers.

At room temperature in air, however, the motion of the individual atom is too fast to observe with an STM. Another technical problem for the observation of individual atoms is that it is very hard to obtain atomic resolution in air due to surface contamination. Instead, in this research, the surface self diffusion coefficient is measured from sequential STM images which show wandering monatomic steps or from the shape change of a gold mound.

At room temperature in air, we also observe that the area of single monolayer gold island decays linearly with time. A linear decay of island is puzzling at first sight. If the rate of mass loss is proportional to the circumference of the island then the decay is parabolic, not linear. We have found, by Monte Carlo simulations, that a proper accounting of the kink atom detachment and reattachment rates leads to a linear decay.

To observe the decay rate of a monolayer gold island, one needs a sample with grains with large facets showing atomically flat terraces separated by monatomic steps.

Gold films evaporated on hot glass satisfy these conditions. One might be tempted to assume that epitaxial growth is a requirement for making atomically flat films. But our results for Au on amorphous glass substrates show that epitaxy is definitely not necessary for the production of large, flat regions.

In our experiment, since not every layered structure created by the evaporation undergoes surface diffusion, we lithographically fabricated small mounds or islands with an STM using the voltage pulse technique. There are several advantages to making small structures artificially. First, in most cases, we can expect the features to change because they are in a metastable state. Secondly, a small system is desirable so that we can collect enough data in a short period of time before the STM image degrades due to build-up of surface contamination. Thirdly, a system of appropriately small size can be exactly modeled by the Monte Carlo simulation with the limitations in array size.

During this surface self diffusion measurement, low angle grain boundaries and other dislocation arrays were observed. We also found that these low angle grain boundaries move under an applied stress introduced either by handling the sample or by crashing an STM tip on the sample surface. These dynamic features usually accompany a deformation of part of the sample.

In a perfect crystal, atoms are arranged in a regular periodic pattern. However, in the real world, a crystal may contain various kinds of defects such as point defects (impurities, vacancies, etc.) and line defects (edge dislocations, screw dislocations). Since the macroscopic behavior of crystalline solids strongly depends upon the species and number of defects, an understanding of defects in a crystal is very important. For irreversible plastic deformation of a crystalline solid, it is well known that the deformation is induced by the atoms sliding over one another along a well-defined slip plane instead by uniform shearing of the crystal. Some characteristics of observed dislocations can be explained by this model.

Originally, before this subject of surface self diffusion drew our attention, our principle goal was investigating discrete charging and quantum size effects in single small metal particles with the STM. This investigation involves the attempt to correlate the I-V characteristics of various tunneling junctions which include a small metal particle and the STM tip.

The understanding of the electronic properties of small pieces of metal is a subject of growing importance as the microelectronics industry pushes toward smaller and smaller circuitry. As the size of a block of metal diminishes, new effects, not visible in large samples, arise and eventually dominate the simple ohmic metallic behavior. Some important I-V curves including the Coulomb Staircase at room temperature and the Coulomb Blockade at T = 83K were obtained.

For this study, we built a STM which works reliably from room temperature to 4K. The design and construction of our STM is described in Chapter 2. Let us briefly discuss the basic concept of STM before we close this chapter.

A STM can provide direct images of conducting surfaces with atomic resolution. A STM consists of a sharp metal tip held several angstroms above a sample surface by piezoelectric ceramic supports. An applied voltage between the sample surface and tip results in a tunneling current which depends exponentially on the tip-to-sample distance. With a tunneling barrier height of a few electron-volts, a change of the tunneling barrier width by one angstrom changes the tunneling current by an order of magnitude.

A STM can be operated in either the topographic mode (constant current mode) or the current mode (constant height mode). In the topographic mode, as the tip is scanned over the surface by the piezo supports, feedback electronics hold the tunneling current constant by adjusting the tip-sample distance. The resulting plot of tip height vs. position is a map of the electronic wavefunctions on the sample surface. Alternatively, in the current mode a tip is scanned over the surface at constant height while the current

is monitored. In this mode the variations in tunneling current due to surface corrugation are mapped vs. tip position. Each mode has its own advantages. The topographic mode gives direct topographic information of the surface over large structure and rough surfaces. On the other hand, current mode allows faster scans for relatively flat surfaces so that the fast imaging minimizes noise due to thermal drift, vibration and piezo creep. Consequently, this current mode is usually used for obtaining images with atomic resolution.

STM is also capable of doing spectroscopic measurements to observe surface or subsurface electronic properties. The applicable subjects involve characterization of superconductors, phonon spectroscopy, quantum size effects, etc.

Chapter 2

THE MICROSCOPE

Simple, Variable Temperature Scanning Tunneling Microscope

2.1 ABSTRACT

We describe a simple scanning tunneling microscope (STM) which works well from room temperature to 4K. It is relatively easy to build, repair or modify, and works very reliably. An unusual feature of our STM is that it is assembled without glues or solders. A list of suppliers of the components used in our STM is included in the references.

2.2 INTRODUCTION

Several designs for variable-temperature and low-temperature scanning tunneling microscopes (STM's) have been published.[1,2,3,4] In this chapter, a single-tube STM with a differential spring coarse-approach mechanism, similar to that described in ref.1 is described. The instrument, shown in Figure 2.1, has a box-shaped body, chosen for ease of machining and so that the microscope can be quickly disassembled for repair or replacement of any component. The schematic diagram of entire STM setup is given in Figure 2.2 and the shop plans of STM body is shown in Appendix A. Our STM has the unusual feature that it is constructed without glues or solders, and it functions very reliably in the temperature range 4-300K.

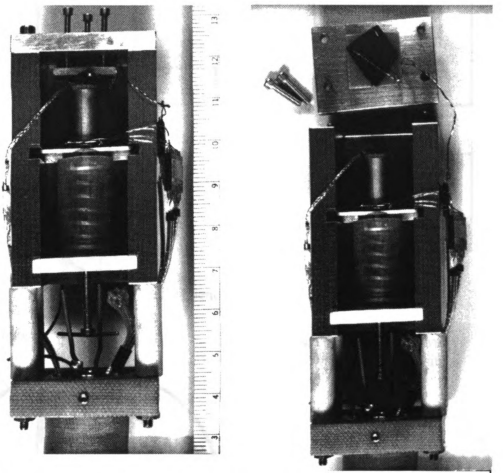

Figure 2.1 Photographs of the STM. The scale on the ruler is centimeters. (a) fully assembled. (b) with sample stage removed for easy sample loading.

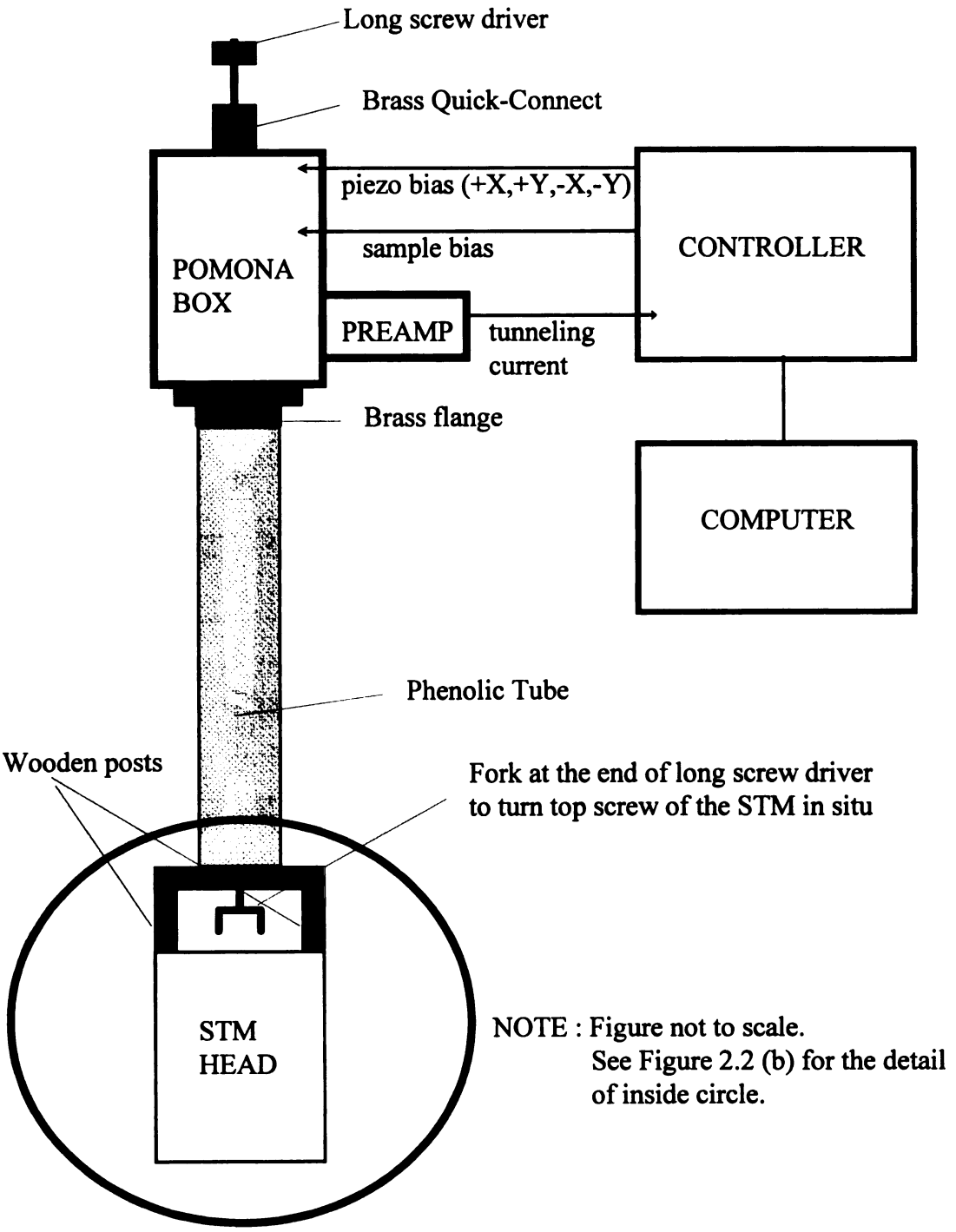

Figure 2.2 (a) Schematic diagram of the STM setup

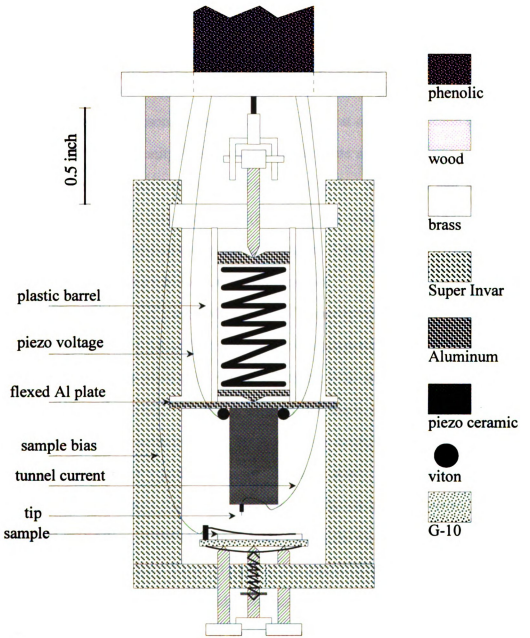

Figure 2.2 (b) Schematic diagram of the STM head

2.3 DESIGN AND CONSTRUCTION

The differential spring coarse-approach mechanism consists of a steel spring pressing against a 1/16" thick aluminum plate supported along two edges. Aluminum, rather than steel, was chosen for the plate because, for a given spring constant, an aluminum plate has a resonant frequency twice as great as that of a steel plate, resulting in better vibration immunity.[5] The motion of the plate and tunneling tip is about 3 μm per turn of the 2-64 screw at the top of the STM body. The screw and the screw plate must be made of the same material (brass, in our case) to avoid binding at low-temperature due to differential thermal contraction. A plastic barrel surrounds the spring to prevent transverse movement during compression.

The main body of the STM is made of Super-Invar[6], a Fe-Ni alloy which has a near-zero coefficient of thermal expansion at room temperature[7]. The thermal expansion coefficient of Invar is plotted in Figure 2.3 along with several different metals in the temperature range 0-300K. In earlier designs, we made the STM body of aluminum, chosen for ease of machining, and because Al is strong and light, with a (Young's modulus/density) ratio equal to that of stainless steel. The aluminum body STM functioned very well both at room and cryogenic temperatures. However, during cooling to <100K, contraction of the aluminum body causes the tip-sample distance to shrink by more than 60μm, requiring about 20 turns of the coarse-approach screw to keep the tip in tunneling range. With the Invar body, on cooling from room to cryogenic temperatures, the tip-sample distance increases by about 20μm, due to contraction of the sample stage and the piezo tube The increase of the tip-sample gap due to cooling is plotted in Fig 2.4. Not only is the thermal drift much reduced, but the increasing tip-sample distance upon cooling reduces the possibility of tip crash.

A difficulty with Super-Invar is that it is available only in 3/4" thick plate[8] which

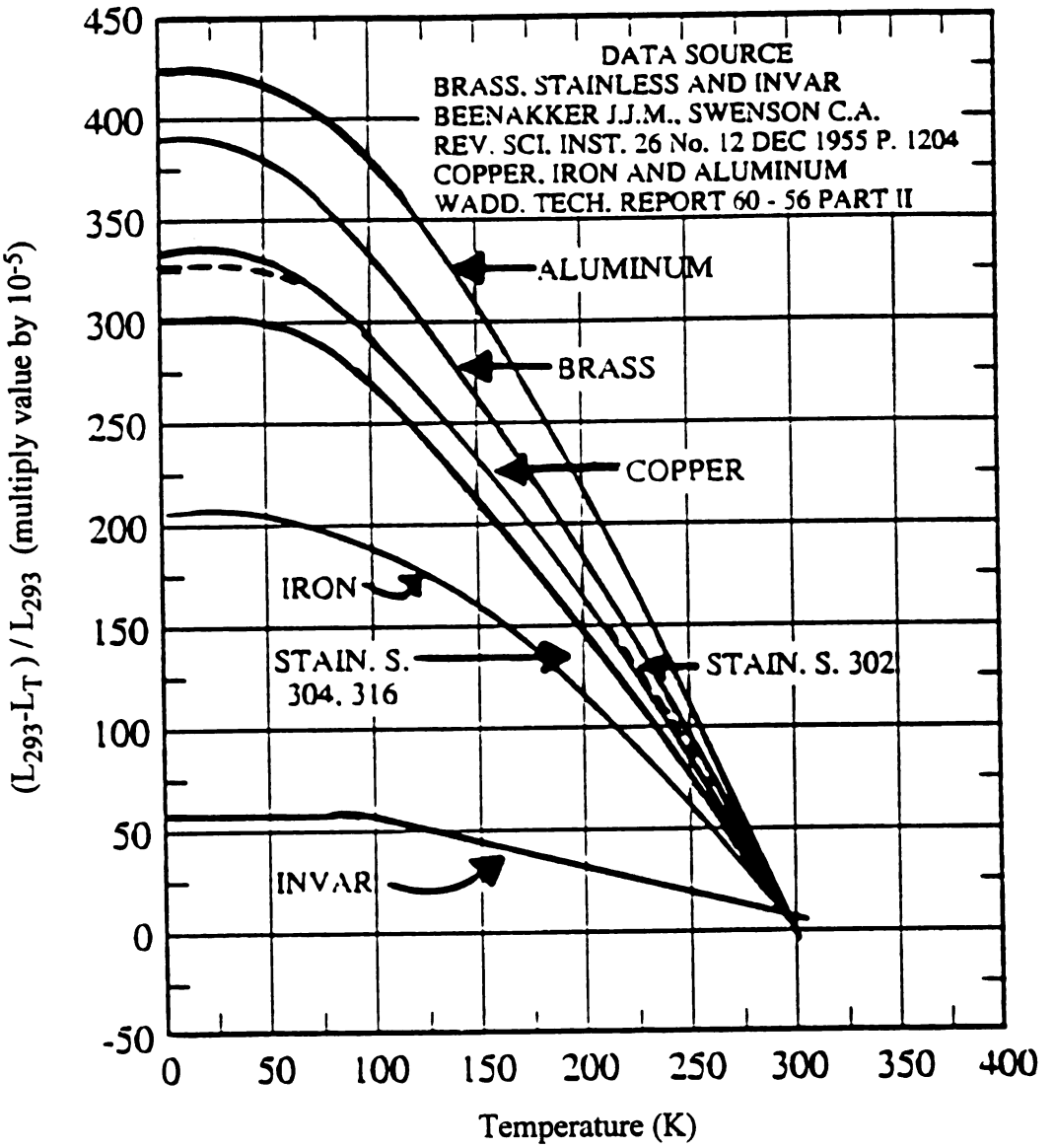

Figure 2.3 Thermal expansion coefficients of Invar and other metals.

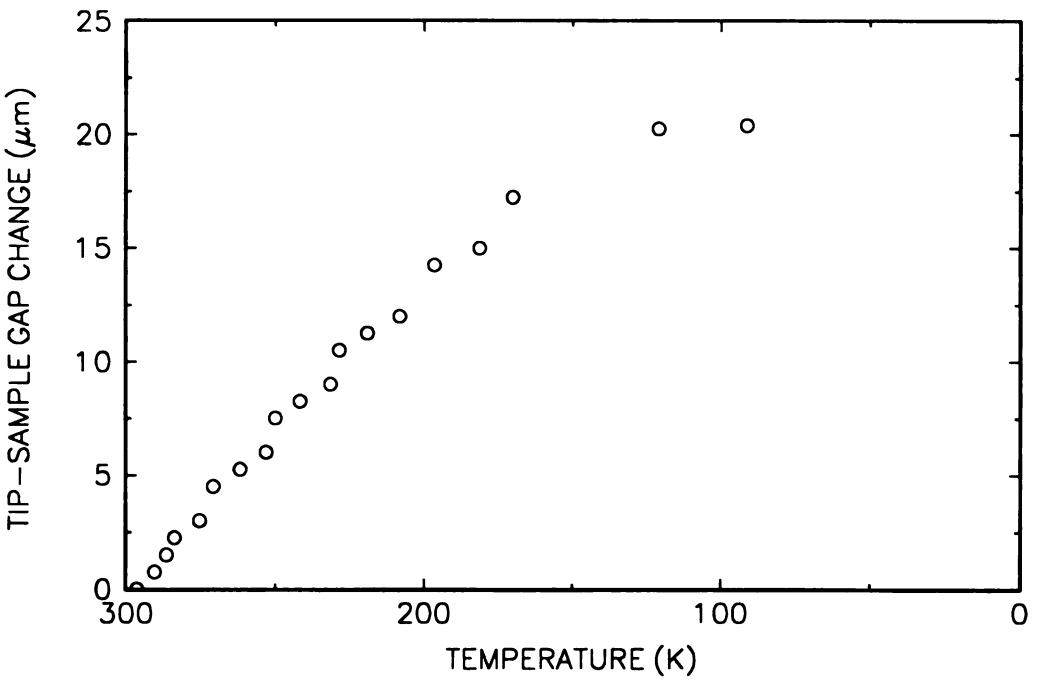

Figure 2.4 Tip-sample gap change on cooling the invar-body STM. The tip-sample separation increases during cool-down.

must be sliced up into thinner plates. This job is best performed with an electrical discharge wire cutter. Another drawback of this Fe-Ni alloy is that it is ferromagnetic, which complicates any magnetic field work.

The sample stage is made of G-10 (ref. 9), fiber glass and epoxy compound which has a high value of (Young's modulus/density) ratio. At the corner of the sample stage a 10 mil brass wire clip is clamped with 0000-160 miniature bolt and nuts[10]. The clip holds the sample in place and provides electrical contact for the bias voltage. The sample stage is attached to the bottom plate of the STM body by the following mechanism.: Three 2-64 stainless steel screws in the bottom plate support the sample stage while a fine steel spring[11] holds the stage and the bottom plate together. Initial coarse-coarse approach is performed by advancing those three screws independently while monitoring the tip-sample gap with an optical microscope. A diagram of the sample stage is shown in Figure 2.2 (b). A modification of the sample stage for a cryogenic UHV system is discussed in chapter 8.

The 1/2" long, 1/4" diameter piezoelectric-ceramic tube[12] has a response of 95Å/V in x,y motion, 47Å/V in z motion, and a maximum x-y range of about ±1μm at room temperature. The x-y motion is calibrated by imaging graphite; the z motion is calibrated by imaging monatomic steps on (111) gold (see Figure 2.5 and Figure 2.6) The x-y response drops to 33Å/V at 77K and to about 12Å/V at 5K[13]. The reduced piezoelectric response at cryogenic temperatures increases the probability of tip crash during the final mechanical approach. To improve the sensitivity of the mechanical approach, the plate in the differential spring mechanism can be easily replaced with a slightly thicker one. (The spring constant of a plate rises as the cube of the plate thickness.)

Figure 2.7 is a photograph of the piezo lead attachment scheme. Each of the four piezo leads consists of a length of number 30 poly-thermaleze coated Cu wire which is

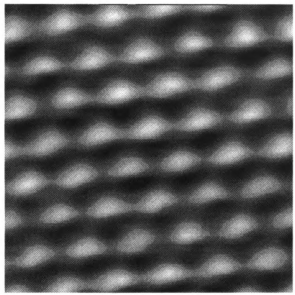

Figure 2.5 16Åx16Å scan of graphite at 77K. Topographic mode, current = 1.0nA, bias = +0.41V

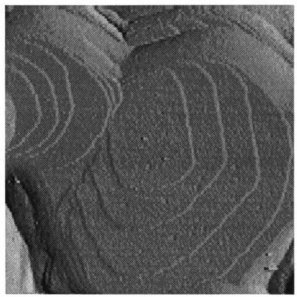

Figure 2.6 250nmx250nm scan of Au(111) at room temperature showing monatomic steps of 2.4Å. Tunneling current = 1.0nA, sample bias = +0.20V

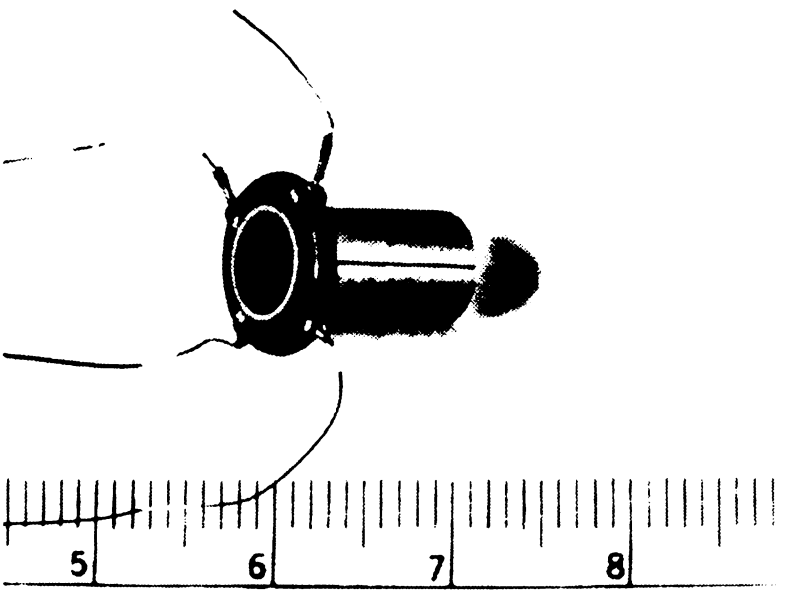

Figure 2.7 Piezoceramic tube with O-ring attachment. The scale is in centimeters.

wrapped around a Viton O-ring[14]. To make electrical contact, the insulation on the wire on the inside of the O-ring is sanded off with a fine file. The O-ring size is chosen to be a snug fit on the piezo tube so that all four leads make good contact to their quadrants. It is important to use a Viton O-ring; the more readily available Buna-N O-rings have a leakage resistance of about 1MΩ which shorts the high-voltage quadrants.

Figure 2.8 is a diagram of the plate/piezo tube/tip structure. A fine steel spring inside the piezo holds the entire assembly together, yet does not degrade the performance of the microscope[15]. The aluminum flange on the top of the tube touches the inside electrode of the tube and provides electrical contact to ground. The tunneling tip is held in a 3mm long SS syringe tube (O.D.=32mil, I.D.=20mil) inserted through a phenolic disc on the bottom of the piezo tube. The tip is slightly bent before inserting into the tube to prevent slipping.

In earlier versions of our STM, we attempted to hold the plate/piezo/tip structure together with cyanoacrylac glue ("Superglue") which is very convenient because it is strong and completely reversible (acetone dissolves the glue in minutes). Although the behavior of this glue is excellent at room temperature, it cracked during thermal cycling between room temperature and 77K. There are glues, such as "Stycast"[16], which survive thermal cycling, but these are so difficult to dissolve that they are essentially permanent.

In most experiments, our tunneling tip is a 10 mil Pt-Rh wire[17] which is cut, by hand, at a 45^{o} angle, with a clean pair of scissors. We find that this simple procedure yields atomic resolution on graphite almost every time. We also tested a 10 mil Nb wire as a tunneling tip with a view toward future experiments with superconducting tips. Cutting the Nb wire with scissors failed to produce a sharp tip and good images. Instead, we produced sharp Nb tips by first scribing a shallow indentation around the wire with a razor and then pulling the wire apart so that it breaks at the indentation and forms a sharp

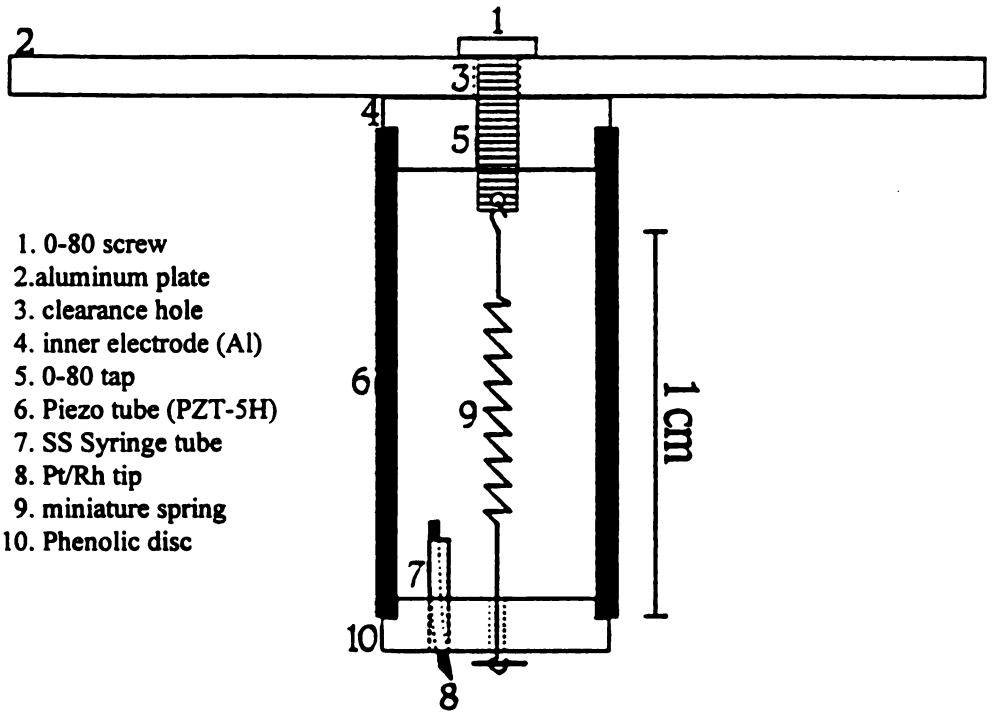

Figure 2.8 Plate/Piezo tube/tip structure

tip at the pulled cross-sectional surface. This pulled Nb tip performs reliably, producing good images at room temperature. Figure2.9 shows Scanning Electron Microscope (SEM) pictures of cut Pt-Rh tip and pulled Nb tip. An atomic resolution image of gold was obtained once at room temperature with the Nb tip in constant height mode. (see Figure 2.10) In this figure, the average distance between neighboring atoms is 2.95 Å which agrees well with the known value, 2.88Å.

As seen in Figure 2.1, the STM is attached to the end of a cryogenic stick with 4 wooden posts. The stick itself is a phenolic tube[18]. These fibrous materials help dissipate mechanical vibrations traveling down the stick. Electrical leads to the STM are miniature 50Ω coax cables[19]. The tunneling current lead is particularly susceptible to noise from triboelectric currents due to mechanical movement[3]. To prevent such movement, this lead is threaded through a tight-fitting stainless steel syringe tube which is clamped at several points along the inside of the phenolic tube.

2.4 OPERATION

With commercial electronics and software[20], our STM performs very reliably, routinely giving atomic resolution on graphite and showing terraces and monatomic steps on gold. (see Figure 2.6 and 2.7). The lowest mechanical resonance of the STM is 2.8 kHz, due to vibration of the sample stage. Figure 2.11 is the power spectrum of the tunneling current showing the STM resonating at that frequency. With no special temperature control precautions, the thermal drift at room temperature is typically 1Å/sec after a 10 minute settling period. At 77K or lower, the thermal drift is very small, less than 5Å/hour.

For cryogenic operation the STM is lowered down the throat of a Helium storage

(a)

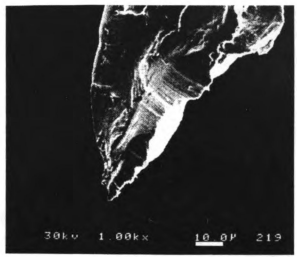

(b)

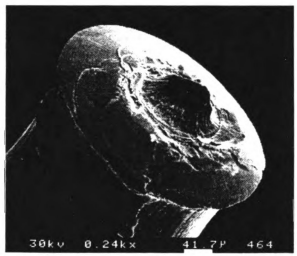

Figure 2.9 SEM pictures of STM tips. (a) cut Pt-Rh tip. (b) pulled Nb tip.

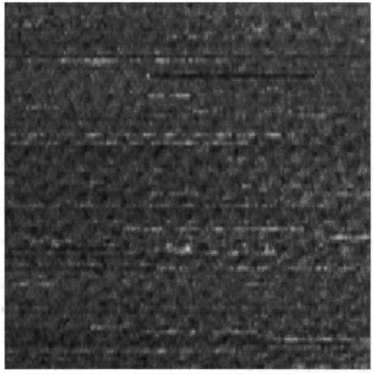

Figure 2.10 67Åx67Å scan of (111) gold with a pulled Nb tip at room temperature in constant height mode. Sample bias = +68mV.

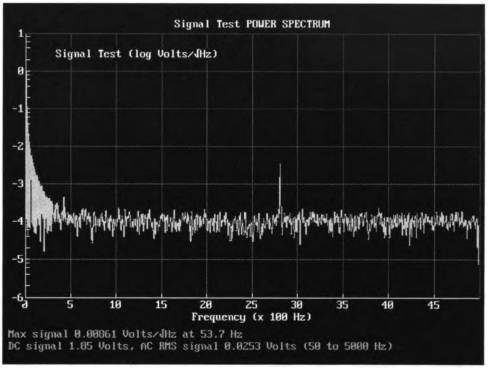

Figure 2.11 The power spectrum of the tunneling current showing the STM resonating at 2.8 kHz.

dewar[21]. The STM, which is enclosed in a grounded steel can with small ventilation holes, is operated in the vapor just above the bath. We find very poor operation in the liquid, presumably because of vibration due to bubbling.

For vibration isolation, we suspend the entire dewar by large rubber bands from a steel frame. Our experience is that noise due to building vibrations is relatively easy to eliminate. A more difficult problem, in a non-vacuum system such as ours, is vibration due to acoustical noise (from fan motors, etc.)

The quality of images taken at low temperatures depends critically on the cleanliness of the sample surface. Layered materials, such as graphite, do not acquire surface contaminants and can be imaged well at any temperature. However, metal surfaces such as Au, Ni, Pb, Ag, etc. acquire one or more monolayers of hydrocarbon contamination after several minutes of exposure to air. This hydrocarbon layer does not seem to degrade STM images taken at room temperature. However, we find that when an air-contaminated sample is cooled to below about 240K, the STM images become extremely noisy, apparently because the hydrocarbon layer freezes and produces an icy coating which disrupts tunneling. To produce good images of metals at low temperatures, we find it necessary to take freshly evaporated samples directly from the vacuum evaporation chamber to the low-temperature STM as quickly as possible, with no more than 5 minutes of exposure to air. Schemes to circumvent this problem will be discussed later in chapter 8 in detail.

In summary, we have described the design and operation of a simple STM which functions reliably from room temperature to 4K. The STM is assembled without glues and solders and can be quickly and easily disassembled for repair or modification.

REFERENCES FOR CHAPTER 2

1 A.P. Fein, J.R. Kirtley, and R.M. Feenstra, Rev. Sci. Instrum. **58**, 1806 (1987).

2 H.G. LeDuc, W.J. Kaiser, and J.A. Stein, Appl. Phys. Lett **50** (26), 1921 (1987); W.J. Kaiser and R.C. Jaklevic, Surface Sci., **55** (1987).

3 J.W. Lyding, S. Skala, J.S. Jubacek, R. Brockenbrough, and G. Gammie, Rev. Sci. Instrum. **59**, 1897 (1988).

4 M.D. Kirk, T.R. Albrecht, and C.F. Quate, Rev. Sci. Instrum. **59**, 833 (1988).

5 The resonance frequency of a plate supported underneath along two edges is proportional to $(E/\rho)^{1/2}$, where E is the Young's modulus and ρ is the density of the plate. The value, E/ρ of aluminum is about 4 times as great as that of a steel.

6 Burleigh Instruments, Inc., Burleigh Park, Fishers, NY 14453, (716) 924-9355.

7 Super-Invar is a 65% Fe/ 35% Ni alloy with a room temperature coefficient of thermal expansion of less than 1×10^{-6} K^{-1}; it is like Invar, but with a more precisely controlled Fe/Ni ratio, designed to give a smaller thermal coefficient. In this ferromagnetic material, at room temperature, the positive coefficient of thermal expansion is nearly canceled by a negative magneto-constrictive coefficient. The total linear contraction between 300K and 4K is 5×10^{-4}, about 1/6 that of stainless steel. See "Physics Vade Mecum", H.L.Anderson, ed., American Institute of Physics, New York, p.131.

8 Burleigh sells Super-Invar in 3/4" thick plate and in solid rod of various diameters.

9 Almac Plastic Inc., 47-42 37th Street Long Island City, NY 11101

10 Fine bolts and nuts are available from J.I.Morris Co., Southbridge, Massachusetts 01550

11 Extremely small steel springs are available from Lee Spring Co., 1462 62 St. Brooklyn, NY 11219.

12 PZT-5H piezo tube from Staveley/E.B.L. Div. Crystal Products, 91 Prestige Park Cir., East Hartford, CN 06108, (302) 289-5428.

13 We have found that the piezo response drops by nearly a factor of 10 between

room temperature and helium temperatures, in contrast to other workers who reports a factor of 5. See ref. 1.

[14] A 1/4" ID - 3/8" OD Viton O-ring provides a snug fit around a 1/4" diameter piezo tube.

[15] The mass of our 1/4" long spring is 0.019 gm, small compared to the 0.912 gm mass of the piezo tube.

[16] Emerson & Cuming, Inc., Woburn, MA 0188, (617) 938-8630.

[17] Thermocouple wire from Omega Engineering Inc., P.O.Box 4047, Stamford, CT 06907, (800)-TC-OMEGA.

[18] Grade L phenolic tubes from Almac Plastics Inc., 26400 Growsbeck Highway, Warren, MI 48090, (313) 773-9050.

[19] S-1 miniature stainless steel coaxial cable from LakeShore Cryotronics, Inc., 64 E. Walnut St., Westerville, OH 43081, (614) 891-2243.

[20] RHK Technology Inc., 1750 W. Hamlin Rd., Rochester Hills, MI 48309, (313) 656-3116.

[21] Cryofab, Inc, 540 North Michigan Ave., P.O.Box 485, Kenilworth, NJ, 07033 (210) 686-3636. This company makes storage dewars with special wide necks. Our 60 liter dewar has a 2" neck and a boil-off rate of 1.5 liters liquid helium per day.

Chapter 3

SAMPLE PREPARATION

Atomically Flat Gold Films Grown on Hot Glass

3.1 ABSTRACT

In this chapter, the results of a scanning tunneling microscope (STM) study of the morphology of Au films thermally evaporated onto heated glass substrates are discussed. Au films of thickness 20nm-80nm were evaporated onto Corning glass cover slips at temperatures of 20C-465C. Before the evaporation, the glass substrates were pre-baked at 300C-400C for 12 hours to remove surface contamination. We have measured grain size and surface roughness of the films, and our best results were obtained with Au films 80nm thick evaporated onto 300C substrates. These films have 250nm diameter grains with large, atomically flat tops exhibiting step-free terraces as large as 200nm x 200nm. These results are comparable to the best reported results for Au grown on heated mica and show that epitaxial growth is not required for the production of films with large atomically flat regions. This study of Au on glass was motivated by our failure to produce flat films of gold on mica using recipes in the literature. Possible reasons for our poor results with mica are discussed.

3.2 INTRODUCTION

In this chapter, the results of a scanning tunneling microscope (STM) study of gold films thermally evaporated onto heated glass substrates are reported. We find that gold films grown on glass cover slips held at 300C exhibit large, faceted grains with atomically flat tops as large as 200nm x 200nm. The production of such large, atomically flat regions is comparable to the best results obtained for Au on heated mica[1,2,3,4] and for faceted Au balls made by melting Au wire[5].

We have also made several attempts to grow flat Au films on heated mica substrates using the recipes reported in the literature, but the resulting films are of very poor quality. We will argue that our poor results are due to the decomposition of the mica during the deposition.

Since the growth of Au on mica is epitaxial[6], one might be tempted to assume that epitaxial growth is a requirement for the making of atomically flat films. Our results for Au on amorphous glass show that epitaxy is definitely not necessary for the production of large, atomically flat regions.

There have been previous STM studies[3,7,8] of Au evaporated onto glass, but for the most part, these have dealt with Au films evaporated onto room temperature substrates. However, Putnam et. al.[3] report that a 100nm Au film evaporated onto a glass slide at 430C showed no atomically flat regions. This result is consistent with our finding that the optimum temperature for the production of large facets is about 300C; we find that higher substrate temperatures result in rough films.

3.3 PROBLEMS WITH MICA SUBSTRATES

Our study of gold on glass was motivated by our failure to reliably produce good films of Au grown on heated mica. Although other groups[1,2,3,4] have reported the production of atomically flat Au films grown by thermal evaporation on heated mica substrates, our attempts to reproduce these results produced films that are extremely rough and have a milky appearance. Figure 3.1 is an SEM photograph of one of our rough Au films. This film, grown by evaporation on cleaved mica[9] held at 350C, is 200nm thick and has an rms surface roughness of about 100nm. Before evaporation the mica was baked in vacuum for 23 hours at 370C. We find that rough films result when the temperature of the pre-bake and deposition is in the range 320C-500C. Films of moderate quality result when the temperature of the pre-bake and deposition is less than 280C. Our results are in marked contrast to the results of others[4] who report excellent films when the temperature of the pre-bake and deposition is about 500C.

We believe that the discrepancy between our results and those of other groups is due to the variable quality of commercially available mica. Mica is a naturally occurring silicate mineral with a complex layered structure[10]. This silicate undergoes dehydroxylation at elevated temperatures, losing internal OH groups and giving off water. The dehydroxylation process in muscovite mica occurs very gradually over an extremely broad temperature range extending from roughly 100C to 900C[11,12,13]. Typically, mica samples show a weight loss that is linear with temperature in the range 100-500C and amounts to 1 - 3% at 500C. In the temperature range 500-900C, the weight loss is somewhat more rapid, with samples losing 3 - 5% of their weight over this range. The exact weight loss depends on the rate of the temperature increase and on the sample. It is quite difficult to completely dehydroxylate mica unless the temperature is raised above 1000C or the sample is baked for many hundreds of hours at lower

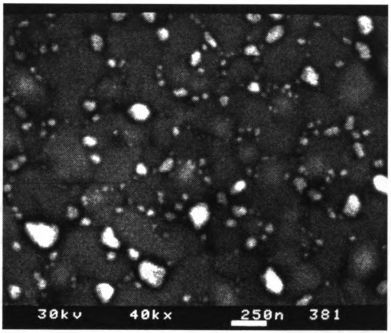

Figure 3.1 SEM photograph of a 200nm-thick gold film grown on mica at 350C.

temperatures[11]. The poor quality of our Au films indicates that the dehydroxylation of the mica is proceeding during the evaporation and that the substrate is continuously producing water under the growing film. Given the wide range of dehydroxylation rates reported in the literature, we expect that the success of mica as a substrate for Au films will vary markedly depending on its exact impurity content, defect structure, etc.

3.4 SAMPLE PREPARATION

Our substrates are 0.15mm thick glass cover slips (Corning #0211 cover glass). According to the manufacturer, this glass has a softening point of 720C, and will undergo slow creep at temperatures as low as 508C[14]. The cover slips were cut into 10mmx10mm squares and cleaned by ultrasonic wash in acetone, methanol, and de-ionized water, followed by drying in a stream of dry nitrogen. Our evaporation chamber is diffusion-pumped with a LN_2 cold trap and a base pressure of 2×10^{-7} mbar. In the evaporator chamber, the substrates were held with stainless steel clips on a copper block which contains a resistive heater and a platinum resistance thermometer[15]. The setup for the sample heater block is shown in Figure 3.2. Before deposition, the sample block and glass substrates were pre-heated to 300-400C in vacuum for at least 12 hours, after which time the system attained its base pressure. The temperature of the sample block was then brought to the final substrate temperature of between 20C and 465C. After briefly outgassing the tungsten evaporator boat, a shutter was opened and gold was evaporated onto the heated glass substrate at 0.1nm/sec. During the evaporation the pressure remained below 2×10^{-6} mbar. The thicknesses of the films were measured with a quartz crystal thickness monitor which was calibrated against a surface profiler. After the evaporation, the samples were allowed to cool in vacuum to room temperature.

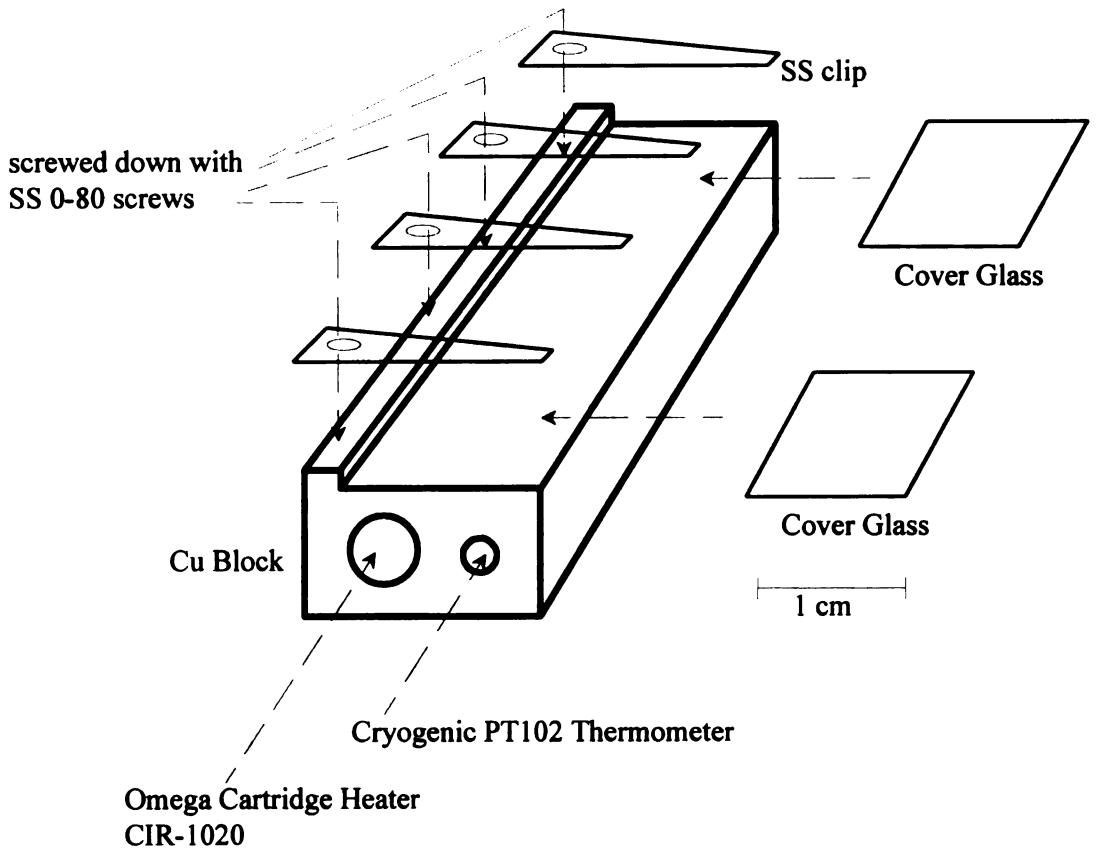

Figure 3.2 The sample heater block.

During the evaporation, the temperature of the growing film increases above that of the copper sample stage due to radiation from the evaporator boat. In our evaporator, the distance between the evaporator boat and the sample is 8.5 cm and 200 watts power is supplied to the boat during evaporation. We have measured the temperature rise of the surface of the sample by clipping a thin-film resistance thermometer[16] to a glass cover slip on the copper sample stage which is then exposed to a heated evaporator boat. Figure 3.3 is a plot of the temperature rise vs. exposure time in seconds. Two curves are shown, for starting temperatures of 26C and 201C. At higher starting temperatures, the sample radiates more efficiently and the temperature rise is less. Recall that the Au is evaporated at 0.1nm/sec, so the horizontal scale in Figure 3.3 can also be interpreted as thickness of the Au film in units of 0.1nm. From the curve, we see that in the worst case, that of an 80nm thick film with a starting temperature of 20C, the temperature rise is 13C. An 80nm thick film at a starting temperature of 400C has a temperature rise of less than 8C.

After evaporation the samples were stored in a nitrogen-filled desiccator. Samples were transferred to an air STM[17], and all imaging data were collected within 3 hours of exposure to air. The tunneling tip is a 10 mil Pt-Rh wire cut with clean scissors. Such tips routinely produce atomic resolution on graphite. All images in this work were taken in topographic mode, with a tunneling current of 1.0nA and a bias voltage in the range 100 - 300mV (sample positive). The STM images shown in this chapter all have 256 scan lines and are displayed as if illuminated by a distant point source. Occasionally, the STM images showed tip artifacts, recognized as regularly repeated features in the image as seen in Figure 3.4. In these cases, the tip was re-cut until the artifacts disappeared.

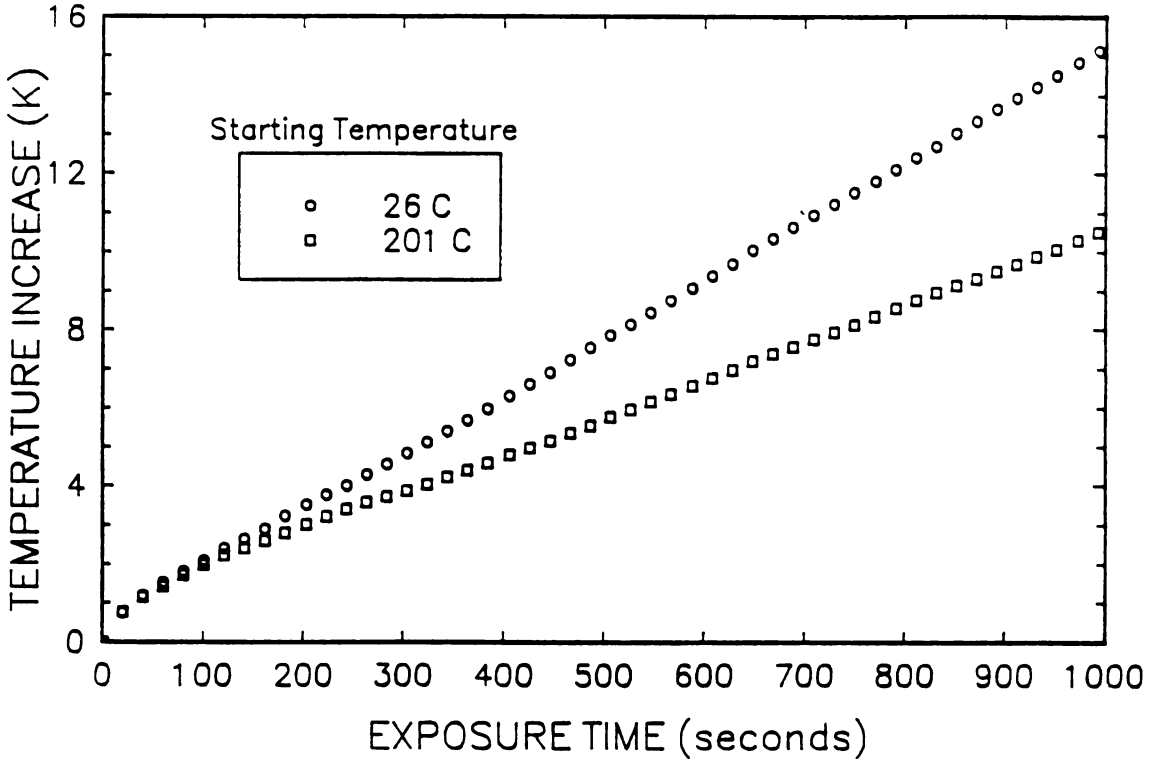

Figure 3.3 Increase in temperature of the sample surface vs. time of exposure to the hot tungsten evaporator boat.

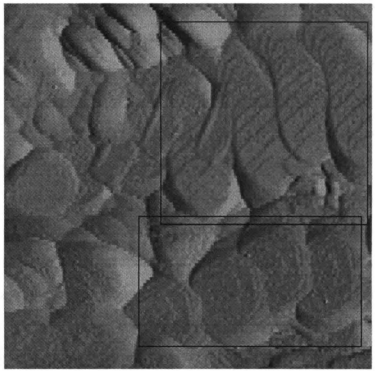

Figure 3.4 STM image showing multiple-tip artifacts (inside the boxes). T=300C, 80nm sample. Scan area = 0.5μm x 0.5μm.

3.5 RESULTS

Figure 3.5 is a plot of average grain size vs. substrate temperature for Au films of thicknesses 20, 40, 60, and 80nm. Because of the radiative heating discussed above, the temperature of the growing film increased above that of the sample stage by typically 5 to 10C during the evaporation (in the worst case the increase is 13C). The 20nm thick samples grown at temperatures above 150C were not electrically continuous and so could not be imaged with an STM. For these samples, the grain size was determined from SEM photographs.

To measure the average grain size from the STM images, we computed the angle-averaged height-height autocorrelation function[18]. The distance between the first two bumps in the autocorrelation function is a good measure of the grain diameter (see Figure 3.6). For some of the films the autocorrelation function did not show clearly defined bumps. In these cases, we determined the average grain diameter from the average grain area, which we obtained by dividing the scan area by the number of grains counted by eye.

STM or SEM (for electrically discontinuous films) images of the 20, 40, 60, and 80nm thick films grown at the substrate temperatures of 20C, 105C, 185C, 300C, 400C, and 465C for each thickness are shown in Figure 3.7, 3.8, 3.9 and 3.10 respectively. The figures show the evolution of the grain morphology as substrate temperature is increased.

Figure 3.11 displays typical scan profiles for the 80nm thick samples, and Figure 3.12 is plot of the measured rms surface roughness as a function of substrate temperature for samples of average thicknesses 40nm, 60nm, and 80nm. The rms surface roughness is 1 standard deviation of the pixel height histogram (taken over $0.25 \times 0.25 \mu m^2$ for the 20C sample and over $1.0 \times 1.0 \mu m^2$ for all other samples.) With the exception of the 60nm sample grown at 180C, which displays an anomalously large roughness, the overall trend

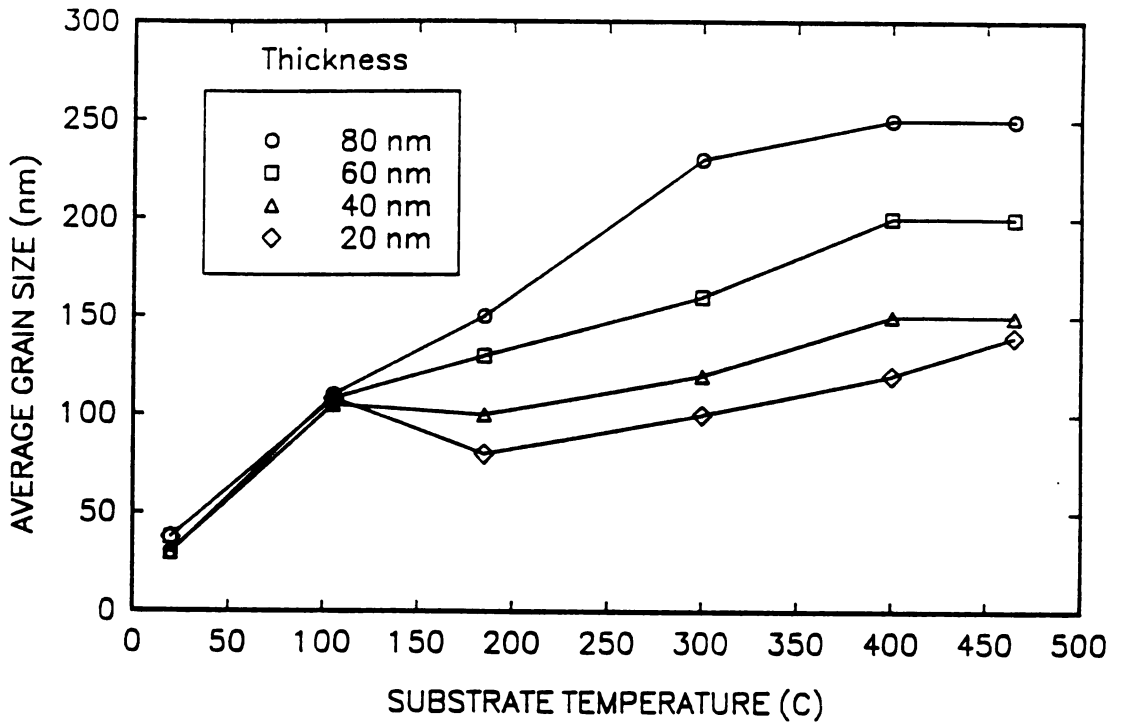

Figure 3.5 Average grain size in gold films evaporated onto glass as a function of substrate temperature during growth.

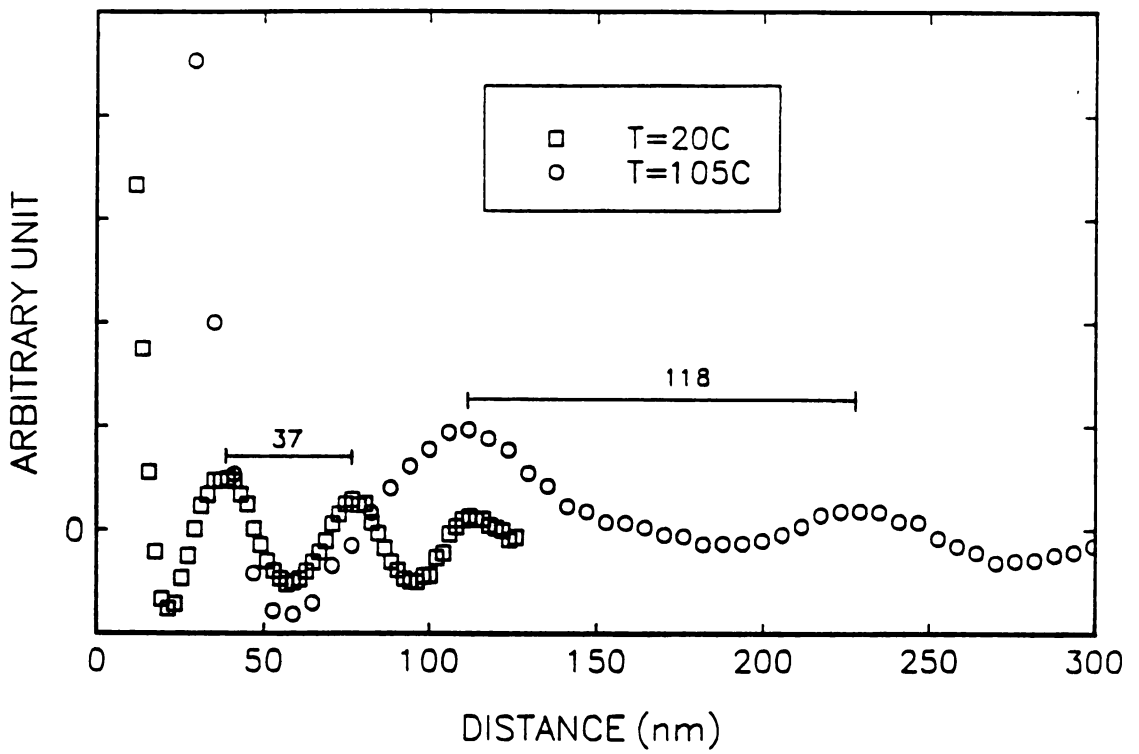

Figure 3.6 Height-height autocorrelation functions for 80nm thick gold films grown at 20C and 105C.

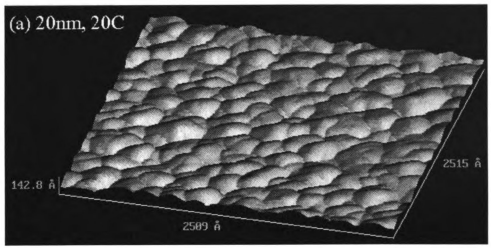

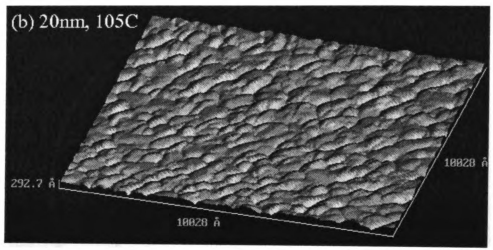

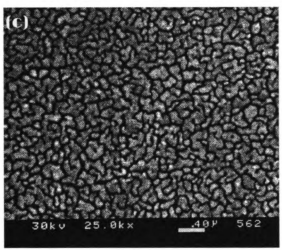

(c) 20nm, 185C

Figure 3.7 (a-b) STM images of 20nm thick gold films grown on glass substrates of (a) 20C, (b) 105C. (c) A SEM image of a 20nm thick gold film grown on a glass substrate of 185C.

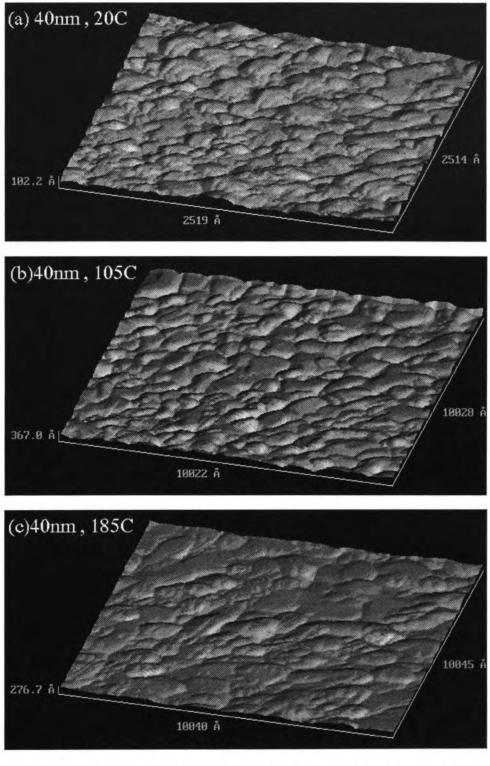

Figure 3.8 STM images of 40nm thick gold films grown on glass substrates of (a) 20C, (b) 105C, (c) 185C, (d) 300C, (e) 400C, and (f) 465C.

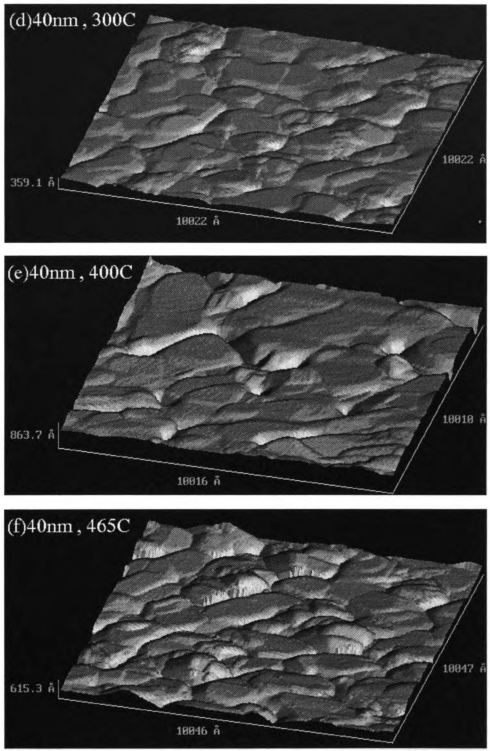

Figure 3.8 (cont'd).

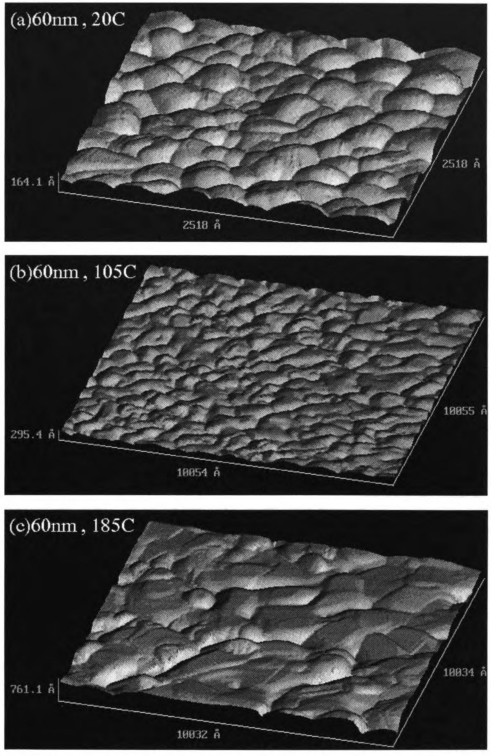

Figure 3.9 STM images of 60nm thick gold films grown on glass substrates of (a) 20C, (b) 105C, (c) 185C, (d) 300C, (e) 400C, and (f) 465C.

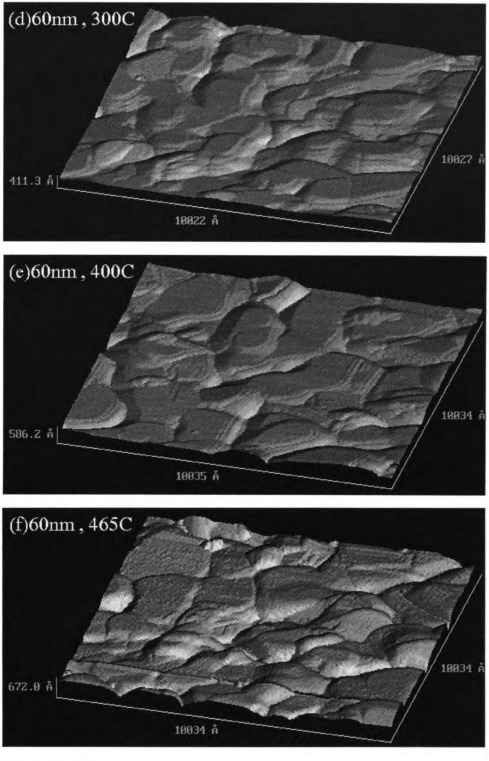

Figure 3.9 (cont'd).

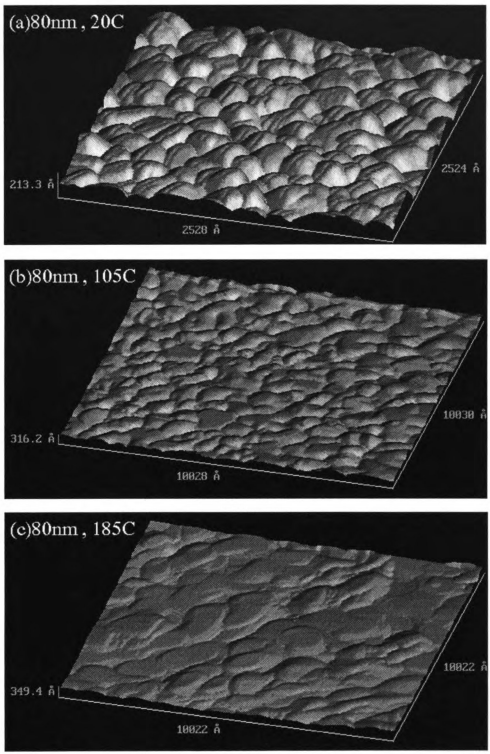

Figure 3.10 STM images of 80nm thick gold films grown on glass substrates of (a) 20C, (b) 105C, (c) 185C, (d) 300C, (e) 400C, and (f) 465C.

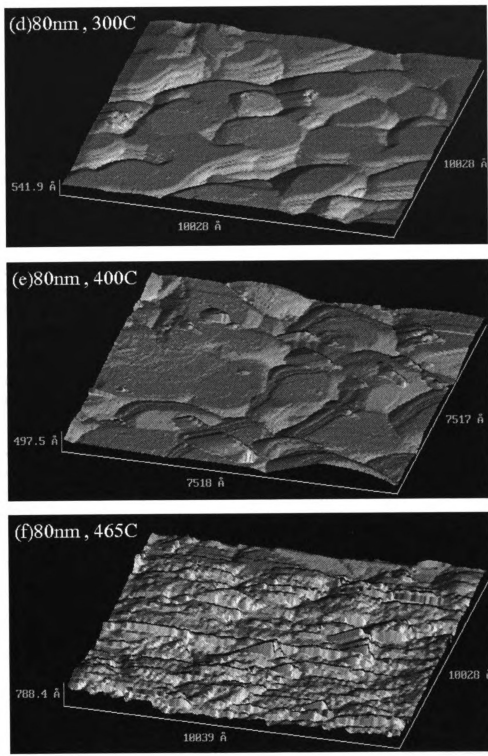

Figure 3.10 (cont'd).

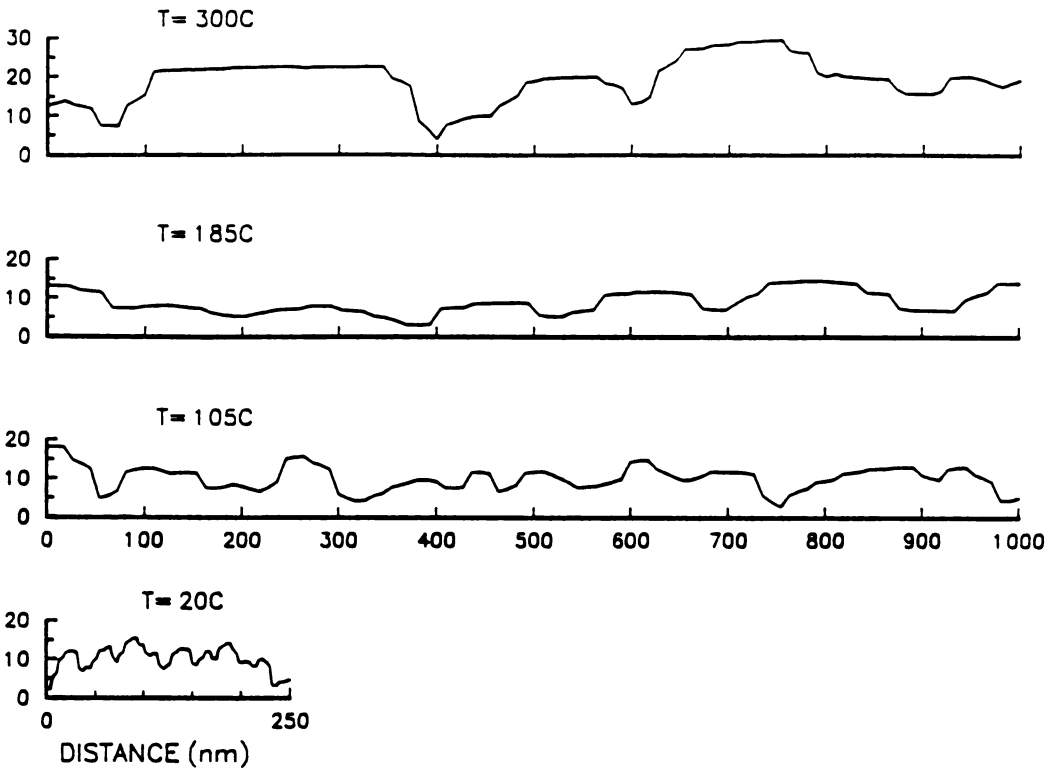

Figure 3.11 Typical scan profiles for 80nm thick films. (The vertical scale is expanded.)

in Figure 3.12 is a gradual increase in roughness with increasing substrate temperature. The unusually rough 60nm sample is shown in Figure 3.9 (c) and appears to have no other unusual features. We suspect that its measured roughness was large because it was scanned with an unusually sharp tip and that the other samples show smoother surfaces because they were scanned by more blunt tips. A blunt tip cannot reach into the depths of the trenches between grains and will produce an erroneously smooth profile. Clearly, the roughnesses displayed in Figure 3.12 are lower limits.

The samples grown at room temperature all show an average grain size of about 30nm, independent of film thickness. As seen in Figure 3.7 (a), 3.8 (a), 3.9 (a) and 3.10 (a), the grains are all of about the same size and have smoothly rounded surfaces with no evidence of faceting. The surface roughness of these T=20C films increased slightly with sample thickness from 2.0nm for the 20nm film to 3.0nm for the 80nm film. We also grew a set of films at room temperature with no substrate pre-bake. Compared to the films with the substrate pre-bake, the no-prebake films exhibited a larger spread in grain sizes, a slightly larger average grain size, and rougher surfaces with roughness varying from 2.6 to 4.0nm. Evidently, pre-baking removes light molecular-weight contamination from the glass substrates and results in smoother films.

The films grown with a substrate temperature of 105C all have an average grain size of about 100nm, independent of film thickness, and all have a surface roughness of about 3.9nm. Some of the grains show flat tops with terraces 10 or 20nm wide separated by multi-atomic steps. (See Figure 3.13.)

Samples grown at temperatures at or above 185C all show a grain size that increases with both the sample thickness and the substrate temperature. At these elevated temperatures, films of 20nm thickness are discontinuous and break up into isolated islands. SEM examination shows that each island contains only a few grains and that the island size is comparable to the grain size. The break-up of the film into isolated islands

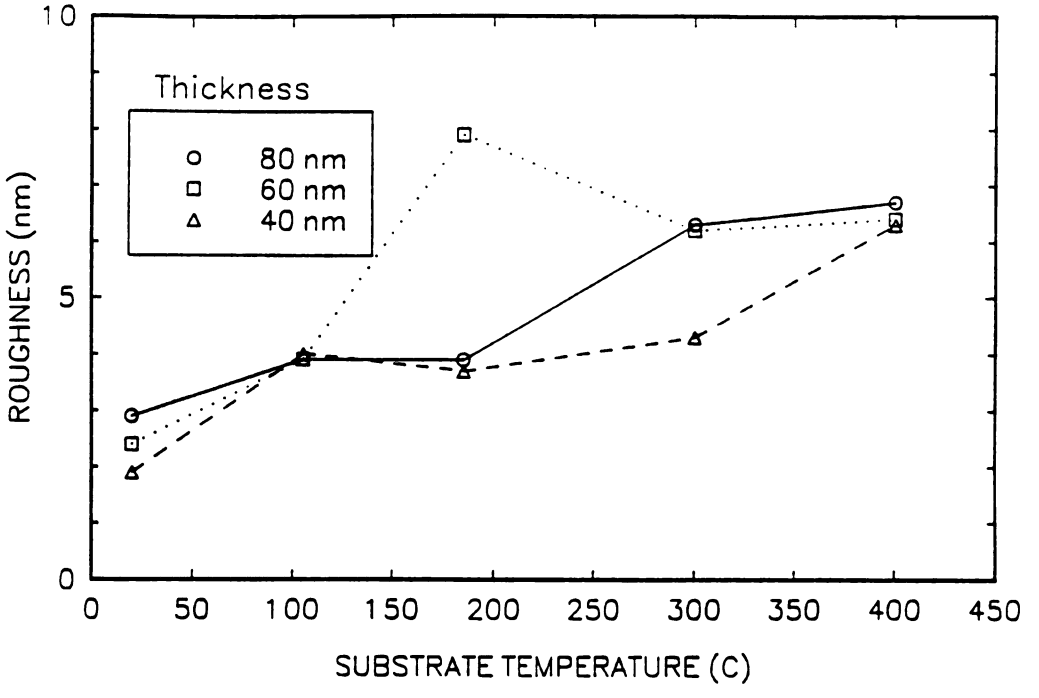

Figure 3.12 Measured rms surface roughness vs. substrate temperature for 40nm, 60nm, and 80nm thick films.

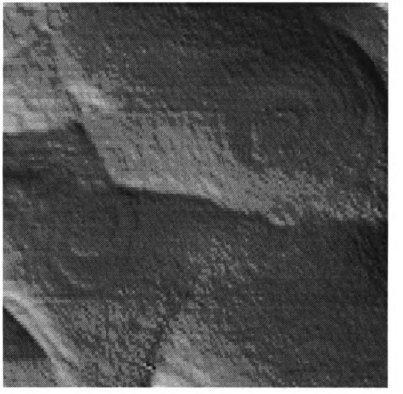

Figure 3.13 Grains showing flat tops with terraces separated by multi-atomic steps. Scan size = 1016Å x 1014Å. A 60nm-thick gold film on a 105C glass substrate.

is the reason for the decrease in average grain size seen in the 20nm thick film in going from 105C to 185C.

Films grown at 185C show grains with clearly developed top facets, which we believe to be the (111) face. We occasionally observe the hexagonal faceting characteristic of the (111) face.[3,4] (See Figure 3.14) Terraces 10-100nm wide, separated by monatomic steps, are seen. (See Figure 3.15)

Films grown at 300C exhibit the largest step-free terraces. 80nm thick films grown at this temperature have an average grain size of 250nm. As seen in Figure 3.16, the tops of the grains typically show a few terraces 20-40nm wide and 100-200nm in length, separated by monatomic steps. About 1 out of 20 grains has a step-free terrace of area 100nm x 100nm or larger, and occasionally a large grain is seen with a 200nm x 200nm atomically flat region. Figure 3.17 shows such a large region bounded by a 60^{o} hexagonal facet. The rms roughness of step-free regions seen in Figs. 3.16 and 3.17 is less than 0.03nm. The STM images show the trenches between grains to be 10 - 20nm deep and 50 - 100nm wide. (Again, we cannot rule out the possibility that the trenches are actually deeper and are not accurately profiled by a blunt tunneling tip.) The measured overall roughness of these 80nm films grown at 300C is 6 - 7nm. We expect that even larger grains and larger terraces will appear in films with thickness greater than 80nm.

Films grown at 400C are similar to the 300C films but the tops of the grains are frequently marred by small, round bumps, about 6nm in diameter and 1nm high, rising above the otherwise atomically flat terraces. In films grown at 465C, these protrusions are larger (10nm high and 30nm in diameter) and densely cover the tops of the grains, destroying the terraces. We speculate that, at these elevated temperatures, the glass has begun to creep, causing strains to build in the growing films and ruining the development of facets.

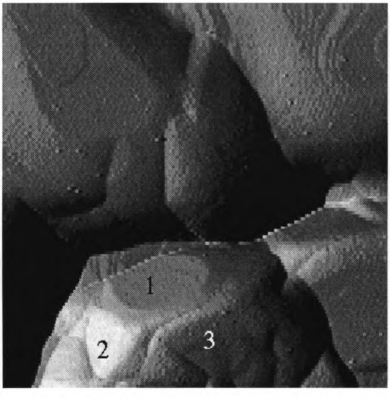

Figure 3.14 The hexagonal faceting of gold crystal. The angle between any two of the three faces 1, 2, and 3 are 120°. A 60nm-thick gold film on a 185C glass substrate.

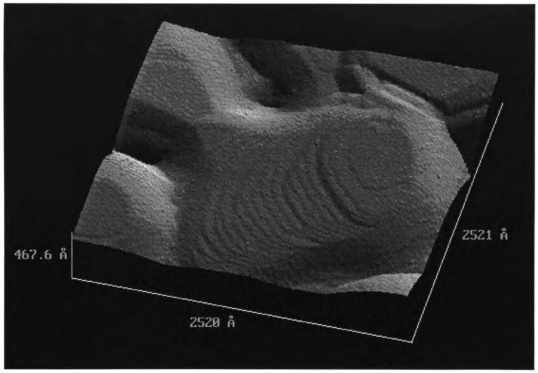

Figure 3.15 Terraces separated by monatomic steps on clearly developed top facet. Scan size = 2521Å x 2520Å. A 60nm-thick gold film on a 185C glass substrate.

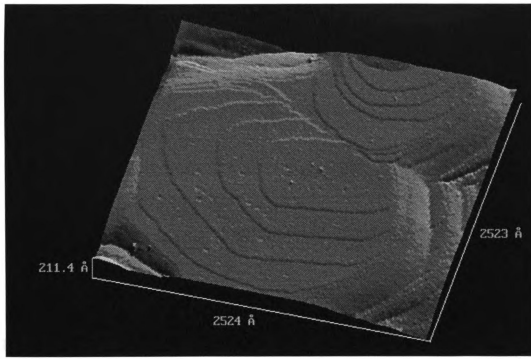

Figure 3.16 STM image of an 80nm-thick film grown at 300C showing a large grain with terraces separated by monatomic steps.

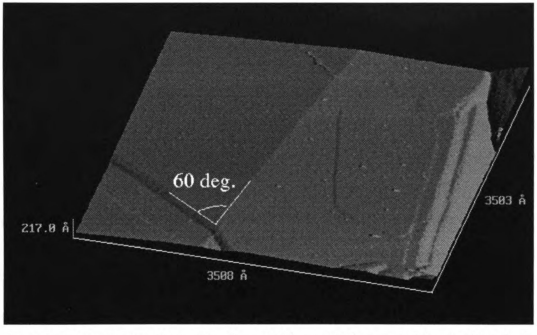

Figure 3.17 Large step-free region bounded by a 60^{o} hexagonal facet which is the characteristic of Au(111) face. The substrate temperature during growth was 300C.

We also studied Au films grown at room temperature and then annealed at high temperature. Films grown at 26C were heated to 485C in vacuum for 3 hours. The annealed samples have properties similar to those of films grown at high temperatures. Figure 3.18 is an image of an annealed 60nm thick sample showing atomically flat grains of 250nm size with some monatomic steps. Again, surface was marred by small, round bumps. Occasionally, we observe monolayer or bilayer wormy channels with the width of 20-50Å on flat top of the grains. (See Figure 3.19)

We made one attempt to grow Au films on quartz substrates at 500C. Clear fused quartz has a softening point of 1665C and a strain point of 1070C and so it may be expected to provide a stable substrate at high temperatures. The quartz substrates[19] were pre-baked at 500C for 6 hours and then Au films of thickness 45nm and 80nm were deposited at 0.1nm/sec. The resulting films were extremely poor; they had a milky appearance very similar to the failed Au-on-mica films. The average grain size was about 100nm and the surface roughness was comparable to the sample thickness. We do not understand these poor results, but we speculate that differential thermal contraction during sample cool-down may damage the film.

3.6 SUMMARY

Thermal evaporation of Au onto heated glass substrates is an extremely reliable technique for the production of films with large, atomically flat regions. We find that 80nm thick Au films evaporated onto glass substrates held at temperatures of 300C exhibit large faceted grains of about 250nm diameter. The tops of the grains are atomically flat with step-free terraces as large as 200nm x 200nm. The grains are separated by trenches 10-20nm deep and 50-100nm wide, leading to an overall rms

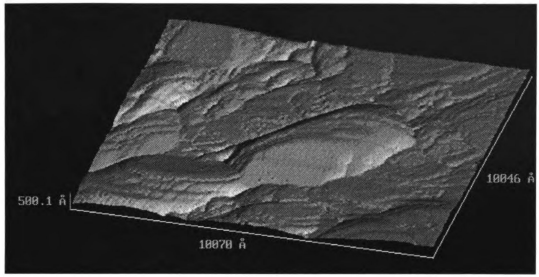

Figure 3.18 STM image of a 60nm-thick gold film annealed at 485C for 3 hours. The film was evaporated at 26C before annealing.

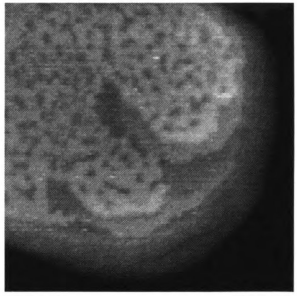

Figure 3.19 A monolayered wormy structure on flat top of the grain in the annealed gold film. Scan area = 1003Å x 1004Å.

surface roughness of 6nm or greater. In comparing our films with the best reported results for gold films grown on mica[4], our films exhibit larger step-free, atomically flat regions, but have an average roughness that is greater than the Au-on-mica films. We find that mica is unreliable as a substrate, apparently because of the variable quality of commercial supplies.

REFERENCES FOR CHAPTER 3

1 C.E.D. Chidsey, D.N. Loiacono, T. Sleator and S. Nakahara, Surface Sci. **200**, 45 (1988).

2 R. Emch, J. Nogami, M.M. Dovek, C.A. Lang, and C.F. Quate, J. Appl. Phys. **65**, 79 (1989).

3 Albert Putnam, B.L. Blackford, M.H. Jericho, and M.O. Watanabe, Surface Sci. **217**, 276 (1989).

4 J.A. DeRose, T. Thundat, L.A. Nagahara, and S.M. Lindsay, Surface Sci. **256**, 102 (1991).

5 J. Schneir, R. Sonnenfeld, O. Marti, P.K. Hansma, J.E. Demuth, and R.J. Hamers, J. Appl. Phys. **63**, 1 (1988).

6 K. Reichelt and H.O. Lutz, J. Crystal Growth **10**, 103 (1971).

7 J. Vancea, G. Reiss, F. Schneider, K. Bauer, and H. Hoffmann, Surface Sci. **218**, 108 (1989).

8 Tzer-Shen Lin and Yip-Wah Chung, Surface Sci. **207**, 539 (1989).

9 Green muscovite mica supplied by Asheville-Schoonmaker Mica Co., 900 Jefferson Ave., P.O.Box 318, Newport News, VA 23607.

10 Thomas J. Pinnavaia, Science **220**, 365 (1983).

11 Ralph E. Grimm, **Clay Mineralogy**, McGraw-Hill Book Co. (1953), pp.233-238.

12 Stephen Guggenheim, Yu-Hwa Chang, A.F. Koster Van Groos, American Mineralogist **72**, 537 (1987).

13 The Spruce Pine Mica Company, a major supplier of mica, specifies 400-500C as the "Maximum temperature with no decomposition."

14 The glass has a softening point of 720C, an annealing point of 550C and a strain point of 508C. The softening point is the temperature at which the glass deforms under its own weight; the annealing point is the temperature at which internal stresses relax within 15 minutes; the strain point is the temperature at which internal stresses relax within 4 hours.

15 Lake Shore PT-102 platinum resistance thermometer

16 Omega model TFD thin film platinum resistance thermometer.

17 The electronics and software are made by RHK Technology, 1750 West Hamlin Rd, Rochester Hills, MI 48309. The scanning head is home-built and is described in M.A.Dubson and Jeeseong Hwang in Rev.Sci.Instrum. 63 (7), July 1992.

18 This function is defined as follows: if $z(\mathbf{r})$ is the height as a function of x-y position $\mathbf{r}$, the angle-averaged autocorrelation function is a function of scalar r and is $C(r) = \langle z(\mathbf{r}')\, z(\mathbf{r}'+\mathbf{r})\rangle_{\mathbf{r}',\theta}$, where $\langle\ldots\rangle_{\mathbf{r}',\theta}$ indicates an average over all vectors $\mathbf{r}'$ and an average over all angles θ of the position vector $\mathbf{r}$, keeping the length of $\mathbf{r}$ fixed.

19 Cut from quartz microscope slides made by Esco Products, 171 Oakridge Ave, Oakridge, NJ 07483.

Chapter 4

STM OBSERVATIONS OF SURFACE SELF DIFFUSION ON THE Au (111) PLANE

4.1 ABSTRACT

STM lithography, the technique to fabricate small structures with an STM tip on an atomically flat surface, is demonstrated. At room temperature in air, an STM study shows that the area of the monatomic gold island on (111) Au decays linearly in time. The surface diffusion constant is also measured from sequential STM images showing wandering monatomic steps or from the shape change of a gold mound. We find that the mass diffusion is faster in a heavily contaminated sample compared to a relatively clean sample.

4.2 INTRODUCTION

The problem of mass transport by surface self diffusion on metal surfaces was first considered by Volmer and Estermann, who observed the growth dynamics of a mercury crystal by the condensation process from its vapor state.[1] Since then, several methods to study the problem have been developed: a theoretical approach using surface potentials and adatom mobilities, and experimental approaches including semi-microscopic observations of mass transportation and direct observations of mobile surface atoms (molecules) on an atomic (molecular) scale. One of the accomplishments

of the theoretical approach is the introduction of the terrace-ledge-kink (TLK) model.[2] The details of this model will be discussed in chapter 5 along with the Monte Carlo simulation explaining our STM data.

Although several measuring techniques such as Auger Electron Spectroscopy (AES), Low Energy Electron Diffractometer (LEED), and workfunction measurement provide important information on surface structure, none of these gives direct real-space information on an atomic scale. The conventional method of directly observing surface morphology is to investigate the two dimensional projection of the 3-D configuration of a sample using a transmission electron microscope (TEM)[3]. Direct 3-D observations of diffusing atoms or molecules on metal surfaces has been accomplished using a Field Ion Microscope (FIM)[4,5,6], STM[7], and Atomic Force Microscope (AFM).

Atomic resolution observations of mass flow on a metal surface provide important clues about the microscopic mechanism of surface self diffusion. Peal and Cooper have reported[8] that, using an STM at room temperature in air, the area of single monolayer gold island decays linearly with time, i.e.

$$N(t) = N(t_0) - m(t-t_0) \tag{4.1}$$

where t_0 is the initial time, N(t) is the number of atoms in the island at time t, and m is the loss rate of atoms. In this chapter, time-sequential STM images are presented showing the same linear decay. The microscopic picture of this decay process will be discussed in detail in Chapter 5.

A direct measurement of the surface self diffusion coefficient can be made by observing the motion of an individual atom diffusing on an atomically flat surface. If the surface is ideal, i.e. without any local defects, the atomistic motion can be considered as

a 2-D random walk from one site to another site which are separated by a potential barrier. In this case we can define a diffusion coefficient[9] as

$$D = \frac{1}{4}\left(\frac{\bar{x}^2}{t}\right) \tag{4.2}$$

where $\bar{x}$, the mean square displacement of the adatom, and t, the duration of the observation, are measurable parameters. At room temperature, the adatom on a Au(111) surface diffuses ten's of nanometers in about 10^{-7} seconds so that the motion of the individual diffusing atom is too fast to observe with an STM since typical data acquisition time for one STM image is a few seconds at best. Lowering the ambient temperature can slow down the diffusive motion since the temperature dependence of the diffusion constant is expected to be

$$D_S = D_0 \exp(-E_b/kT) \tag{4.3}$$

where D_0 is a prefactor and E_b is the activation barrier for diffusion. Another technical difficulty is that it is very hard to obtain atomic resolution in air because one or more layers of water and hydrocarbon contamination build up on the metal surface after several minutes of exposure to air. This problem can be eliminated by operating the STM in Ultra High Vacuum (UHV).

In this experiment, the surface diffusion coefficient is measured either from the time-sequential STM images showing decaying monolayer islands or from the shape change of a gold mound which was lithographically fabricated by an STM.

4.3 EXPERIMENTAL TECHNIQUES

4.3.1 Sample Preparation

To observe the decay rate of a monolayer gold island, one needs a sample with large isolated grains with large facets showing atomically flat terraces separated by monatomic steps. As discussed in chapter 3, the evaporated gold films on hot glass satisfy these conditions. We also find that the <111> direction is perpendicular to the flat surface of the layers. Figure 4.1 is an x-ray 2θ scan[10] of the 80nm-thick, T=300C sample showing a strong {111} peak. The x-ray shows that the measured lattice constant between two {111} planes is 2.3509Å which is in accord with the monatomic step height of 2.36Å on gold {111}. All of the samples in this experiment are prepared by thermal evaporation of 60-80nm thick gold films on 300C glass substrates as described in chapter 3. Large-grained samples with large terraces and monatomic steps are produced almost every time with the recipe.

All the images in this experiment are obtained within a few days after the sample were made. We have not seen any surface diffusion in samples older than a month. We find that samples reach a static state after approximately one month. Figure 4.2 is a pair of STM images of a 6 month old sample showing no sign of activity even after 13 hours and 50 minutes. We reclean old samples by rinsing them in a flow of clean acetone and methanol followed by drying with clean N_2 gas. Even after the cleaning, sometimes tough greasy contamination on the old sample surface is identified from the streaky or fuzzy STM images. In that case we use the ultraviolet (UV) ozone cleaner to remove the tough organic contamination from the surface.

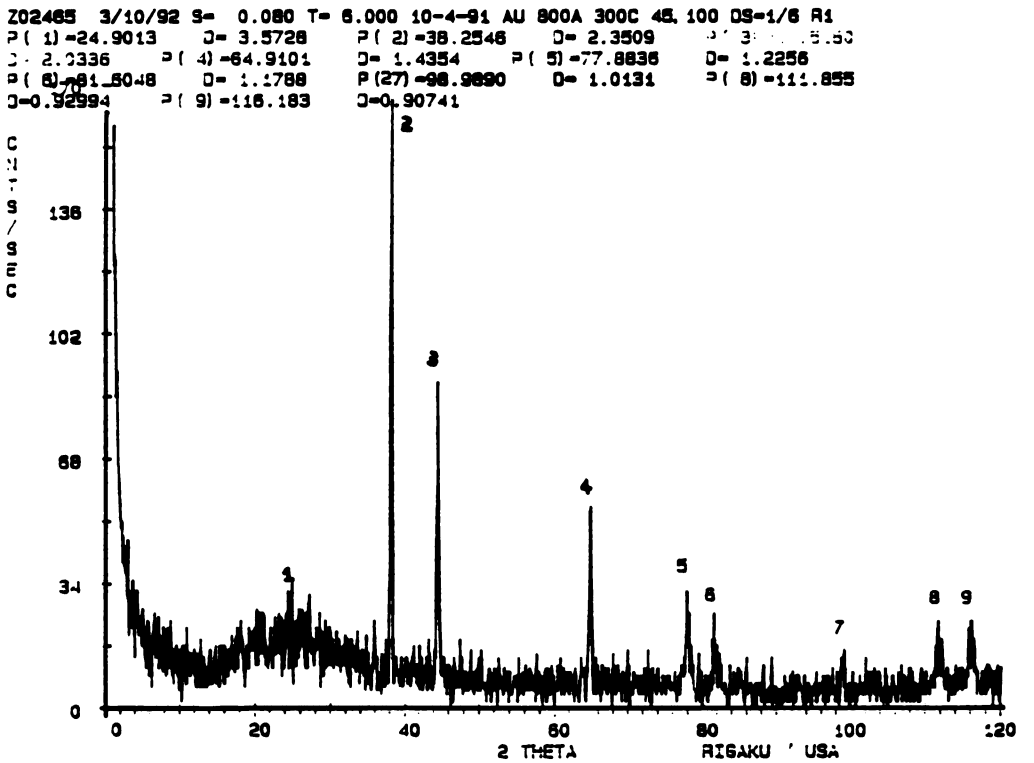

Figure 4.1 X-ray 2θ scan of the 80nm-thick gold film of 300C glass substrate. The peaks are identified as the orientations of a gold crystal: 2{111},3{200}, 4{220}, etc. The broad peak in position 1 is a contribution from an amorphous glass substrate.

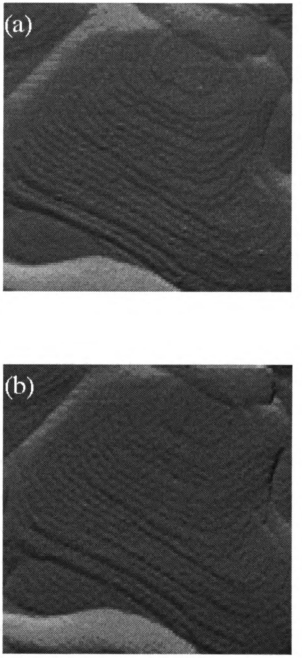

Figure 4.2 A pair of STM images of 6 month old sample showing no sign of activity. Scan area = $(250nm)^2$. (a) Image at time = 0. (b) Image after 13 hours and 50 minutes.

4.3.2 STM Lithography

All the images in this chapter are taken at room temperature in air in a constant current (topographic) mode using our home built STM described in chapter 2. Emch *et. al*[11] and Schneider *et al.*.[12] used an air STM to produce controlled features by applying voltage pulses to the tip. They also exhibited that at ambient temperature the written features disappeared on a time scale of hours. In our experiment, since not every layered structure created by evaporation undergoes surface diffusion, we lithographically fabricated small mounds or islands with an STM using the voltage pulse technique. There are several advantages to making small structures artificially. First, in most cases, we can expect the features to change because they are in a metastable state. Secondly, a small system is desirable so that we can collect enough data in a short period of time before the STM image degrades due to build-up of surface contamination. Thirdly, a system of appropriately small size can be modeled by the Monte Carlo simulation with the limitations in array size.

Now we describe our STM lithography procedure. The STM tip was scanned over the sample surface to find a grain with an atomically flat surface. The tip is then moved far away from the grain and crashed several times onto the gold surface so that the tip picks up gold atoms from the surface. Figure 4.3 demonstrates that the tip is not ruined even after several crashes or dragging it along the surface. The tip is sent over the atomically flat area again and a step pulse of +3-4V (sample at + voltage, tip at virtual ground) is applied to the sample for a period of 1-10msec to produce a pit or a mound. The feedback circuit maintains the constant tunneling current during the pulse. This procedure sometimes produces mounds, sometimes pits. As shown in Table 4.1, mounds tend to form with a preset tunneling current of below 1.05nA while pits tend to form above 1.05nA for a tunneling current. At high tunneling current (above 2.0 nA), the tip

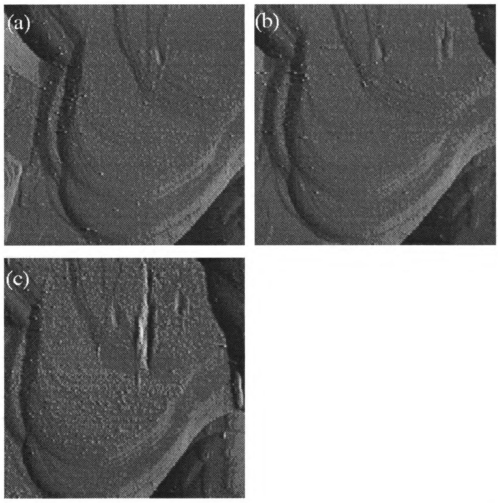

Figure 4.3 Images of tip-crashes. Scan area = $(30nm)^2$. (a) The first crash (b) The second crash. (c) The tip was being dragged between the two crash sites before imaging. Note that the monatomic gold steps are still visible even after the tip crashes several times.

Table 4.1 Features formed by voltage pulse under various conditions.

Preset Tunnel Current (nA)	Pulse height (V)	Pulse width (msec)	Feature
0.91	+3.0	5	mound
0.97	+3.0	20	mound
1.00	+3.0	10	mound
1.02	+3.0	5	mound
1.02	+3.0	5	mound
1.05	+3.0	10	mound
1.05	+3.5	10	pit
1.38	+4.0	5	pit
1.62	+3.0	20	pit
1.67	+3.0	20	pit

makes several pits and mounds on the surface. The pits and mounds fabricated by the voltage pulses are presented in Figure 4.4. Note the multiple-tip artifact in the images.

A reproducible way of controlling the size of fabricated features is not available at present. In most cases, a smooth, rounded gold grain with a size of a few nanometers in height and a few tens of nanometers in width is formed by the voltage pulse with a tunneling current below 1nA. In some cases, however, a layered structure of gold islands is produced. We believe that the features are made of gold atoms because the deposited island has a faceted crystalline shape and the height of the island equals the height of a monatomic terrace of Au{111} layer within the error bound.

Once interesting features such as mounds, well defined islands, and layered pits are found, the shape change is followed by imaging at regular intervals in time. For the measurement of number of atoms vs. time, the area of the island or pit is measured by counting the number of pixels inside the boundary of the feature then converting the image area to actual area. Finally, the number of atoms corresponding to an area is calculated simply by dividing the area by the unit area of the Au(111) plane. To define the boundary of a feature, we use the differential image which shows the curvature of the pixel intensity. Since the boundary also takes up a certain number of pixels in the image, the number of atoms corresponding to the pixels of the boundary is calculated. Half of this value is assigned as an upper bound of the error and half for the lower bound. To follow the shape change of a mound, the height and width are obtained from the surface profile.

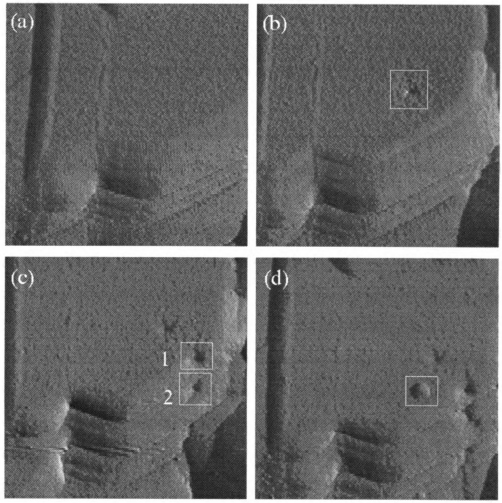

Figure 4.4 Pits and mound formed by voltage pulses. Scan area = $(120nm)^2$. (a) Large, atomically flat area on top terrace. (b) The first pit (inside the box) formed after a pulse of (+3V, 20msec), tunnel current = 1.62nA. (b) The second pit formed under the same condition (inside the box 1). Note the repeated image of the pit (in box 2) due to a double tip. The first tip does not repeat since its distance from the terrace edge is greater than the distance between the double tips. (c) A mound formed after a pulse of (+3V, 5msec), tunnel current = 0.91nA.

4.4 RESULTS

4.4.1 Linear Decay in Time of the Monolayer Island

Figure 4.5 shows time-sequential STM images of a bilayer gold island. Figure 4.5(1)-(6) are images with the surface illuminated by a point light source at infinity, while Figures 4.5(7)-(9) are grayscale images with brightness representing the height. Figure 4.5(1) shows a large atomically flat area before a voltage pulse. The tip was then set at a spot on the flat surface and a pulse (+3Volt, 10msec.) was applied to the sample to make the mound shown in Figure 4.5(2). We can claim that the mound is deposited from the tip because we do not see a moat around the mound which is a sign of 'lifting' the mound out of the surface. 8 minutes after the pulse, the area was scanned again and the decay process was observed by comparing this image to the previous one. We zoomed in on the area around the mound and found that the mound is actually a layered structure of two monatomic gold islands. Figures 4.5(3)-(9) are additional time lapse images of the structure.

One might argue that the top island is a just tip artifact because the image shows that there is a triple tip. But, we can rule out this concern by following argument.: Looking at the image, we can easily tell the triple tip is aligned in the south-north direction because the repetition of image occurs in that direction (the line scans in the east-west direction.). Furthermore, we can tell the tip at the south end is closest to the sample since the STM constructs the image starting from the line at the north. First, the closest tip at the south scans over the top terrace. Right after the scan over the top terrace is finished, the tip moves to the lower terrace and is then pushed downward to maintain a constant current. But, as soon as the tip is pushed downward, the neighboring tip takes over the tunneling. Since this second tip is still over the top terrace, it images

Figure 4.5 Time-sequential STM images showing linear decay of two layer system. Frame (1) and (2) are images before and after a voltage pulse. Scan area : $(150nm)^2$ for (1) and (2), $(40nm)^2$ for (3)-(9). The time index of each image is as follows (minute:second) : (3) (00:00) (4) (09:23) (5) (24:17) (6) (34:48) (7) (37:05) (8) (48:30) (9) (50:43).

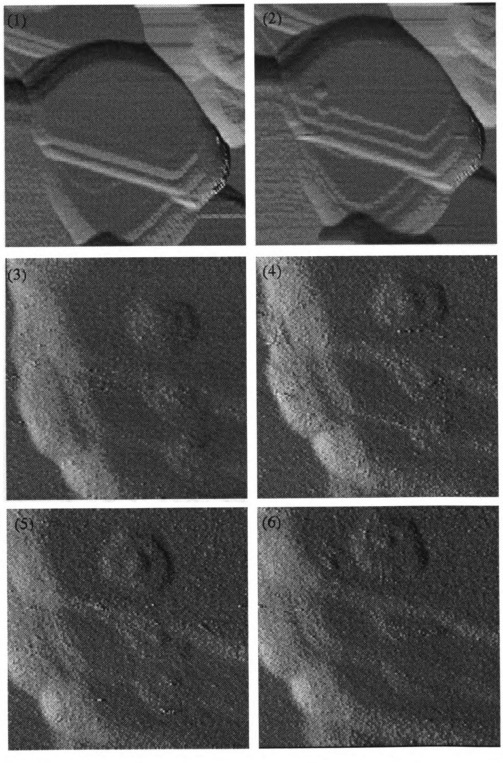

Figure 4.5

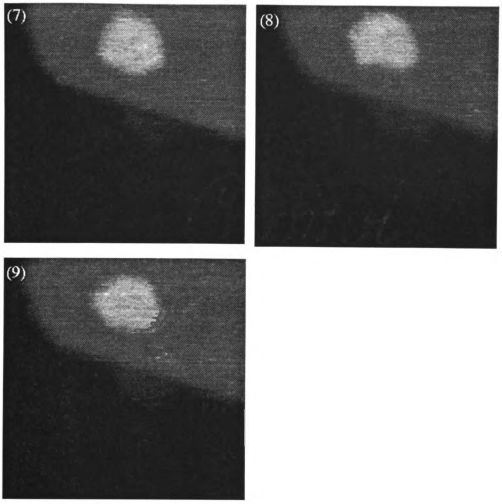

Figure 4.5 (cont'd).

the top terrace again, and so on. Figure 4.6 shows an illustration explaining the triple image. We now know there is no tip artifact in the first image of the highest terrace.

In Figure 4.7, the areas vs. time for both the top island and the second island are plotted. The data for the top island shows that the area decays linearly in time and it fits very well to a simple line given in formula (4.1) with the slope, m of -0.13 atoms per second (aps). The area of the second island increases during the decay of the top island then decreases after the top island disappears. Initially, the rate at which the second island is being fed by the atoms diffusing from the top island is greater than the rate at which the second island itself decays. D.R. Peal has suggested possible reasons for this difference in rate[13]. One possibility is that if the island edge is in contact with a line defect, the flow of atoms is obstructed along this contact zone. The other possibility is that since the mass flow is observed in air and not in UHV condition, the decay rate may be enhanced by adsorbates on the surface which lower the diffusion barrier in surface potential. In this case, the nonuniform coverage or the difference in the species of the adsorbates alter the decay rates for the different layers. The historical review and the experimental justification of the increase of the diffusivity on contaminated surfaces compared to non-diffusive behavior in UHV systems is well addressed in Reference 15.

Figure 4.8 is another series of STM images showing linear decay in a two layer system. In this case, a voltage pulse of +3Volt was applied for 10 milliseconds with a tunnel current of 2.0nm so that the tip produces pits and mounds on the surface. After the pulse, the tip was sharpened to produce a cleaner image compared to the image before the pulse.

The plot of the area vs. time for each island in the two layer system is presented in Figure 4.9 (a). A linear fit yields a decay rate of -0.27 aps for the top island. The decay rate of the second island during the decay of top layer is +0.01 aps and then changes to -0.27 aps as soon as the top island disappears. The same argument for

Figure 4.6 A schematic illustration showing the effect of a double tip. Arrows represent the tunneling site. The solid contour shows the image with a single tip. The repeated image due to a double tip is drawn with a dotted line. (Tip position 1) STM is imaging with a tip2. (Tip position 2) After this moment the tip is pushed downward to maintain a constant tunnel current. (Tip position 3) Tip1 takes over tunneling and images a part of the top layer again. (Tip position 4) Tip2 takes over the tunneling again and images the lower terrace.

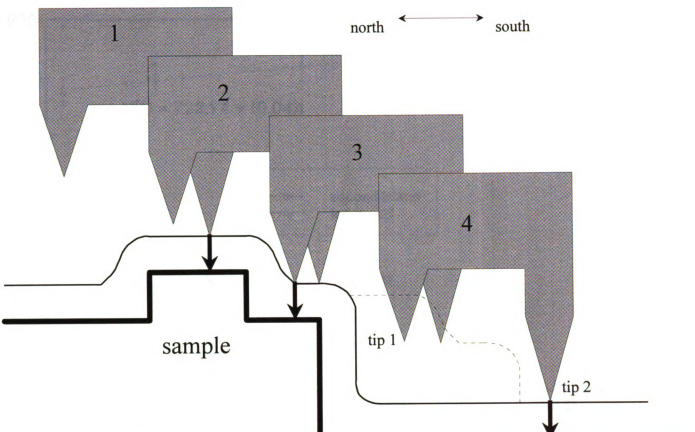

Figure 4.6

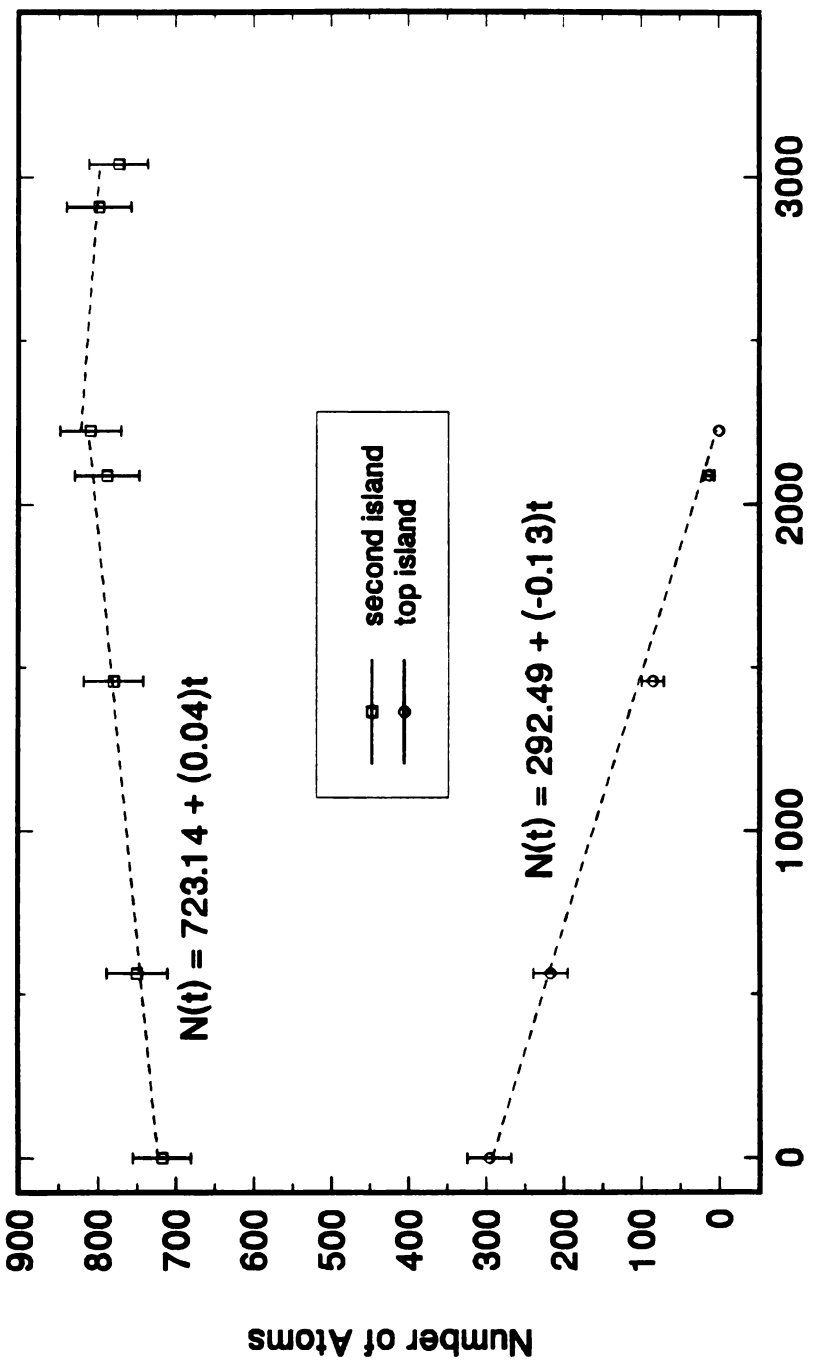

Figure 4.7 Areas vs. time for both top island and second island shown in Figure 4.5.

Figure 4.8 Time-sequential STM images showing linear decay of two layer system. Scan area = $(40nm)^2$. Frame (12) shows the location of the top island and the second island The time index of each images is as follows (minute:second): (1) (00:00) (2) (02:13) (3) (16:22) (4) (20:27) (5) (22:42) (6) (29:55) (7) (38:46) (8) (43:22) (9) (51:56) (10) (54:04) (11) (60:06).

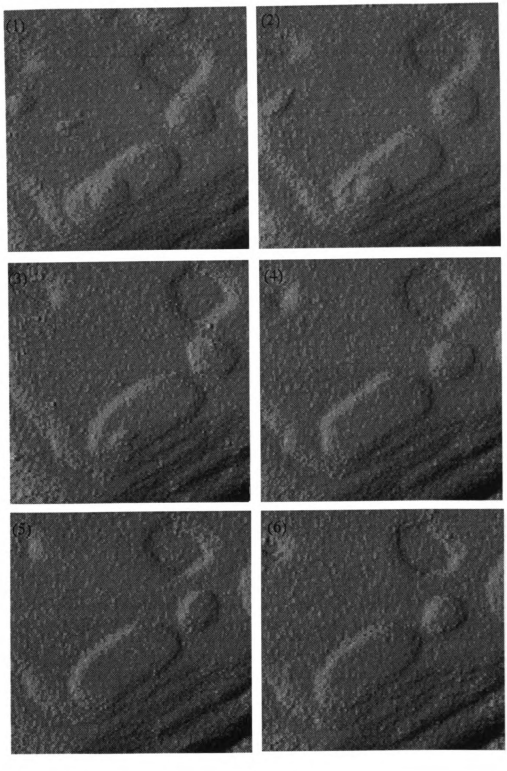

Figure 4.8

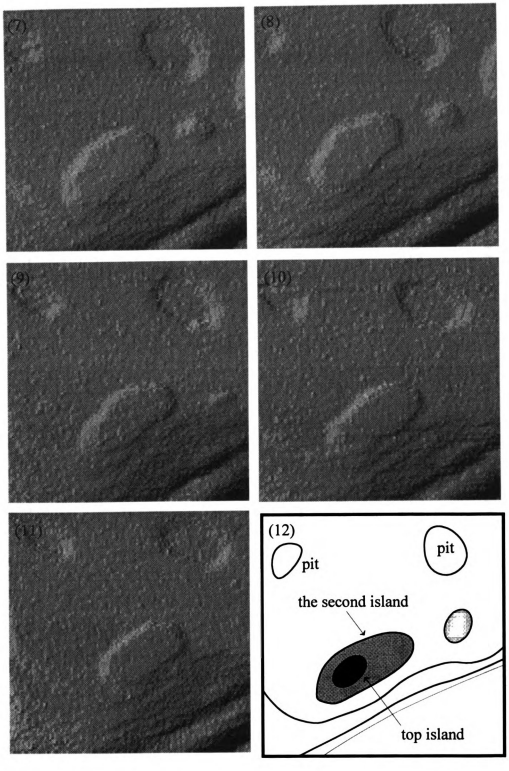

Figure 4.8 (cont'd).

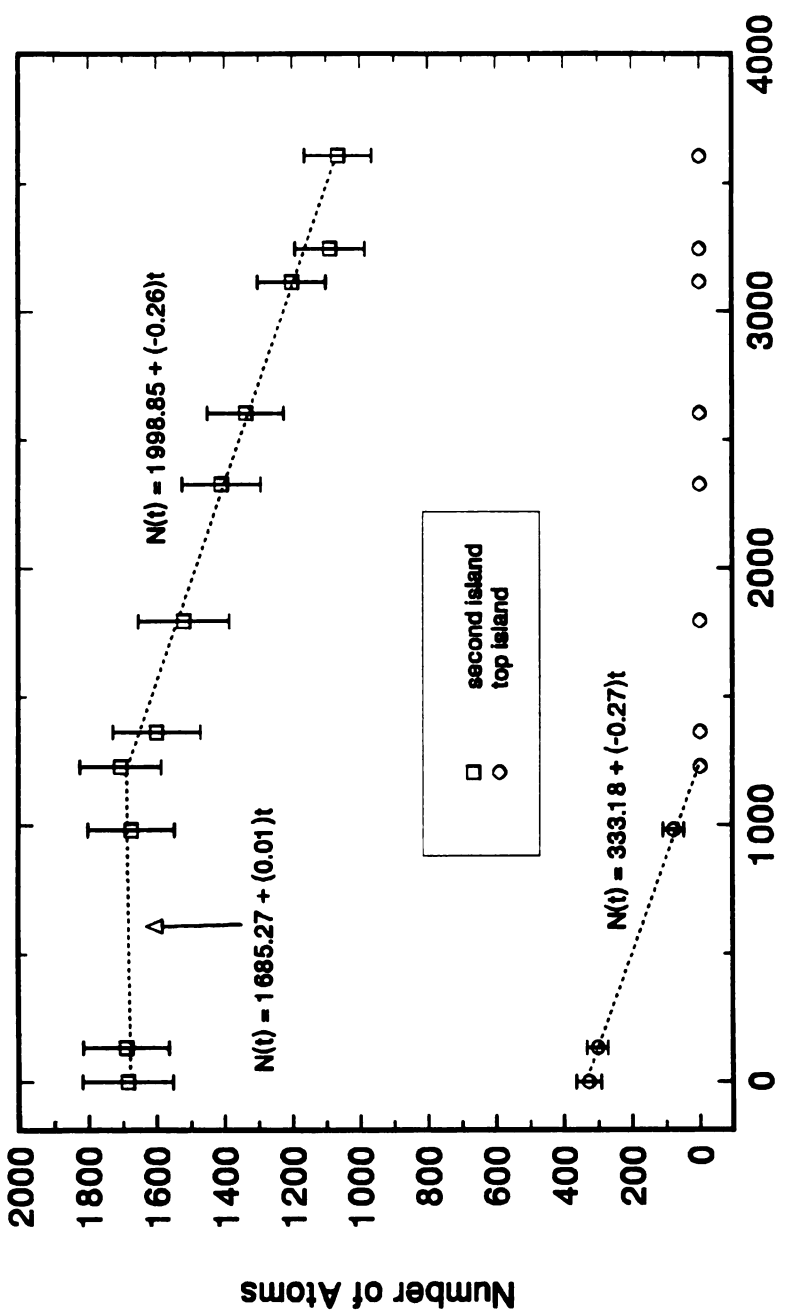

Figure 4.9 (a) The plot of the area vs. time for each island in two layer system of Figure 4.8.

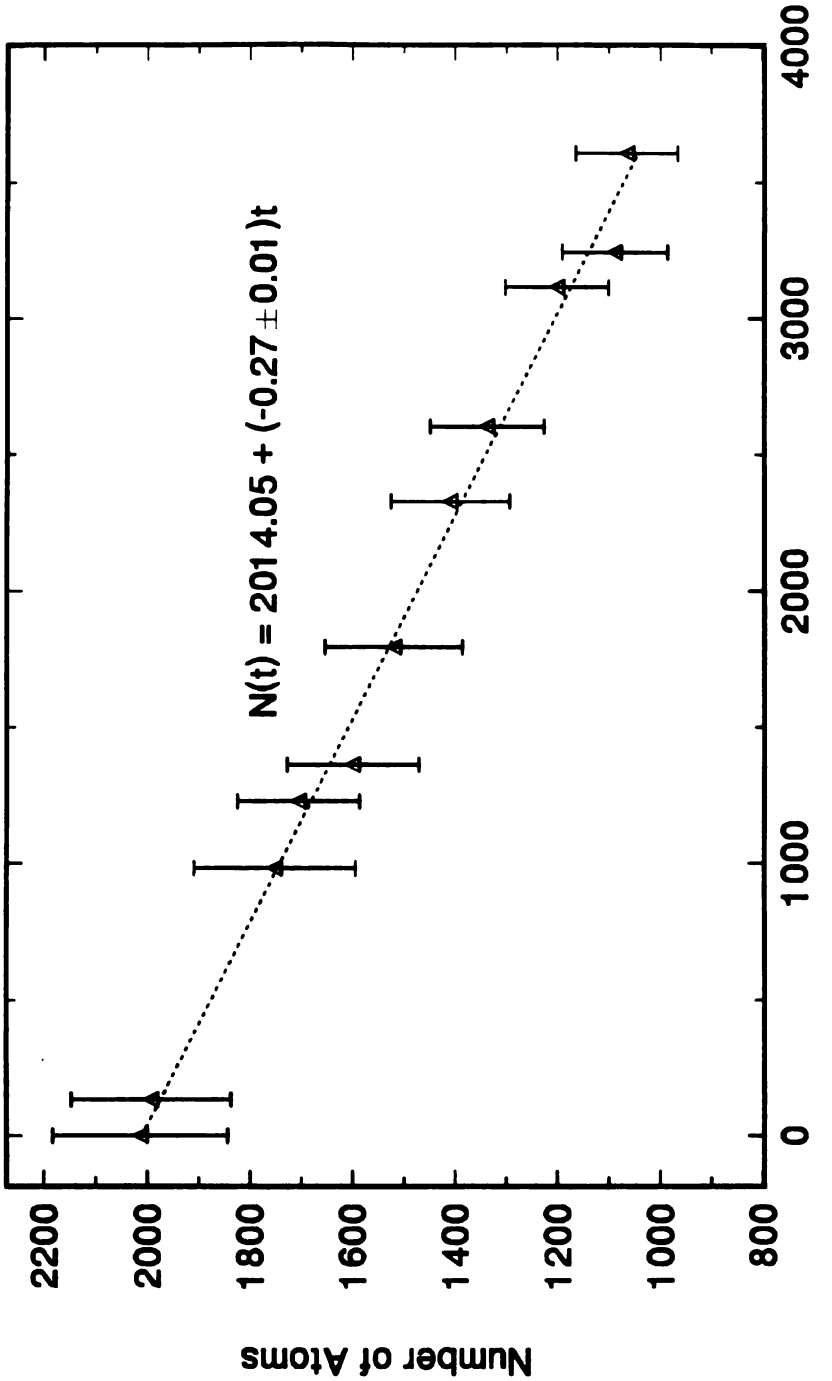

Figure 4.9 (b) A plot of total area of top and second island vs. time.

previous data can be applied for this case also. It is worth pointing out that the total area of the top and second islands also decays linearly since any atom diffused from this two layer system must have left from the edge of the second island. (See Figure 4.9 (b).)

4.4.2 Measurement of the Diffusion Coefficient from a Diffusing Mound

Schneider *et al.*[12] made a rough estimate of the diffusion constant on a gold surface at room temperature in air from the diffusing mound, assuming a gaussian shape of the mound which consists of non-interacting atoms. If we take h, the local height of the mound as a measurement of concentration of atoms, then we can write down the relation as

$$h(r) \propto \exp(-r^2/4Dt) \tag{4.4}$$

where t is the time passed since the formation of the mound (modeled as a delta peak at t=0), D is the diffusion constant, and r is the distance from the center of the mound.

The time lapse STM images of several diffusing mounds and healing pits are presented in Figure 4.10. The mounds and pits were produced by a voltage pulse of +4Volt with a duration of 10 milliseconds with a tunneling current of 2.0 nA. About 4 hours later, the pits are completely healed and the mounds have dispersed in the radial direction. At each time, the width, w of the biggest mound (width=3.32nm, height=17.54nm at t=0) is measured from the STM images. Here, the width of the mound is measured at the point where the height of the mound drops to 1/e times the mound peak height. From (4.4), we get $-w^2/(16Dt) = -1$ so that $D=(w^2/16t)^{1/2}$, and find D to be approximately 10^{-16} to 10^{-17} cm^2/sec.

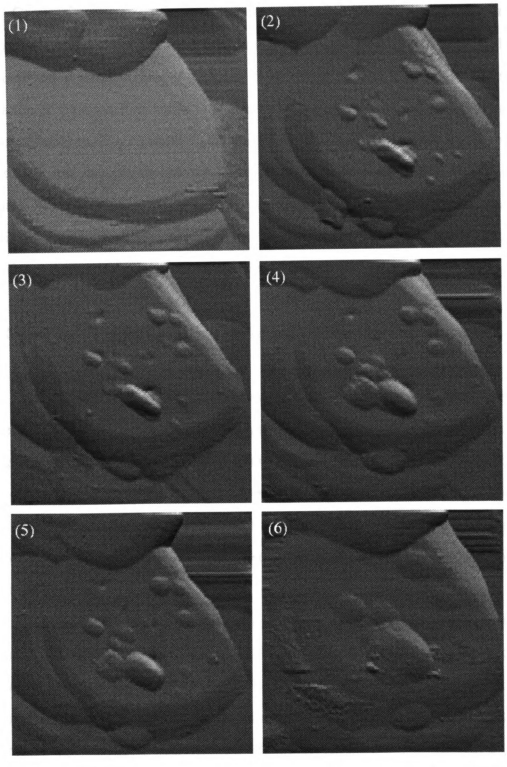

Figure 4.10 The time lapse images of diffusing mounds and healing pits. Scan area = $(200nm)^2$. The time index of each image is as follows (hour:minute:second): (1) (before the formation of structures) (2) (00:00:00) (3) (01:11:21) (4) (02:01:25) (5) (03:02:37) (6) (04:14:39).

Conventionally, a quantitative measurement of the surface self diffusion was made at high temperatures. In those experiments, the experimental value of the diffusion coefficient on a metal surface is different from author to author and depends on the orientation of the crystalline surface. However, all the data fall within a narrow band in the plot of ln(D) vs. T_m/T, where T_m is the absolute melting temperature of the metal.[9] Accordingly, we can extrapolate the diffusion constant at room temperature and our measured value is within the range although this non-interacting particle model is unrealistic. A more realistic measurement of the surface self diffusion coefficient from wandering monatomic terraces will be described in the next section.

4.4.3 Measurement of the Diffusion Coefficient from Moving Terrace Edges

The first direct STM observation of moving gold steps at room temperature were reported by Jaklevic *et al.*[14] in 1988. They produced monolayer pits on Au(111) surface by crashing the tip to the surface then found that the pits are filled by the diffusive atoms. Holland-Moritz *et al.*[15] also reported a more comprehensive study of moving gold steps on gold films evaporated on hot mica substrates. They concluded that the speed of step motion is very sensitive to levels of contamination during the sample preparation process.

Adopting their idea, we intentionally prepared a contaminated sample to see if there is active step motion. For the preparation of clean samples, we prebake a evaporation chamber for 12 hours at high temperature and pre-melt gold wire in the tungsten boat with the sample shutter closed before evaporation. To make an intentionally dirty sample, however, we evaporated 80nm of gold on 300C glass substrates without either prebaking the chamber or pre-melting the gold in the boat.

Another few monolayers of gold were evaporated after the sample was cooled to room temperature.

Figure 4.11 is a series of STM images of this contaminated sample showing the wandering of terrace steps due to surface diffusion. It is clear that thermodynamics is flattening the surface so that atoms in top terraces are flowing to lower terraces to fill the valleys. One interesting feature of these images is that the terraces split into small islands and the islands then disappear due to surface diffusion. In STM lithographically fabricated samples, however, the terrace decays by evaporating atoms from the perimeter sites isotropically in all directions. In heavily contaminated samples, atoms around contaminant sites may evaporate faster so that the terraces break into small islands first before they decay. The decay process of the second terrace in the frame (00:48:17) and (00:52:23) of Figure 4.11 clearly shows this.

We can estimate the surface diffusion constant from this data by a simple model as follows: Consider a system of monatomic layers whose neighboring adjacent steps are separated by an average distance l and the average distance between the active kink sites along each step is d. For the reasons discussed in Chapter 5, the atoms diffuse only from the higher layer to the lower layer. When an atom diffuses, an atom on the edge of the higher terrace detaches on a time scale of t_{det} and performs an unbiased random walk on the terrace between the higher and lower edges and eventually it either goes back to the home terrace and reattaches or falls downstairs and attaches to the lower edge. Let the time scale that the atom falls downstairs and attaches to the lower edge be t_{esc}. (See Figure 4.12 for the illustration of the system.)

The mass transfer diffusion coefficient is defined by[9]

$$D_M = (n/N)D_o \tag{4.5}$$

Figure 4.11 The time sequential STM images of the contaminated sample showing wandering of terrace steps due to surface diffusion. The time index of each image is (hour:minute:second). Scan areas : (00:00:00)-(00:29:47);$(120nm)^2$, (00:31:52)-(00:34:43);$(150nm)^2$, (00:36:54)-(00:41:03);$(120nm)^2$, and $(100nm)^2$ for the rest of all..

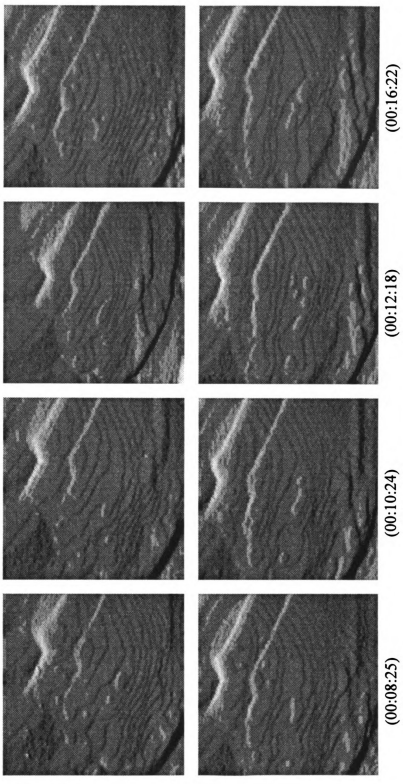

Figure 4.11

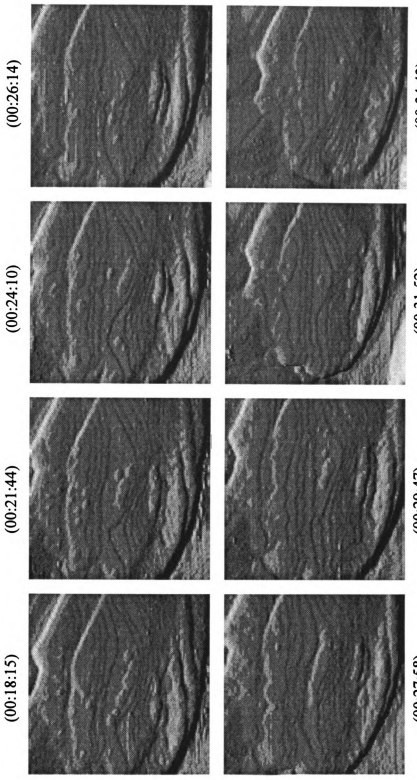

Figure 4.11 (cont'd).

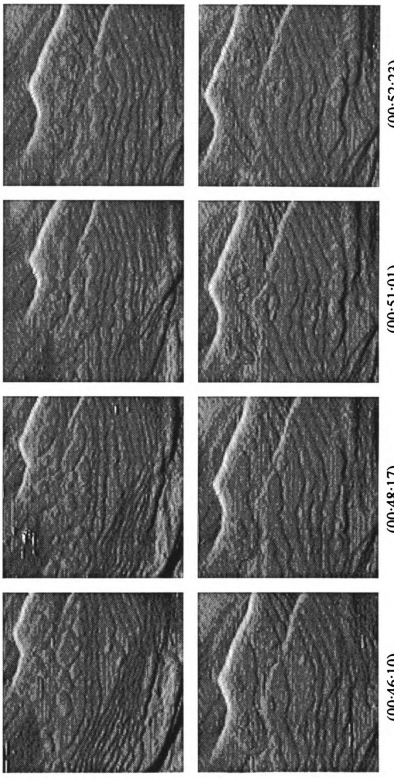

Figure 4.11 (cont'd).

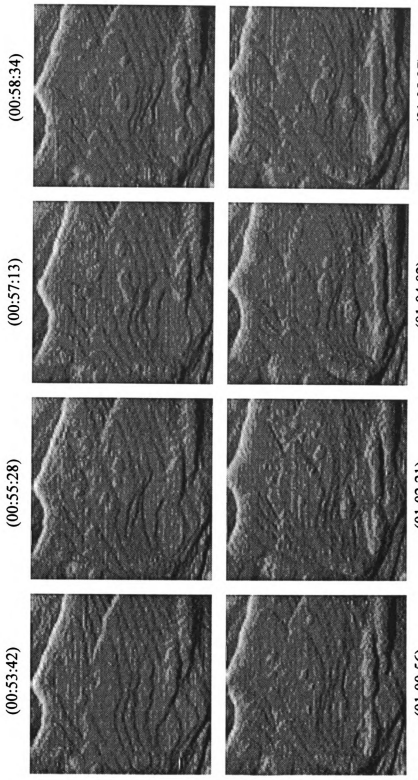

Figure 4.11 (cont'd).

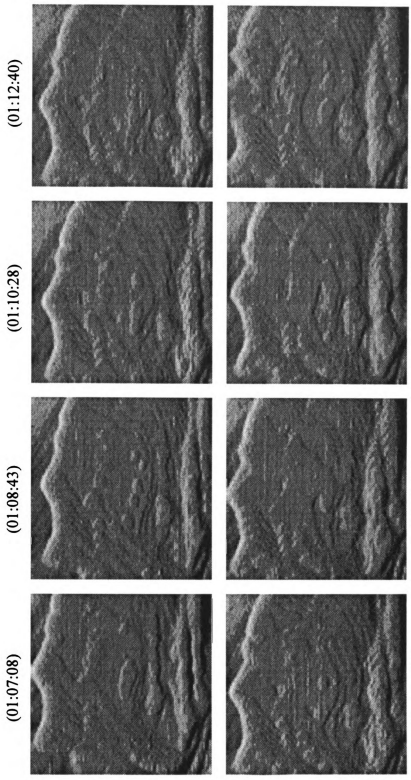

Figure 4.11 (cont'd).

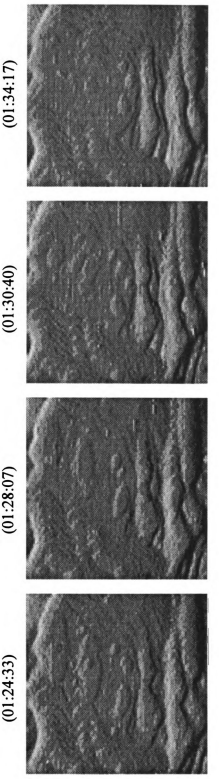

Figure 4.11 (cont'd).

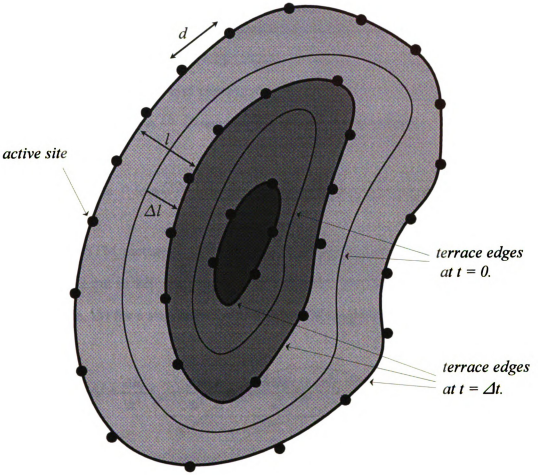

Figure 4.12 A schematic illustration of the diffusing terraces. The steps move Δl after Δt. The greyscale represents the height of each terrace at time of Δt (the darker, the higher).

where n is the density of diffusers, N is the density of available diffusion sites, and D_o is a diffusion constant for one diffuser which is approximately $l^2/4t_{esc}$. Since we know that $N=1/a^2$ and $n=1/ld$ with a as a lattice constant and l,d as parameters defined above, (4.5) can be rewritten as $D_M=(a^3/d)(1/4t_{det})$. It can be shown that a 1D random walker, taking steps of unit length and starting at x=1, has a probability $1/x_o$ of reaching $x>x_o$ before returning to origin.[16] Consequently, we obtain the relation

$$t_{esc} = t_{det}\,(l/a). \tag{4.6}$$

In the STM pictures in Figure 4.11, we observe that the steps move an average distance of 6.2 nm in 120 seconds, i.e. $\Delta l = 6.2\text{x}10^{-7}$ cm and $\Delta t = 120$ seconds. Using (4.6), the time, Δt for a step to retreat a distance Δl is rewritten as

$$\Delta t = \frac{\Delta l d}{a^2} t_{esc} = \frac{\Delta l d}{a^2}\frac{l}{a} t_{det} = \frac{l \Delta l d}{a^3} t_{det}$$

Accordingly, D_M is expressed with our observable parameters of Δl and Δt as

$$D_M=(\Delta l)^2/4\Delta t\,. \tag{4.7}$$

here we used the approximation of $\Delta l \sim l$ based upon the STM images. The estimated value of the mass transfer diffusion coefficient is $8.0\text{x}10^{-16}$ cm^2/s.

A time series of STM images of a five days old gold film evaporated by the clean procedure is displayed in Figure 4.13. Though not all the spots we imaged showed the surface diffusion, the shrinkage of the stack of gold monolayers was seen in one spot of the sample. After two and a half hours, the top terrace area reduced to a quarter of the initial area. We also observe a strong anisotropy in the surface diffusion so that

Figure 4.13 Time series STM images showing the shrinkage of stacked monolayer gold mesas in the sample prepared by clean procedure. The time index of each image is (hour:minute:second). Scan area = $(100nm)^2$.

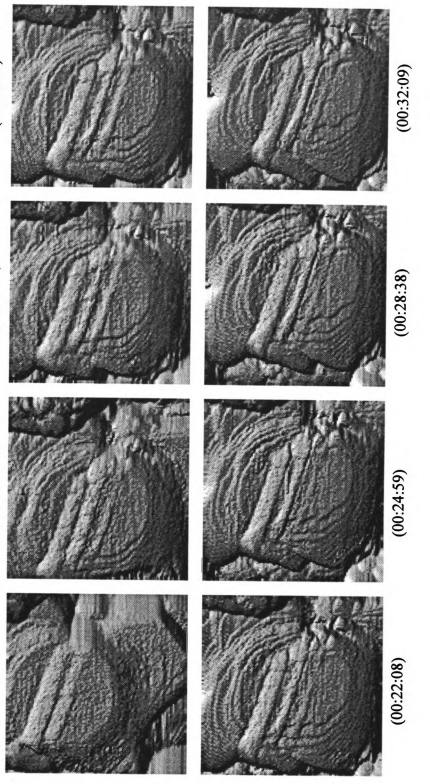

Figure 4.13

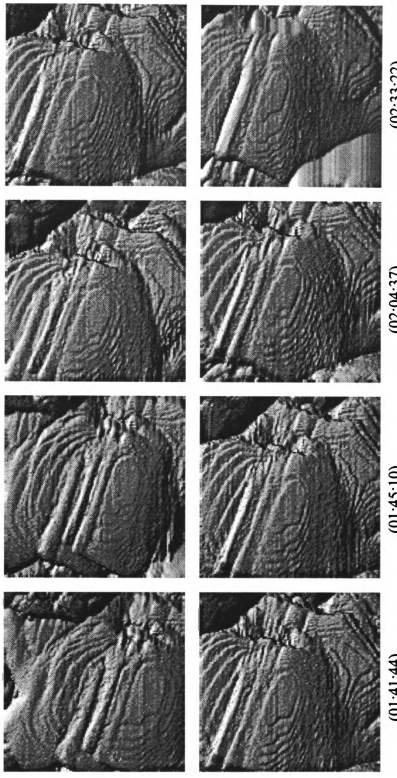

Figure 4.13 (cont'd).

originally well rounded terraces end up with elongated terraces. As shown in the decay of the two terrace system in section 4.4.1, the decay rate of each terrace gets smaller as we go to lower terraces since higher terraces feed the lower ones with diffusive atoms. In this relatively clean sample, the surface diffusion is considerably slower than in the contaminated sample. Using the average values of Δl = 4.5 nm and Δt = 1100 seconds, equation (4.7) yields the mass diffusion constant of $4.6 \times 10^{-17} cm^2/sec$, one order of magnitude lower than the D of the contaminated sample.

In summary, we fabricated small gold islands and pits on an atomically flat gold surface by a voltage pulse. The sequential STM images of the fabricated structures show that the area of the monolayer gold island decays linearly in time at room temperature in air. To measure the surface diffusion constant, the relaxation of the stepped gold surface toward equilibrium is observed. From the series of images showing moving monatomic steps, we obtain a diffusion constant of $6.2 \times 10^{-17} cm^2/sec$ for the clean samples, while the heavily contaminated sample yields 8.6×10^{-15} $cm^2/seconds$. These values are in good agreement with reference 17.

REFERENCES FOR CHAPTER 4

1 M. Volmer and I. Estermann, Z. Physik 7, 1 (1921)

2 W. Kossel, Nach. Ges. Wiss. Gottingen **K1** 135 (1927); I.N. Stranski, Z. Phys. Chem. **136**, 259 (1928)

3 Jan-Olle Malm and Jan-Olov Bovin, Surf. Sci. **200**, 67 (1988)

4 J.A. Panitz, J. Phys. **E15** 1281 (1982)

5 G. Ehrlich and F.G. Hudda, J. Chem. Phys. **44**, 1039 (1966)

6 H.W. Fink and G. Ehrlich, Surf. Sci. **143**, 125 (1984)

7 J.K. Gimzewski, R. Berndt, and R.R. Schlitter, Surf. Sci. **247**, 327 (1991)

8 D.R. Peale and B.H. Cooper, J. Vac. Sci. Tech. A **10**, 2210 (1992)

9 H.P. Bonzel, edited by NATO Adv. Study Inst. Ser. Sec. **B 86**, 195 (1983)

10 The x-ray diffraction was performed on a Rikagu Diffractometer using Cu Kα radiation.

11 R.E. Emch, J. Nogami, M.M. Dovek, C.A. Lang and C.F. Quate J. Microscopy **152**, 129 (1988)

12 J. Schneider, R. Sonnenfeld, O. Marti, P.K. Hansma, J.E. Demuth, and R.J. Hamers, J. Appl. Phys. **63(3)**, 717 (1988)

13 D.R. Peal, Ph.D. Thesis, Cornell University, 1992 (unpublished)

14 R.C. Jaklevic and L. Elie, Phys. Rev. Lett., **60(2)**, 120 (1988)

15 E. Holland-Moritz, Joseph Gordon II, G. Borgers, and R. Sonnenfeld, Langmuir 7, 301 (1991)

16 Eugene Capriotti, private communication.

17 P. Wynblatt and N.A. Gjostein, Surf. Sci. **12**, 109 (1986)

Chapter 5

MONTE CARLO SIMULATION OF THE LINEAR DECAY OF ISLANDS ON METAL SURFACES

5.1 ABSTRACT

STM studies of mass flow on (111) Au have shown that the rate of decay of the area of monolayer islands is linear in time. We demonstrate by Monte Carlo simulation that a proper accounting of the detachment and reattachment rates of kink site atoms produces a linear decay. In our simulation, adatoms emitted from kink sites on mesa edges execute an unbiased random walk and may reattach to the home mesa or be absorbed by an outer ledge, possibly after several reflections from the step down at the outer ledge. The linear decay of mesa areas is found to be rather insensitive to variations in the probability of reflection from the outer ledge.

5.2 INTRODUCTION

In an STM study of surface mass flow on (111) gold, Peale and Cooper have reported[1,2] that, at room temperature in air, the area of single monolayer islands decays linearly with time. We have done similar experiments and find the same results[3] as shown in Chapter 4. A linear decay of island areas is puzzling at first sight. If the rate of mass loss is proportional to the circumference of the island (a natural assumption if the number of kink sites per unit length along the perimeter is constant), then the number N

of atoms decays as $dN/dt \propto -(N)^{1/2}$, and the decay is parabolic, not linear. In this Chapter we show, by Monte Carlo simulations, that a proper accounting of the kink atom detachment and reattachment rates leads to a linear decay.

We have developed two distinct computer models, which produce nearly identical results. Our models are based on the assumption that the potential near a monatomic step has the form shown in Figure 5.1 with a deep well at the base of the step (site B), small activation barriers between shallow wells far from the step, and a somewhat higher shallow well at the site on the top terrace adjacent to the step (site A). Site A is somewhat higher because it lacks a second nearest neighbor. As a consequence of the asymmetry in this potential, a kink site atom in the deep well B is more likely to activate out onto the lower terrace than up onto the higher terrace. Also, an adatom approaching the step from the left has some tendency to be reflected, while an adatom approaching the step from the right has no such tendency and will be captured in the deep well B. The qualitative form of this potential is supported by embedded atom method calculations[4]. Also, reflection of an adatom by a step down has been observed on metal surfaces by field ion microscopy[5].

Because the terrace corrugation is small, the time for an adatom to random walk between ledges is very fast compared to the mean time for a kink site atom to detach[6,7]. The atoms at the surface of a perfect crystal are vibrating at some frequency ν_D which can be estimated by the relation $h\nu_D=kT_D$, where T_D is the Debye Temperature of the solid, h is a Planck's constant, and k is Boltzmann's constant. For gold, $\nu_D \sim 3\times10^{12}$ sec^{-1} is obtained with a value of $T_D=165K$.[8] Sometimes thermal energy gives the atom sufficient energy to leave its initial site and hop to a neighboring site. The frequency ν with which an atom will jump from the original site is expected to be $\nu=\nu_D\exp(-E_b/kT)$, where E_b is the energy barrier for the atom to surmount during the hopping. Accordingly, the time scale for the atom to hop from one site to its nearest neighboring

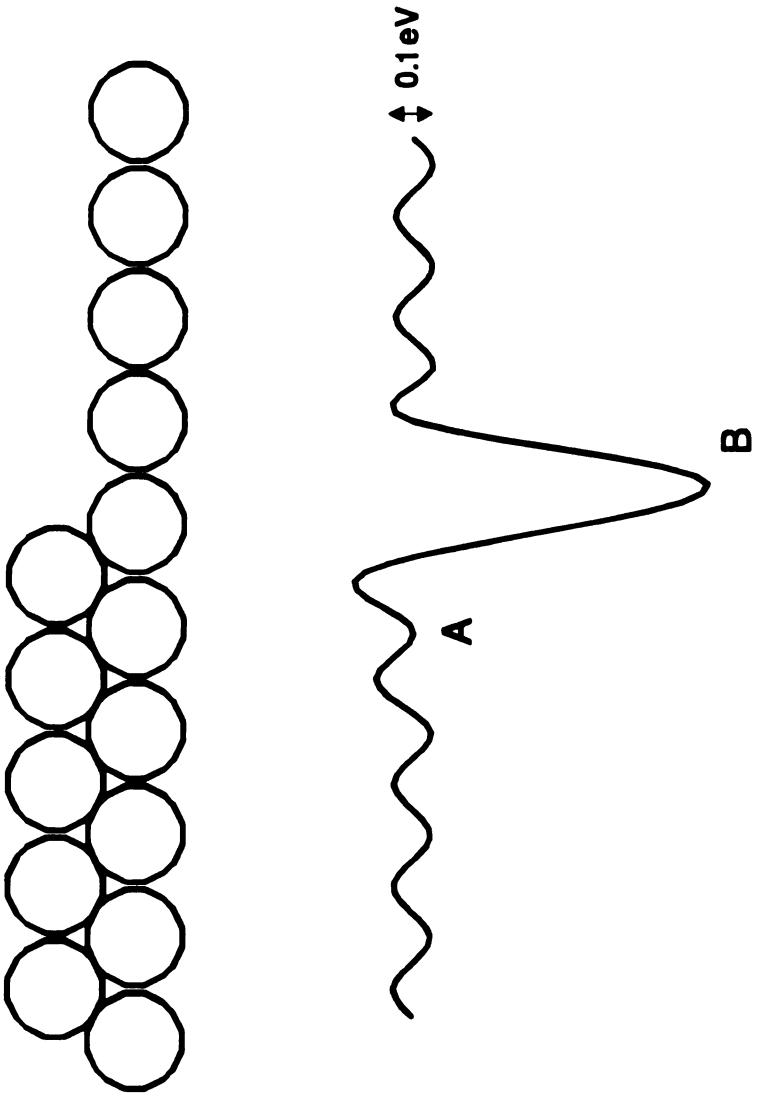

Figure 5.1 Potential near a monatomic step.

site is $\tau=\nu^{-1}=(1/\nu_D)\exp(E_b/kT)$. For (111) Au at room temperature, the mean time for a kink atom to detach is 10^{-5} to 10^{-2}s depending on the depth of the well at point B (E_b = 0.45-0.65 eV). On the other hand, with an activation barrier E_b=0.1eV, the time for an adatom to random walk a distance of one lattice constant is about 10^{-11}s so that an adatom on a (111) surface wanders ten's of nanometers (i.e. hundred's of lattice constants) in about $10^{-11}x(100)^2 = 10^{-7}$s. Consequently, at low temperatures ($T < 0.25\ T_{melting}$), the rate-limiting step in mass flow is the detachment of kink atoms and there is rarely more than one adatom on a given terrace at any time.

The linear decay may be understood qualitatively as follows. An adatom emitted from a kink site on the edge of a mesa is quite likely to reattach somewhere along the mesa's perimeter after a brief random walk. Only occasionally do adatoms wander to the outer ledge of the terrace before encountering the perimeter of the home mesa. However, this high reattachment rate drops as the mesa shrinks, because the wandering adatoms are less likely to encounter the smaller mesa. The dropping reattachment rate counterbalances the dropping emission rate as the perimeter shrinks and nearly linear decay results.

5.3 MODELS AND RESULTS

5.3.1 A Hybrid Lattice-Continuum Model

In our first model, we assume that the number of kink sites on the perimeter of an island is proportional to the perimeter length. We also assume that all kink sites have the same constant probability per unit time to detach so that the mean time between detachment events is inversely proportional to the perimeter length. In this model,

which is a hybrid lattice-continuum simulation, a mesa is represented by a circle I of radius R_i centered on the origin. R_i is determined by an integer N representing the number of atoms in the mesa: $R_i = (N/\pi)^{1/2}$. A larger circle O of fixed radius R_o, also centered on the origin, represents an outer ledge which can capture adatoms emitted by I. A walker, representing an atom detached from a kink on the perimeter of I, is released from the smallest positive integer position on the x-axis outside I and begins an unbiased random walk on the xy lattice, jumping to one of its 4 nearest neighbors in each step. If the walker crosses the outer circle O before crossing I, then it may be absorbed with probability (1-k) or it may reflect with probability k and continue its meandering trek. If it is absorbed by O, the time is advanced by $\Delta t = N^{-1/2}$ (the inverse of the mesa circumference), N is then reduced by 1, the radius of I is reduced accordingly, and a new walker is released from the smallest integer position on the x-axis outside the now-smaller circle I. The time increment Δt represents the mean time between detachment events, assumed inversely proportional to the circumference of I and the number of kink sites.

During its random walk, the adatom may undergo multiple reflections from O before being absorbed by O, or it may return to I after one or more reflections from O, or (most likely) it may return to I without reaching O. If the walker crosses the inner circle I, it is immediately absorbed, the time is advanced by $\Delta t = N^{-1/2}$, N is unchanged, and a new walker is released from the starting point just outside I. The process repeats until I completely evaporates, while N is recorded as a function of time.

Note that our model assumes that successive walkers do not interact, which is the case if the time between detachment events is long compared to the time of the random walk. Also, duration of the random walk does not affect the advancement of time in the simulation. The total time in the simulation is the sum of the times between successive

detachment events. The random walk proceeds "in parallel" with the wait until the next detachment event.

Figure 5.2 displays the results of this simulation for an inner circle of starting radius near 20 (N=1257), outer circles of radius 25, 50, 100, and 200, and a reflection coefficient k=0 (walkers always absorbed upon contact with the outer circle). For outer circles large compared to the inner circle, we see that the mesa area decay is very nearly linear, but as R_O approaches the inner circle's starting radius R_i, the mesa decay becomes more parabolic. A smaller outer circle captures adatoms more effectively, resulting in a lower reattachment rate and a net evaporation rate which is more dominated by the rate of emission, leading to a more parabolic decay.

Figure 5.3 displays the results of the same simulations, but with a reflection coefficient k=0.95. For larger outer circles, the decay is only slightly slower than the k=0 case and is still nearly linear. The linear decay is insensitive to k because once the walker has wandered to the outer circle, it is very likely to undergo multiple reflections and be absorbed by O before finding the small inner island.

5.3.2 A Cubic Lattice Solid-On-Solid Model

Next we describe a cubic lattice solid-on-solid model, similar in spirit but more realistic in detail than the first model. The initial configuration is a stack of mesas, concentric circular terraces separated by monatomic steps. To specify the condition of each atomic site, two two-dimensional arrays, T(x,y) and E(x,y) are used. T(x,y) represents the occupied site at position (x,y), and E(x,y) represents the empty site right above each occupied one. Introducing E(x,y) is essential since the coordination numbers for the neighboring empty sites are to be specified before an atom makes any movement toward one of its nearest neighboring sites. We then assign a value to each array

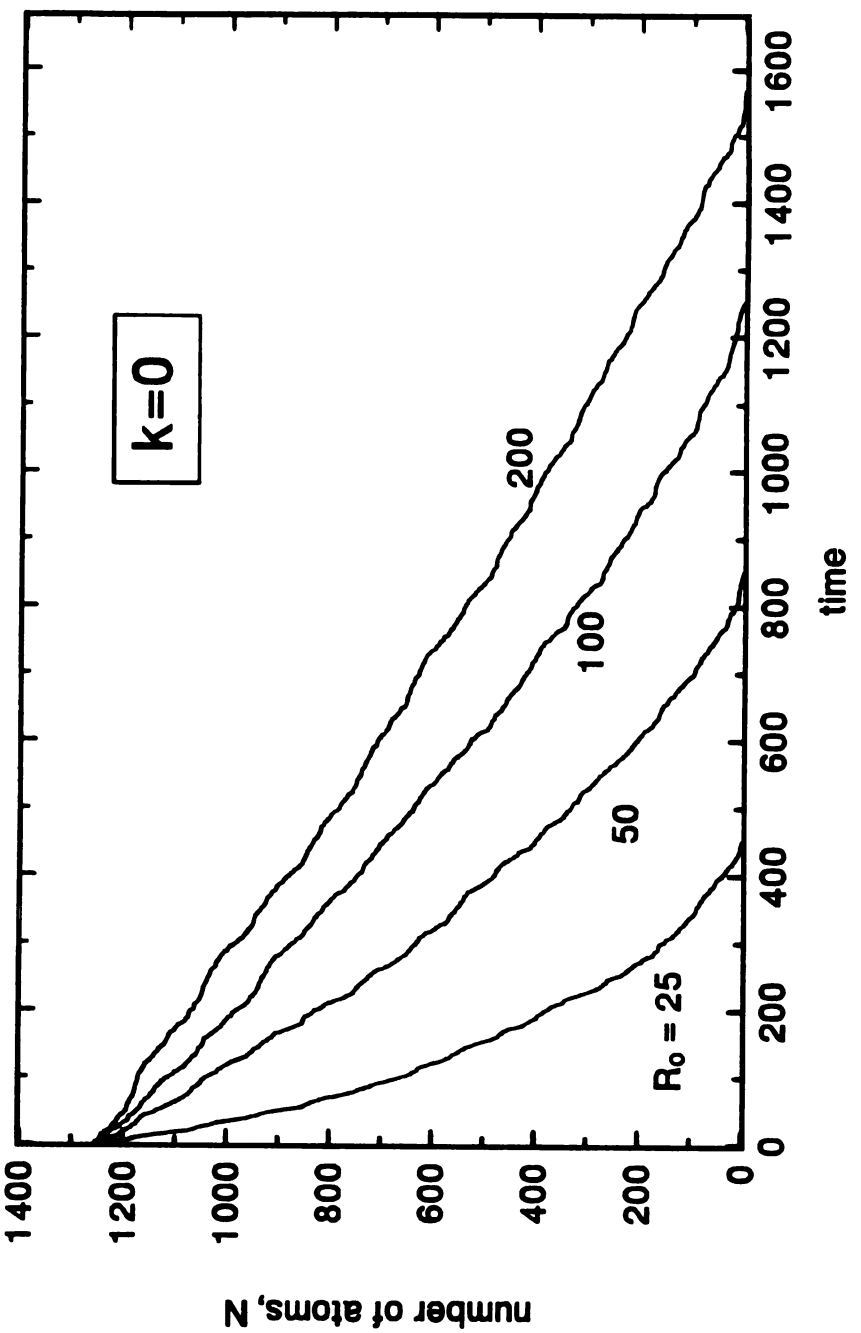

Figure 5.2 Decay of an island of radius 20 with outer absorbing circles of reflection coefficient k=0.

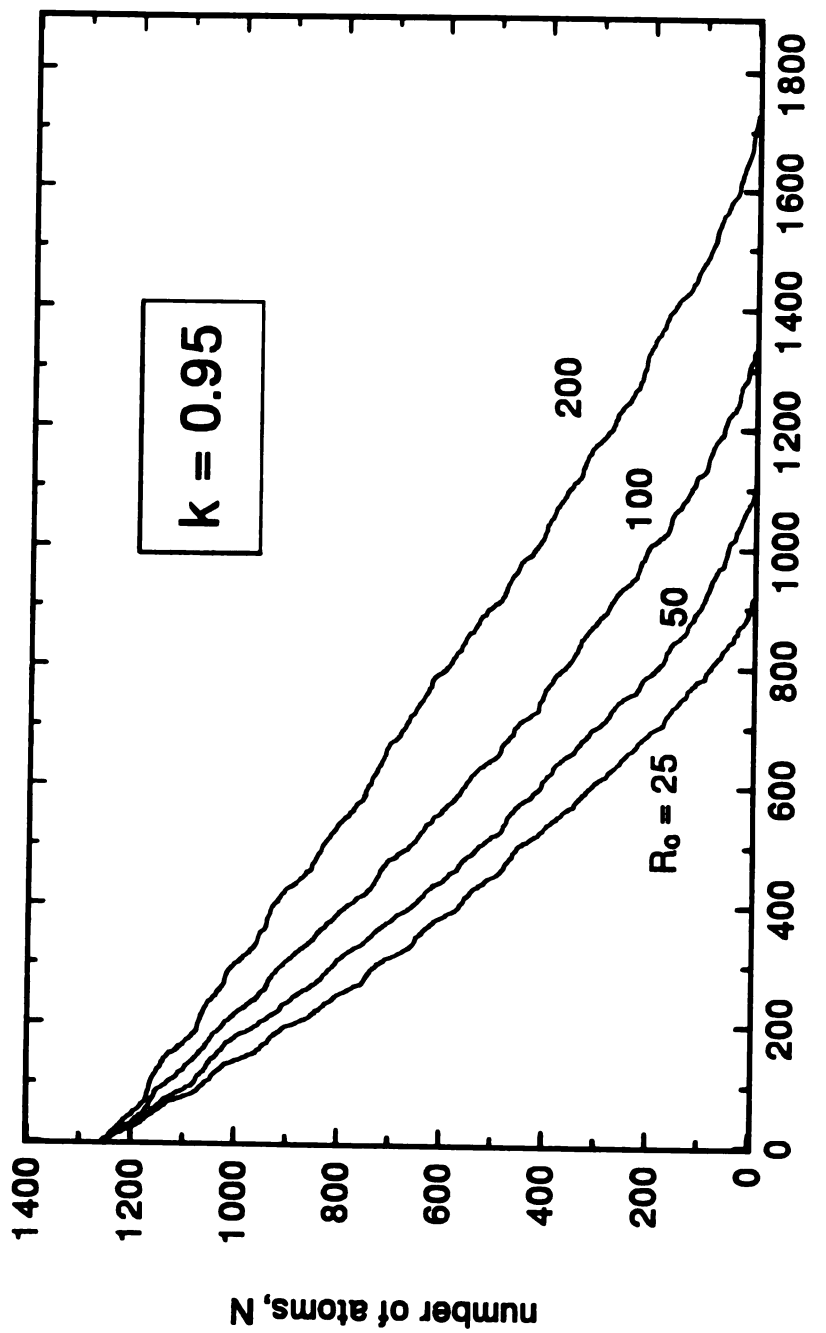

Figure 5.3 Decay of an island with outer absorbing circles of reflection coefficient k = 0.95.

variable according to the physical situation of each site as follows. The first two digits of the value show a local coordination number of an atom which is calculated by weighting 1st, 2nd, and 3rd nearest neighbors 9:3:1 (approximately the ratio in a Van der Waals solid). In three dimensional lattice cubic model, the first nearest neighbors are adjacent atoms that share a side of the cube, the second nearest neighbors share an edge, and the third nearest neighbors share a corner. The third digit of the array variable represents the terrace number, defined as 1 is for the top terrace, 2 is for the next lower terrace, and so on.

During the simulation, a list of "active" sites on the perimeters of the mesas is maintained. Active sites are those with a coordination number fewer than 49, in other words, fewer than 3 in-plane nearest neighbors including kink and corner sites as shown in Figure 5.4. At the start of the simulation, an atom is chosen at random from the list of active sites. The atom detaches from its mesa by jumping one step away from the perimeter and begins an unbiased random walk, stepping to any of its empty in-plane 1st or 2nd nearest neighbor sites. An atom is detached from a mesa if it has no nearest neighbor in-plane, even though it may have a second nearest neighbor in-plane. As in the lattice-continuum model, a detached atom may re-attach to its home mesa, or it may attach to the perimeter of an outer mesa by jumping down one level, possibly after several reflections from the step. Hops up onto higher terraces are not allowed; hops down to lower terraces are allowed with probability (1-k).

When the meandering atom attaches to a mesa, it explores the perimeter for some time, searching for a highly coordinated site, and comes to rest when it finds a local maximum in bond number (i.e. local maximum of the coordination number). This perimeter search procedure is required to keep the mesas compact as the simulation proceeds. If the wandering atom were to stick where it first hits a mesa, the mesas would develop a highly ramified, fractal shape, as in diffusion limited aggregation. Again, in

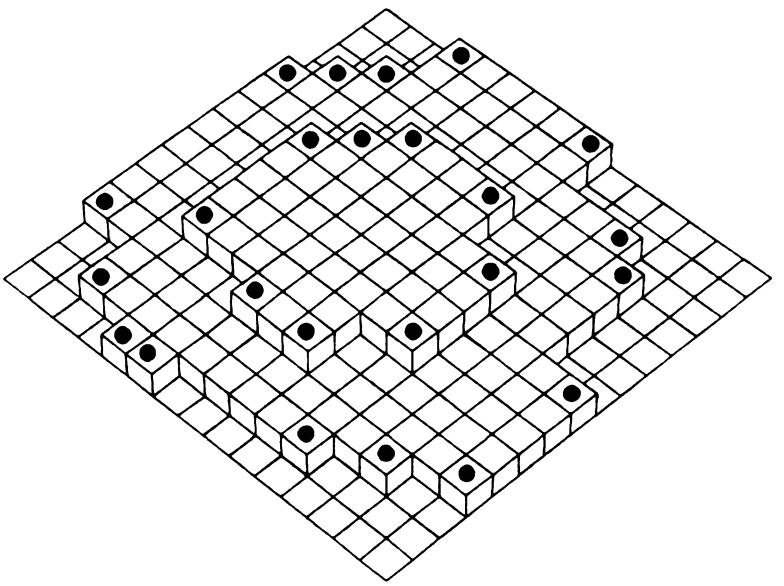

Figure 5.4 Two stacked mesas in the cubic lattice solid-on-solid model. Active sites are marked with a dot.

computing the local coordination of a perimeter atom, we weight 1st and 2nd nearest neighbor bonds 3 to 1. In searching for a final resting place along the perimeter, the atom random walks for up to 50 steps (an arbitrary number) and is allowed to temporarily reduce its second nearest neighbor count by one in order to move around corners. If the atom has not found a local bond number maximum after 50 steps, as in the case of a atom exploring the edge of square mesa, the atom stops.

When the walking atom finally comes to rest, the time is advanced by $\Delta t = 1/B$ where B is the total number of active sites in the system of mesas. The list of active sites is then updated, and a new walker is chosen at random from the updated list. Maintaining the list of active sites requires some ingenuity, since old active sites disappear (either evaporate or are covered by new atoms) and new ones appear as the simulation proceeds. In this cubic lattice simulation, as in the simpler continuum-lattice model above, we assume a constant probability per unit time that an active site will detach. Hence, the mean time between detachment events is inversely proportional to the number of active sites. Note that, in this lattice model, we do not need to assume that the number of kink sites is proportional to the mesa circumference.

The number of active sites, log of $N(t)_{active}$ vs. log of total remaining number of atoms, N(t) is plotted in Figure 5.5 from the simulation of the decay of an initially circular mesa with a beginning size of 3800 atoms. From this plot, to avoid an error due to a size effect of the small island, we fit the data down to N(t)=400 and obtained

$$N_{active}(t) \sim (N(t))^{0.502 \pm 0.006}$$

Here, the number of active sites is proportional to the island perimeter.

One might argue that corner atoms should detach more often than kink atoms since corners have only 1 in-plane 2nd nearest neighbor, while kinks have 2. However,

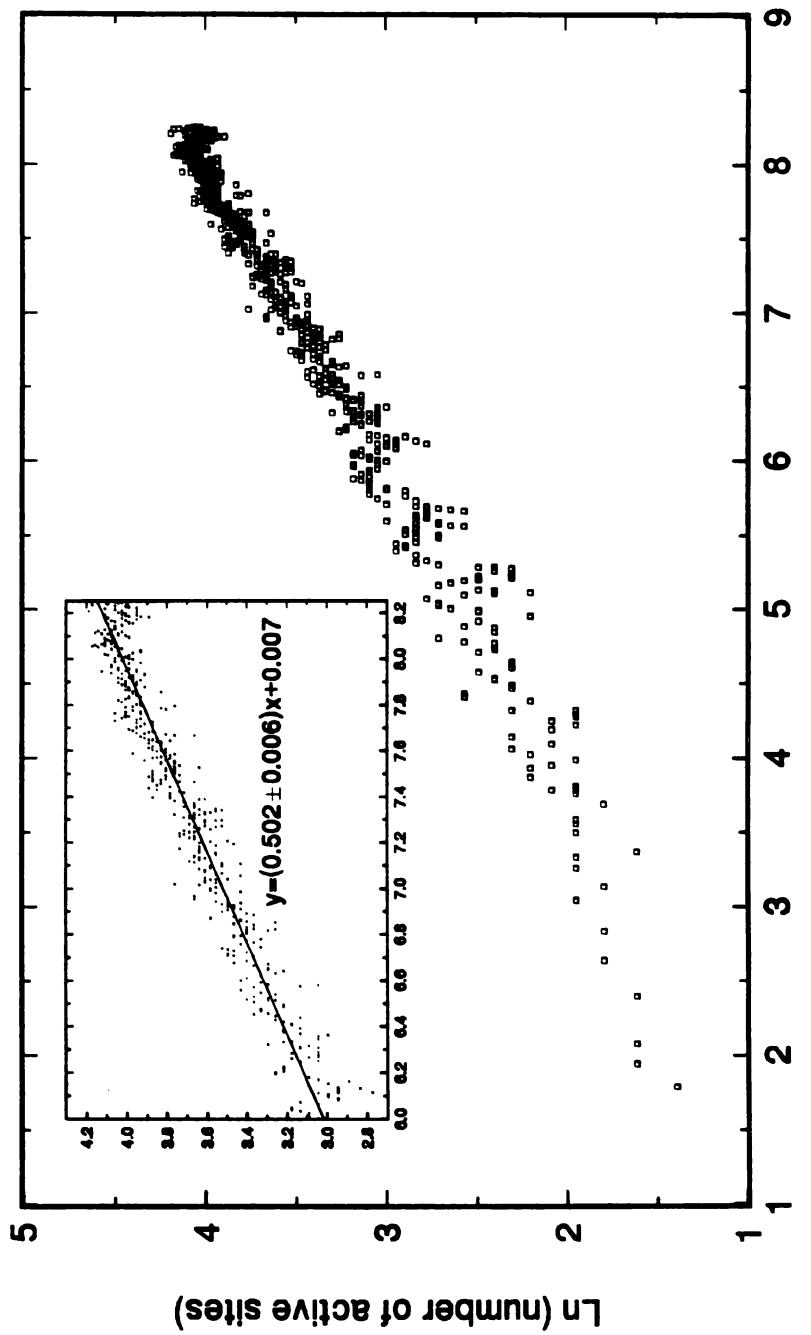

Figure 5.5 Plot of log of the number of active sites vs. log of total number of remaining atoms in a mesa during the simulation. The inset shows fit of the data to a line y=ax+b.

for reasons of simplicity, we make no such distinction. We note that for the (111) face of an fcc lattice, corner and kink sites have very similar local coordinations, each with 3 nearest neighbors in-plane. Occasionally, an active site with a single in-plane nearest neighbor is produced. This occurs when one of two adjacent kink sites detaches, leaving behind a ledge atom (see the lower left of the bottom mesa of Figure 5.5). Our simulation makes no distinction between such ledge atoms and other active sites, although it would be more realistic to allow ledge adatoms to explore the mesa perimeter, seeking a kink site. We believe that because such ledge active sites are rare, their occurrence does not significantly effect our results.

This cubic lattice model produces results which are nearly identical to the results of the simpler lattice-continuum model. The area of a single isolated mesa decays nearly linearly with time if it is on top of a larger mesa with a radius at least twice the starting radius of the smaller top mesa. As before, this result is rather insensitive to the value of the reflection coefficient k, at least for $k < 0.95$. Figure 5.6 displays areas vs. time for the top mesa of a three mesa stack with beginning sizes of 200, 800, and 2500 atoms with several k values of 0, 0.5, 0.85, and 0.9. Only k=0 case shows a slight parabolic behavior.

Our lattice model produces interesting behavior for a series of stacked mesas. Figure 5.7 shows area vs. time for the top two mesas of a three mesa stack with beginning sizes of 400, 1600, and 6400 atoms. The bottom mesa (not shown in the figure) is surrounded by an absorbing circle of radius 1.5 times the radius of the bottom mesa. The reflection coefficient $k = 0.90$. While the top mesa decays linearly, the middle mesa decays slowly at first and then more rapidly when the top one has disappeared. This is because the middle mesa is at first fed by the top one. This is precisely the behavior that has been observed experimentally for stacked mesas on (111)

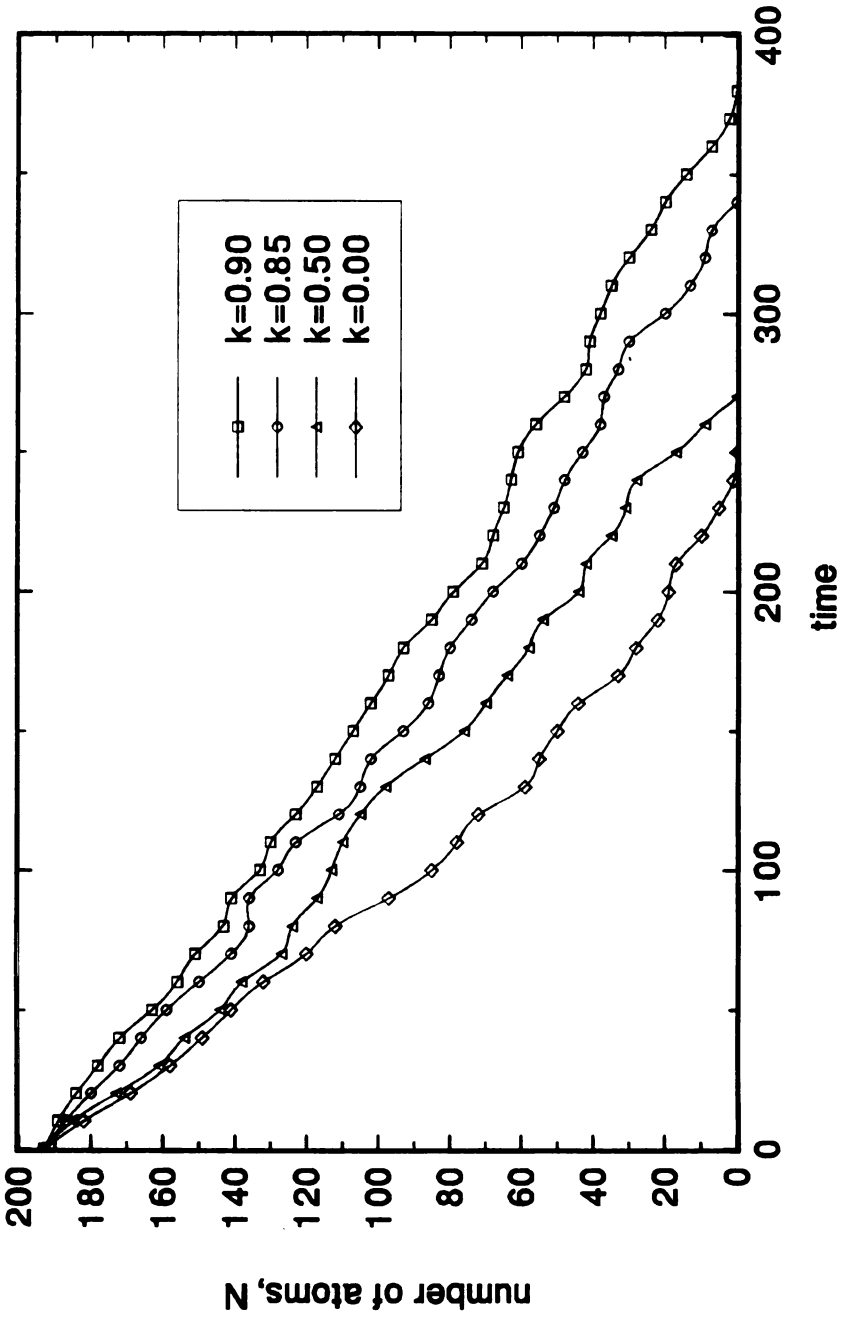

Figure 5.6 Decay of the top mesa in a three mesa system of starting sizes 200, 800, and 2500 atoms with several diferent values of k = 0, 0.5, 0.85, and 0.9.

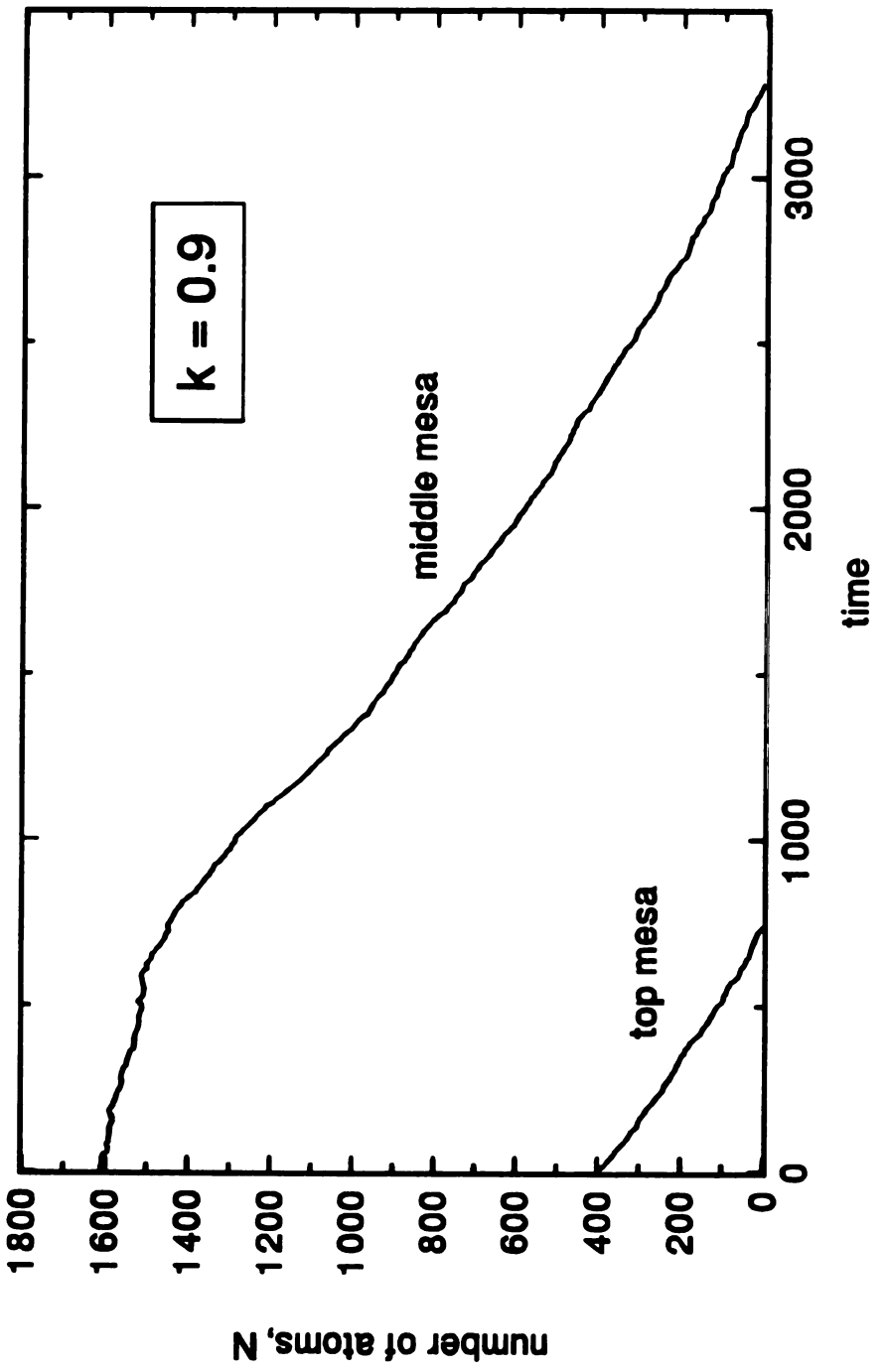

Figure 5.7 Decay of the top and middle mesas in a three mesa system of starting sizes 400, 1600, and 6400 atoms, respectively. The reflection coefficient, k = 0.9.

Au[2,3,9]. Our STM data shows the same behavior as shown in Figure 4.7 and 4.9 in Chapter 4.

In summary, we have shown, by Monte Carlo simulation, that the linear decay of monolayer islands on metal surfaces arises from a competition among the rate of emission of adatoms by kink sites, the rate of absorption by an outer ledge, and the rate of reattachment to the home mesa. Linear decay is found when the distance to the outer absorbing ledge is more than 2 or 3 times the starting radius of the mesa, and it is rather insensitive to variations in the probability of reflection from the outer ledge.

REFERENCES FOR CHAPTER 5

1 D.R. Peale and B.H. Cooper, J. Vac. Sci. Tech. **A10**, 2210 (1992).

2 David R. Peale, Ph.D. Thesis, Cornell University, 1992 (unpublished).

3 Jeeseong Hwang and M.A. Dubson (in preparation).

4 Chun-Li Liu and James B. Adams, Surf. Sci. **265**, 262 (1992)

5 Hans-Werner Fink and Gert Ehrlich, Surf. Sci. **143**, 125 (1984).

6 Claude A. Roulet, Surf. Sci. **36**, 295 (1973).

7 P. Wynblatt and N.A. Gjostein, Surf.Sci. **12**, 109 (1968); P. Wynblatt, Phys. Stat. Sol. **36**, 797 (1969).

8 C. Kitell, **Introduction to Solid State Physics**, 6th ed., John Wiley & Sons (1986)

9 B.H. Cooper, D.R. Peale, J.G. McLean, R. Phillips, and E. Chason, in **Evolution of Surface and Thin Film Microstructure: Materials Research Society Symposium Proceedings**, Vol. 280, 1992 (in press); D.R. Peale and B.H. Cooper (in preparation).

Chapter 6

STM STUDY OF THE PLASTIC DEFORMATION OF STRESSED THIN GOLD FILMS ON GLASS SUBSTRATES

6.1 ABSTRACT

With an STM, at room temperature in air, low angle grain boundaries and other dislocation arrays are observed in thermally stressed gold films evaporated on heated glass substrates. We find that these low angle grain boundaries move under an applied stress introduced either by handling the sample or by crashing an STM tip on the sample surface. From time lapse STM images, we also observe that the motion may slow to a stop, reverse direction, or show oscillatory behavior. These dynamic features usually accompany a deformation of a part of the sample. Possible explanations for this behavior are discussed along with STM observations.

6.2 INTRODUCTION

In a perfect crystal, atoms are arranged in a regular periodic pattern. However, in the real world, a crystal can contain various kinds of defects such as point defects (impurities, vacancies, etc.) and line defects (edge dislocations, screw dislocations). Since the macroscopic behavior of crystalline solids strongly depends upon the species and number of defects, the understanding of defects in a crystal has been very important. For an irreversible plastic deformation of a crystalline solid, it is well known that the

deformation is induced by the atoms sliding over one another along a well-defined slip plane instead by uniform shearing of the crystal. Many systematic studies of this behavior have revealed that the dislocations play a major role in the deformation.

Before we discuss the role of dislocations in a plastic deformation, let us first describe basic geometry of the edge and screw dislocations. Here, the definitions of those two dislocations and the Burgers vector are borrowed from Reference 1.

Figure 6.1(a) shows the atomic arrangement and bonding in a simple cubic lattice. Figure 6.1(b) and Figure 6.1(c) show an edge and screw dislocation, respectively. Suppose that all the bonds across the surface ABCD are broken and the faces of the crystal are separated so that an extra half-plane of atoms can be inserted in the slot, as illustrated in Figure 6.1(b). The faces of the slot will have been displaced by one atom spacing, but the only large disturbance of the atoms from their normal positions relative to their neighbors is close to the line DC. The deflection and distortion of the interatomic bonds decreases with increasing distance from the line. This line DC is called a **positive edge dislocation** and is represented symbolically by the symbol ⊥. A **negative edge dislocation** would be obtained by inserting the extra plane of atoms below plane ABCD and is represented by the symbol ⊤. The arrangement of atoms around a **screw dislocation** can be simulated by displacing the crystal on one side of ABCD relative to the other side in the direction AB as in Figure 6.1(c). Examination of this model shows that it can be described as a single surface helicoid, rather like a spiral staircase. The set of parallel planes initially perpendicular to DC have been transformed into a single surface, and the spiral nature is clearly demonstrated by the atom positions shown in Figure 6.1(d). DC is a screw dislocation. Looking down the dislocation line, if the helix advances one plane when a clockwise circuit is made round it, it is referred to as a **right-handed screw dislocation**, and if the reverse is true it is **left-handed**.

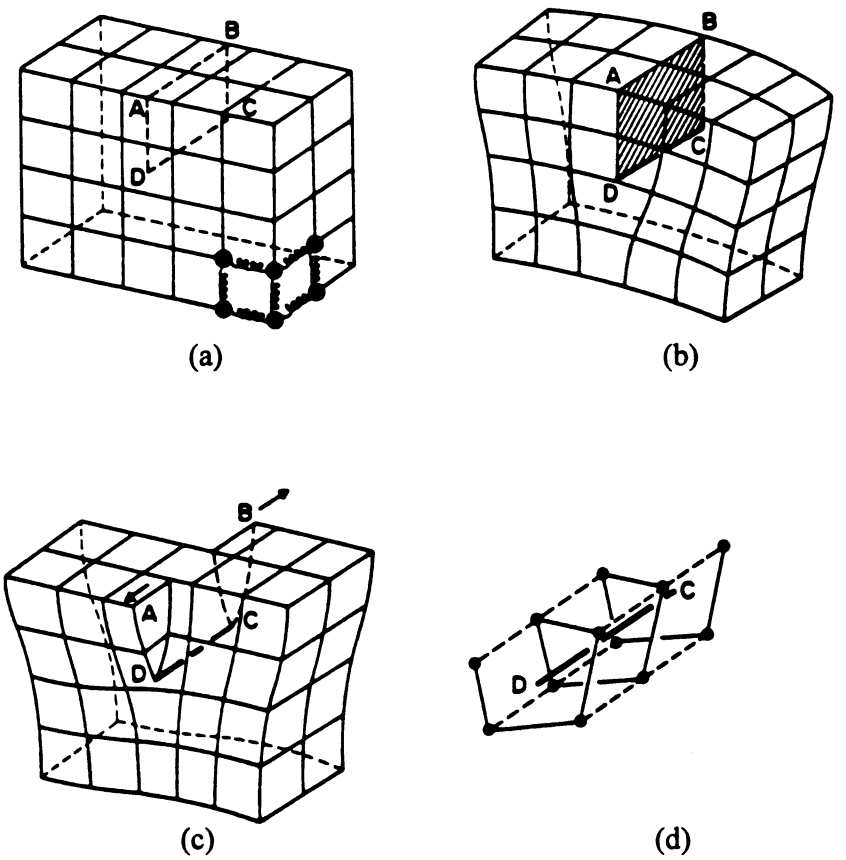

Figure 6.1 (a) A model of a simple cubic lattice. The atoms are represented by filled circles, and the bonds between atoms by springs, only a few of which are shown. (b) A positive edge dislocation DC formed by inserting an extra half-plane of atoms in ABCD. (c) A left-handed screw dislocation DC formed by displacing the faces ABCD relative to each other in direction AB. (d) A spiral of atoms adjacent to the line DC in (c). [Taken from Hull and Bacon (reference 1)]

The most useful definition of a dislocation is given in terms of the **burgers circuit**. A burgers circuit is any atom-to-atom path taken in a crystal containing dislocations so that the path forms a closed loop. Such a path is illustrated in Figure 6.2(a), i.e. MNOPQ. If the same atom-to-atom sequence is made in a dislocation-free crystal and the circuit does not close, then the first circuit, Figure 6.2(a) must enclose one or more dislocations. the vector required to complete the circuit is called the **Burgers vector**. It is essential that the circuit in the real crystal passes entirely through "good" parts of the crystal. For simplicity consider the Burgers circuit to enclose one dislocation as in Figure 6.2(a). The sequence of the circuit MNOPQ in this Figure. The enclosed failure QM is the Burgers vector and is at right angle to the dislocation line. When the Burgers circuit is drawn around a screw dislocation(Figure 6.3), again with a closed circuit in the crystal containing the dislocation, the Burgers vector QM is parallel to the dislocation line.

Usually, in a crystalline solid, there are a large number of randomly oriented single crystal grains separated by grain boundaries. When the disorientation between the adjacent grains is small, the boundary is called a low-angle grain boundary. A model that describes the low-angle grain boundary between adjoining crystallites or crystal grains as an array of edge dislocations was first proposed by Bragg[2] and Burgers[3]. The model was confirmed experimentally by Gronsky who observed low-angle grain boundaries in molybdenum crystals on an atomic scale by Transmission Electron Microscope (TEM).[4,5] Figure 6.4 shows such a low-angle grain boundary consisting of a sheet of an array of equally spaced edge dislocations lying in the vertical direction. If the spacing of the dislocations is D, then the following relation is satisfied.

$$\frac{b}{2D} = \tan\frac{\theta}{2} \tag{6.1}$$

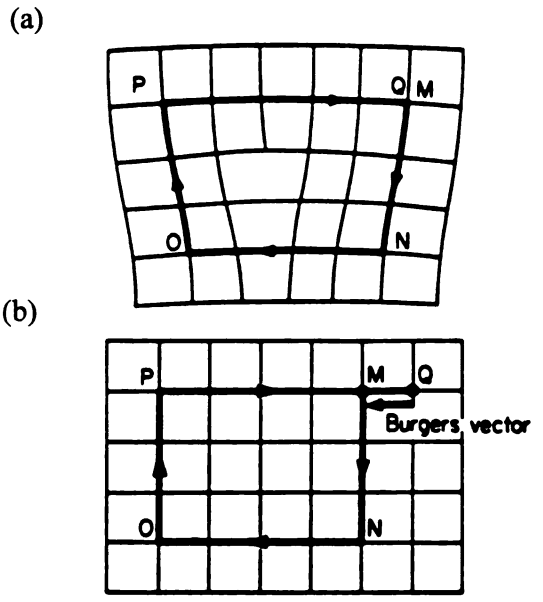

Figure 6.2 (a) Burgers circuit around an edge dislocation. (b) Burgers circuit in a perfect crystal; the closure failure is the Burgers vector. [Taken from Hull and Bacon (reference1)]

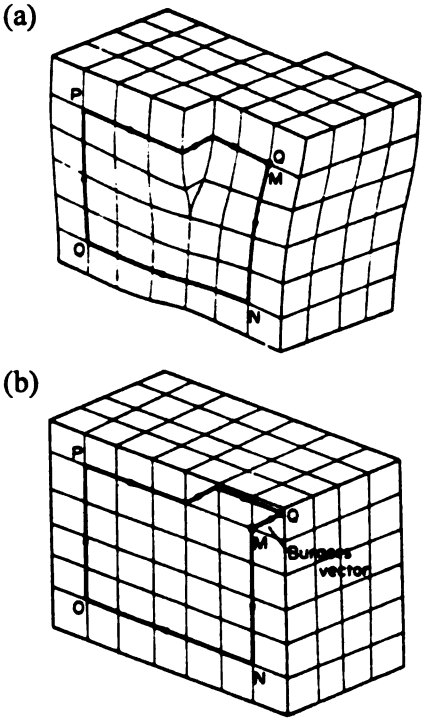

Figure 6.3 (a) Burgers circuit around a screw dislocation. (b) Burgers circuit in a prefect crystal; the closure failure is the Burgers vector. [Taken from Hull and Bacon (reference 1)]

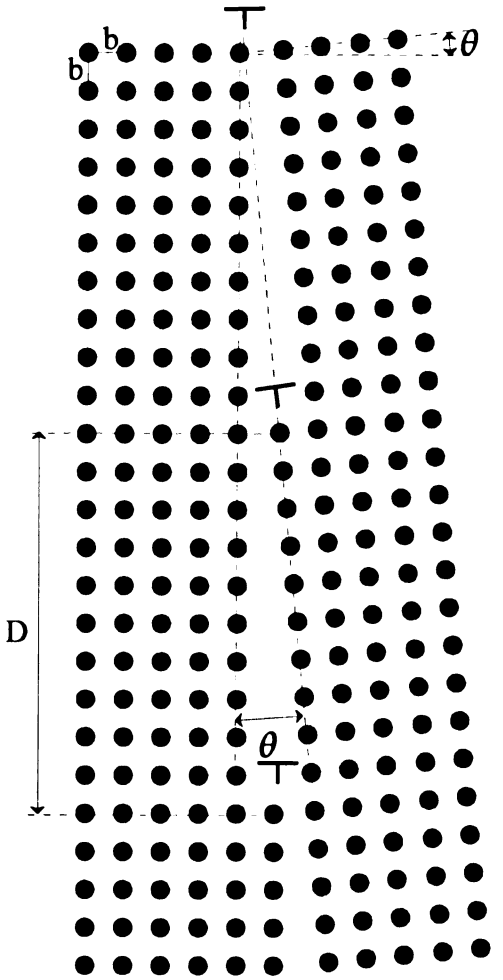

Figure 6.4 A low angle grain boundary consisting of a sheet of equally spaced dislocations.

where θ is the small tilt angle in radians, and b is the magnitude of the burgers vector. If the angle θ is small enough, then

$$D = \frac{b}{\theta} . \tag{6.2}$$

Washburn *et al.*[6] did an x-ray study to show that, in a zinc single crystal, dispersed dislocations created by bending the crystal at low temperature tend to turn into planar arrays upon annealing at high temperature. In most cases, annealing results in a network of the planes of dislocation arrays with relatively dislocation free volumes enclosed by this network. The edge of the low-angle grain boundary plane is observable on the crystal surface where the plane meets with the crystal surface. Consequently, two crystal surfaces are bounded by the edge line and form a small tilt angle. In Figure 6.4, the tilt angle is presented as θ. We call the intersection of the low-angle grain boundary plane and the crystal surface a 'boundary line'.

The idea that the low-angle grain boundary consists of arrays of dislocations is also supported by the observed motion of a dislocation array on the crystal surfaces. (If the low-angle grain boundary were just an amorphous barrier, under some shear stress, then the subgrains would slide over each other along the low-angle grain boundary and the motion of a dislocation array on the crystal surface would not be observed.)

There are two types of dislocation movements; in its slip plane (glide), and normal to the slip plane (climb). The slip plane is the plane which is perpendicular to the low-angle grain boundary plane and contains the dislocations. The glide of low-angle grain boundary under the applied stress was first predicted by Schockley[7,8]. As shown in Figure 6.5, consider a stress (τ's) applied on the surface of a crystal which contains a low-angle grain boundary. The shearing stresses moves the atoms above the slip plane

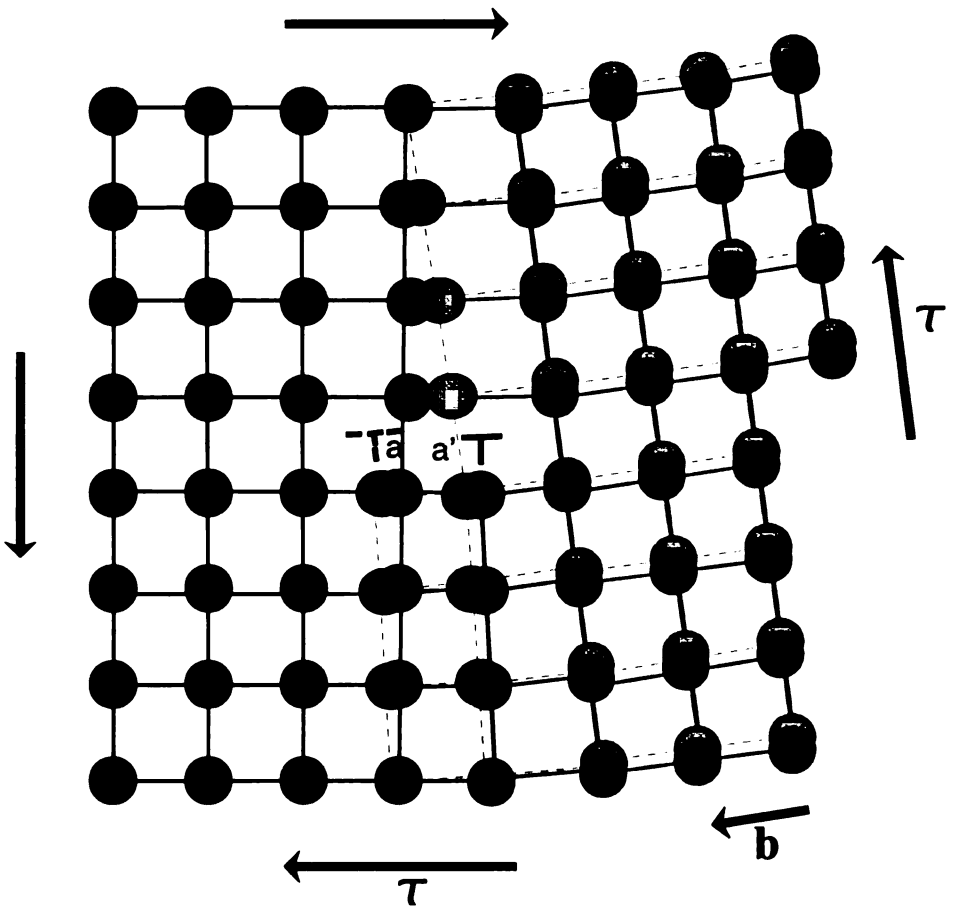

Figure 6.5 Motion of a dislocation as a glide along the slip plane (a horizontal bar of the **T** symbol). A system of shear stresses are represented as four arrows going around the crystal. As the motion of the low angle grain boundary (a vertical bar of the **T** symbol) proceeds, the atomic bond **a** is breaking and **a'** is forming. **b** is the Burgers vector.

to the right and the atoms below the slip plane to the left. The slip plane is represented as the horizontal bar of the symbol T, the low-angle grain boundary as the vertical bar. In fact, in a crystal, the glide starts at a local region and steps along (in this case to the left) instead of shearing the two pieces each other along the slip plane. Figure 6.5 shows one step of this glide process where the low-angle grain boundary plane moves to the left by one lattice constant. The black and gray dots represent the atoms before and after the motion respectively. As the motion of the low-angle grain boundary proceeds, the atomic bond a is breaking and a' is forming.

The motion of this low-angle grain boundary has been observed by J. Washburn *et al.*[4] with an optical microscope. In their experiment, a zinc bicrystal was clamped at one side and stress was applied to the un-clamped side of the crystal. Under the influence of the applied stress, they observed a 2 degree low angle low-angle grain boundary move back and forth according to the direction of the applied stress. It is worth pointing out that the motion was observed with an external stress approximately equal to the crystal's yield stress.

With a home built STM described in Chapter 2, we observed similar behavior in thin gold films on glass substrates. Most of the samples in this experiment are prepared by evaporating 40 to 200nm-thick gold films on heated glass substrates at 300C and annealed at 300C for a few hours following deposition. The samples were then allowed to cool in vacuum to room temperature. All of the STM images presented in this Chapter are taken at room temperature in air with a tunneling current of 1.0nA and a sample bias in the range of +100mV to +300mV. (The STM tip is at virtual ground.)

6.3 RESULTS AND DISCUSSION

In Chapter 3, we showed that thermal evaporation of gold on hot (about 300C) glass substrates yields growth of layers of gold which are (111) planes. We find that such films exhibit many dislocations and defects. Figure 6.6 shows a right-handed screw dislocation developed during the growth. To produce this sample, 80nm of gold was evaporated on 300C glass without annealing after the evaporation. Since this kind of screw dislocation is rarely found in annealed samples, we believe the dislocations tend to annihilate (for the dislocations with opposite signs) or turn into a more stable configuration by thermal activation during the annealing. If the dislocations are random, then they will collect to make a low-angle grain boundary plane during the annealing.[4]

Figure 6.7 displays time-lapse STM images showing a boundary line on a 80nm-thick Au film thermally evaporated on a 300C glass substrate and annealed. This sample was recleaned and imaged 5 days after the preparation. The low-angle grain boundary emerges from the crystal to form a straight boundary line on the surface. By measuring the tilt angle from the sample surface profile (see Figure 6.8), we find that the two subgrains meet with an angle of 5.1 ± 0.5 degrees which is maintained throughout the sequence of images. The images are illuminated by a point light source at infinity with an appropriate angle so that the surface of the tilted subgrain (the portion on the right side of the low-angle grain boundary) appears darker. Measuring the position of the boundary line on the sample surface, we find that the low-angle grain boundary moves to the left and finally stops. The step structure seen on the surface provides a steady reference mark relative to the motion of the low-angle grain boundary. The plot of x(t), the distance that the low-angle grain boundary moves vs. time in seconds shown in Figure 6.9 demonstrates that the motion is attenuated and finally stops.

Figure 6.6 A screw dislocation produced during the evaporation of a 80nm thick gold film onto a 300C glass substrate. A ramp with a monatomic height is going around from top to bottom. Scan size = $(100nm)^2$.

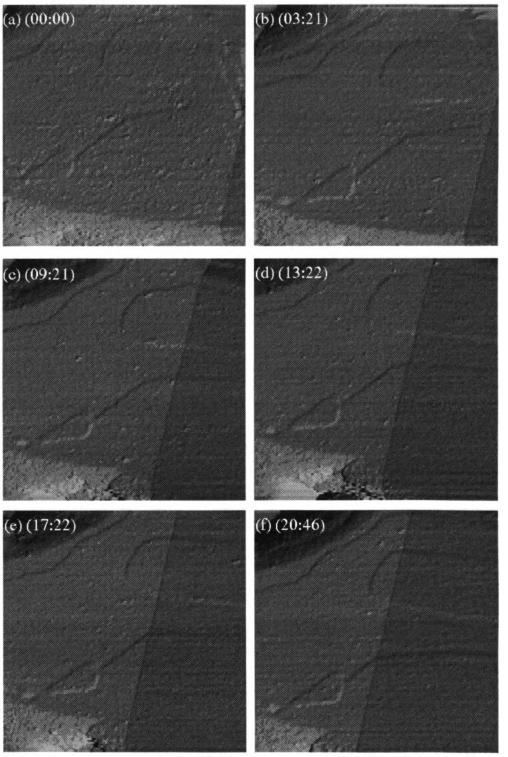

Figure 6.7 Time lapse STM images showing the attenuated motion of the low angle grain boundary. Scan size = $(180\text{nm})^2$. The time index of each image is (minute:second).

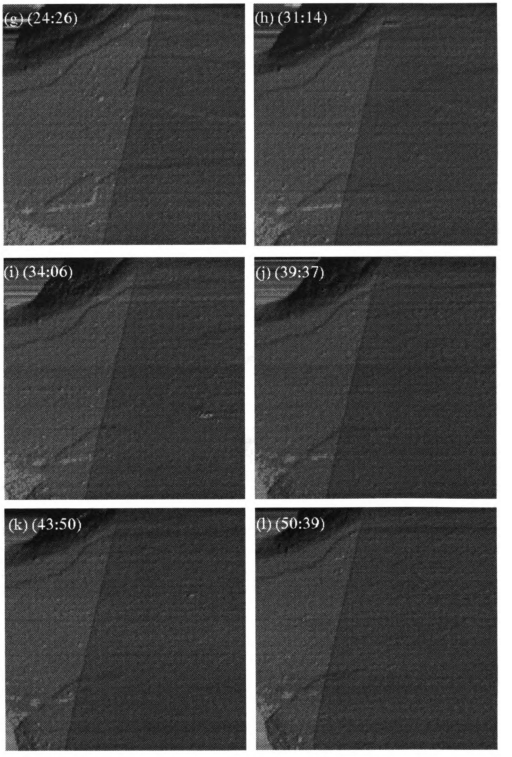

Figure 6.7 (cont'd).

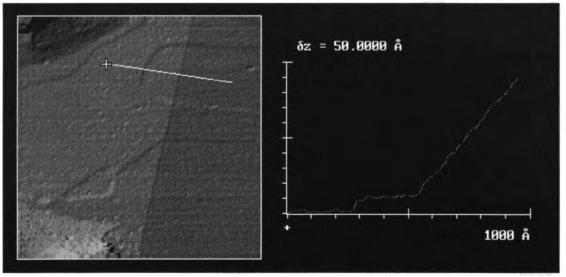

Figure 6.8 A surface profile of the image 6.7(d). The surface profile along the line on the image is displayed in the plot at the right hand side. The cross mark at one end of the line corresponds to the origin of the plot. The profile shows that the surface of the subgrain (darker gray scale) rises from the horizontal plane with an angle of about 5.1 degrees. Note that the scale of the y axis is expanded.

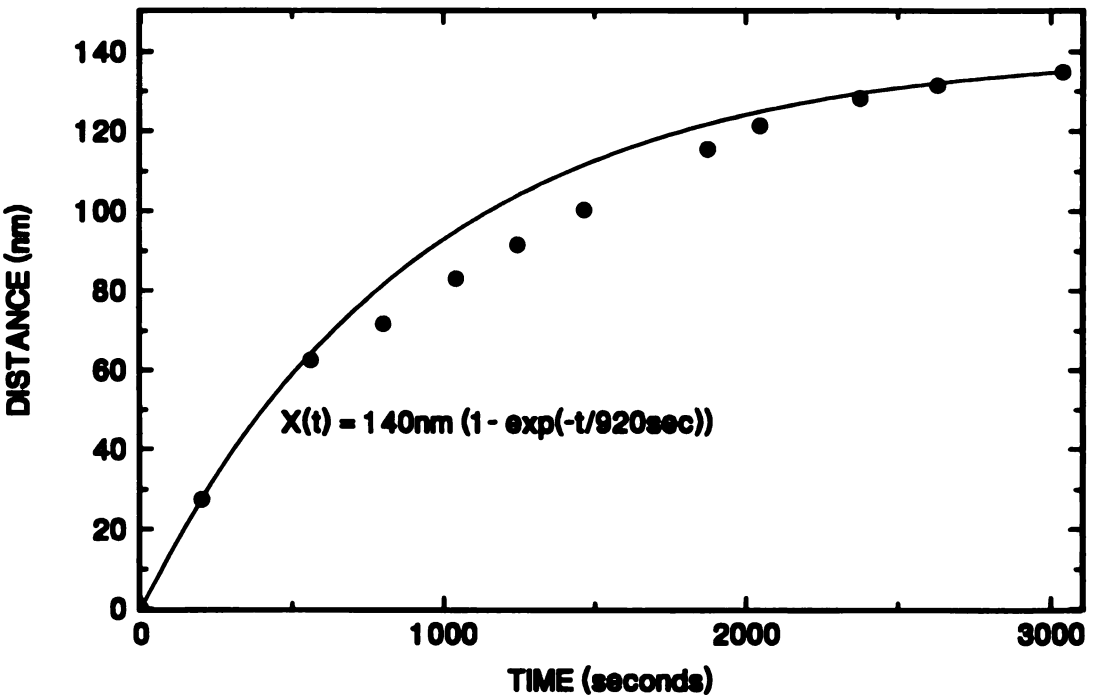

Figure 6.9 The plot of the distance that the low angle grain boundary (shown in Figure 6.7) moves vs. elapsed time. Note that the motion is attenuated and finally stops. A trial fit of x(t) is displayed along with the data.

Assuming the low-angle grain boundary is a plane, we can measure its orientation relative to the surface. If the crystal surface were perfectly flat, then the boundary line would appear as a straight line no matter how the low-angle grain boundary was oriented. The orientation of the low-angle grain boundary is not resolved in this case. With some corrugations on the surface, however, a top-down view of the boundary line will be a straight line if the low-angle grain boundary cuts the sample vertically; the boundary line will not be straight if the low-angle grain boundary plane intersects with the surface at other than 90 degrees. From Figure 6.7(a)-(d), we measure the angle of 69±5 degrees between the flat (111)Au surface and the low-angle grain boundary.

It is well known that the face centered cubic (fcc) crystal glides primarily on the close-packed {111} plane in three <110> directions in {111} plane. Figure 6.10(a) illustrates the fcc system showing one of the {111} planes and three slip directions in the plane.[9] The Figure also shows a possible low-angle grain boundary plane (plane ABD) which is another {111} plane and whose orientation corresponds to the STM observations in Figure 6.7. Figure 6.10(b) displays that the low-angle grain boundary (plane ABD) meets at an angle of 72.8 degrees with the (111) plane (plane ABC). This angle corresponds to the value obtained from the STM images within the error bound.

Once we know the orientation of the low-angle grain boundary plane, we can calculate the spacing D of the dislocations shown in Figure 6.3. From Equation 6.1, we obtain D = 29.63 ±3.22 Å, using θ=5.1±0.5 deg. and b = 2.64Å which is the length of the bond AD in Figure 6.5. This means that there is an edge dislocation about every 11 lattice constants.

If the yield shear stress is the minimum stress required to move a dislocation, a larger shear stress should be applied to assure the motion of a dislocation. The calculation of the yield shear stress was first done by Peierls and Nabarro[10]. They

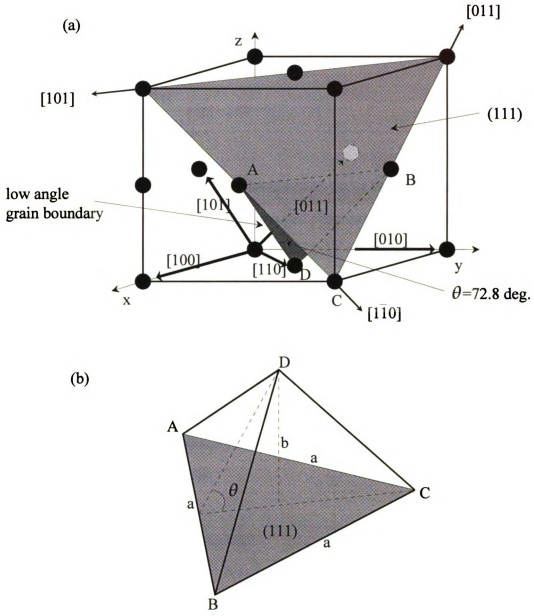

Figure 6.10 (a) The FCC system showing one of the {111} planes and three slip directions in the plane. (b) A close-up view of the (111) plane-low angle grain boundary system. The plane ABC is a (111) plane, and the plane ABD is a possible low angle grain boundary observed with an STM. The low angle grain boundary meets the (111) plane with an angle of 72.8 degrees.

calculated the change in energy due to the dislocation motion from one local equilibrium position to the next. From this, they found the stress, σ_m necessary to move a dislocation to be

$$\sigma_m = \frac{2G}{(1-\nu)} \exp[-2\pi a / b(1-\nu)] \tag{6.3}$$

where G is a shear modulus, ν is a Poisson's ratio, and a and b are the lattice constants in a low-angle grain boundary plane and in a slip plane respectively. If we put the values[9] G = 2.01×10^{10} N/m^2, ν=0.42, and $a/b \approx 1$, then we obtain $\sigma_m \cong 6.81 \times 10^{-5}$ G = 1.37×10^6 N/m^2.

Now we ask the question "What is the source of the stress to move the dislocation?" After deposition, during the cooling of the sample, thermal stresses are introduced to the gold film since the thermal expansion coefficients of gold and glass are different. By using a simple 1-D approximation, we estimate the stress, σ introduced to the gold film. During the cooldown, the strain, ϵ of the gold film due to a differential thermal expansion coefficient is

$$\epsilon = (\alpha_{Au} - \alpha_{glass})\, \Delta T \tag{6.4}$$

where α_{Au} and α_{glass} are thermal expansion coefficients of gold and of glass respectively, and ΔT is the temperature change during the cooldown. Using α_{Au} =14.2×10^{-6}, α_{glass} = 7.4×10^{-6}, and ΔT=280K, we obtain ϵ = 1.67×10^{-3} which is one minus ratio of stretched length to the original length of a gold. (i.e. during cooldown to room temperature, the gold film does not shrink as much as it would be like.) In the simple case of uniaxial tensile stress and in an elastic limit, the stress can be expressed as

$$\sigma = E\,\epsilon \tag{6.5}$$

where E is the Young's modulus of gold. (More precisely, this should be the biaxial modulus of gold in (111) plane.) Using $E=7.45\times10^{10}$ N/m^2 for gold (Reference 11), we obtain $\sigma = 1.24\times10^{8}$ N/m^2. This thermal stress is certainly large enough to move the dislocation by glide since it is two orders of magnitude greater than the yield shear stress.

One might be tempted to believe that the attenuated motion of the low-angle grain boundary is due to the relaxation of this thermal stress. However, recalling that the images were taken 5 days after the sample preparation, it is unlikely that the relaxation of the thermal stress still persists since the time scale of the attenuation of the low-angle grain boundary motion is order of 10 minutes. (See Figure 6.8.) Since the motion has such a short lifetime, it is more likely that the stress was introduced just before taking the STM images. We believe that the stress was introduced when the sample was handled[4] with tweezers as it was loaded onto the STM sample stage. Actually, the images were taken within in a few minutes after loading the sample in the STM. Once the sample is loaded in the STM sample stage, the sample is imaged in a stress-free state so that the relaxation of the stress can occur.

Another clue that a small stress can cause low-angle grain boundary motion is demonstrated in Figure 6.11. This series of images from a sample of 80nm thick gold film on a 300C glass substrate shows that STM tip crash can cause a enough stress to initiate the low-angle grain boundary motion. After obtaining an image of a flat top grain with an indented area at the center, the feedback circuit of the STM is disabled momentarily so that the thermal drift of the tip can cause the tip to crash on the sample. Several mounds shown in the images in the upper right are formed by tip hitting the

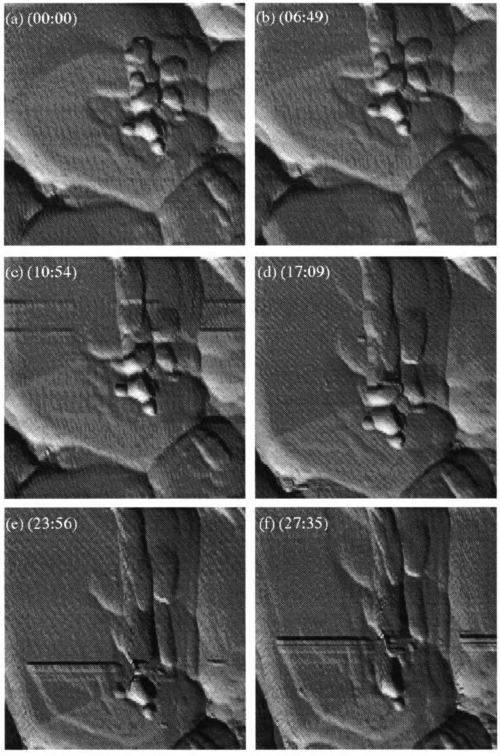

Figure 6.11 A series of STM images showing that the tip crash causes the low angle grain boundary motion. The horizontal streaky lines in (e) and (f) are noise signals. Scan area = $(200\text{nm})^2$. The time index of each images is (minute:second).

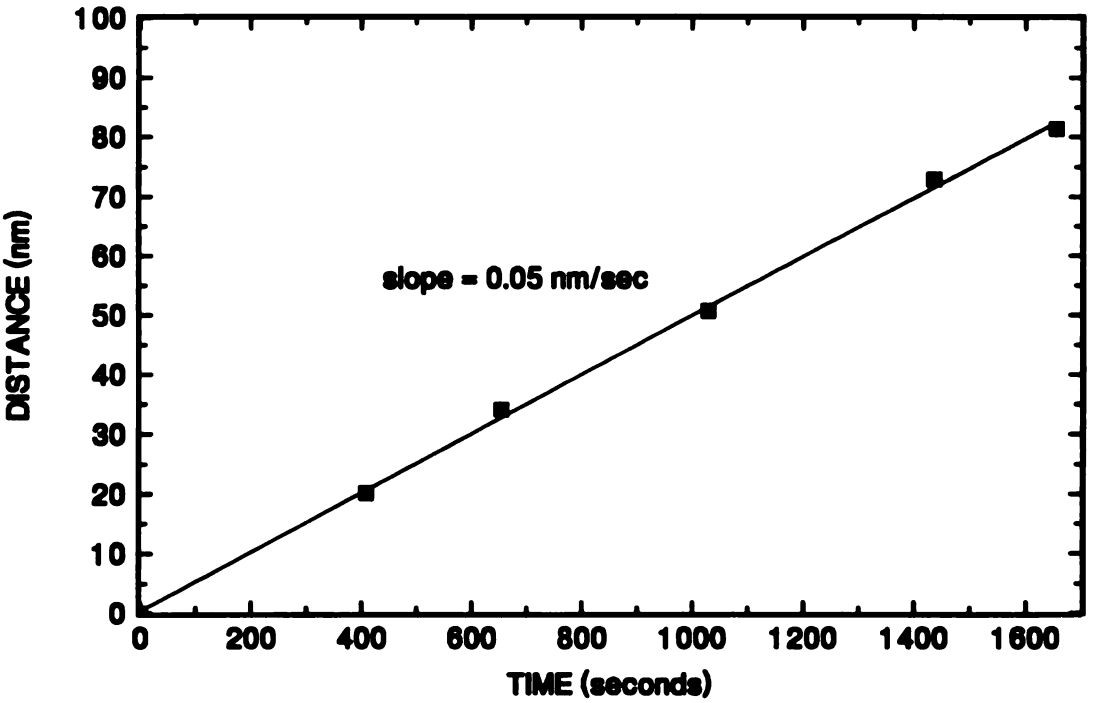

Figure 6.12 A plot of the distance that the low angle grain boundary in Figure 6.11 moves vs. time. The velocity of the motion is measured to be 0.05nm/sec.

surface. Immediately after the tip-crash, the feedback circuit is reactivated and the same area is imaged at regular intervals.

From the series of STM images, we find that a sharp buckling of the sample surface with an angle of 4.5±0.3 degrees on the upper left corner of the image starts moving toward the lower right. The angle is determined from the surface profiles of each image and found to be invariant through the measurement. In this case the surface is buckled down viewing from the top. The distance that the boundary line moves is measured and is displayed in Figure 6.12 as a function of time in seconds. From this plot, we measure the velocity of the dislocation's motion to be 0.05 nm/sec. Unfortunately, in this experiment, we did not follow the motion long enough to see any attenuation.

A striking feature in these images is that there is a noticeable plastic deformation of the features on the surface. On the surface behind the moving boundary line, the mounds elongate and flow toward the top and the surface indentation also deforms in the same direction.

Another observation of the similar activity of deformation or elongation is displayed in Figure 6.13 which are 7 sequential images selected out of total 20 images of a 40nm-thick sample taken over 100 minutes. Note the straight boundary line running across the image. A tilt correction was made before displaying the image so that the surface shown as bright gray is flat. After the tilt correction, the surface as dark gray is found to rise up with an angle of 20±2 degrees from the horizontal plane. (This angle is also preserved throughout the measurement.) Assuming the low-angle grain boundary is a flat plane, we find the tilt angle between the low-angle grain boundary and the horizontal (111) plane to be 15±2 degrees. This angle corresponds to the angle between (111) plane and (221). The simple picture that the low-angle grain boundary (or whatever) is just an edge dislocation boundary plane might be unrealistic in this high

Figure 6.13 Time lapse STM images showing that the motion of a high angle grain boundary reverses direction. Scan Size = $(300nm)^2$ for images (a) to (e), $(330nm)^2$ for the rest. The surface appearing darker rises up with an angle of about 20 degrees from the horizontal plane which is the bright surface. Note that the part of the sample where the low angle grain boundary has passed elongates and the original shape is restored as the low angle grain boundary passes again during its reverse motion. The time index of the images is (hour:minute:second).

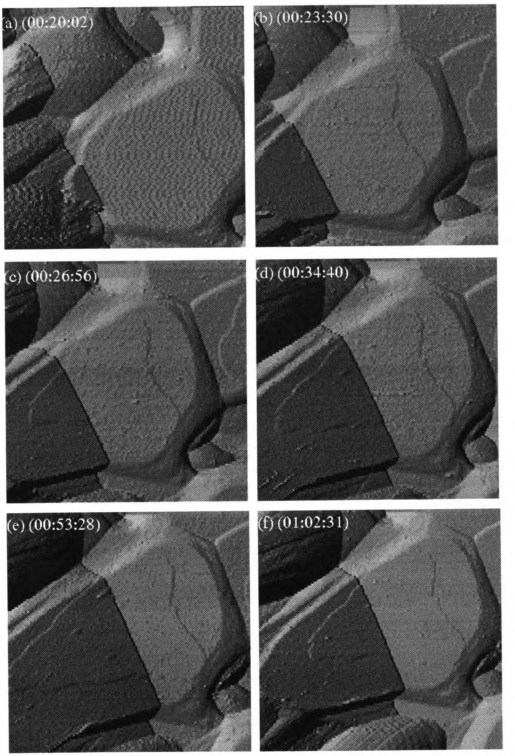

Figure 6.13

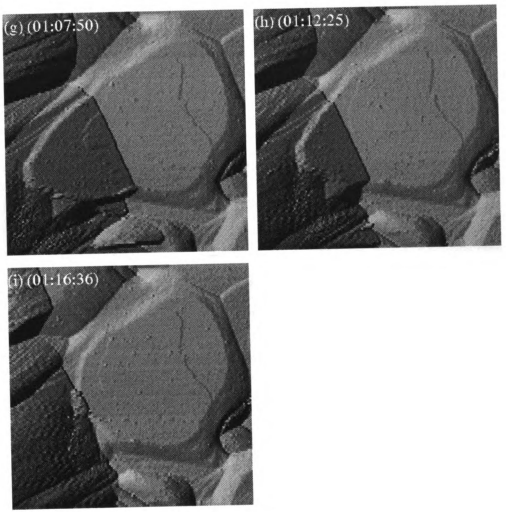

Figure 6.13 (cont'd).

(a)

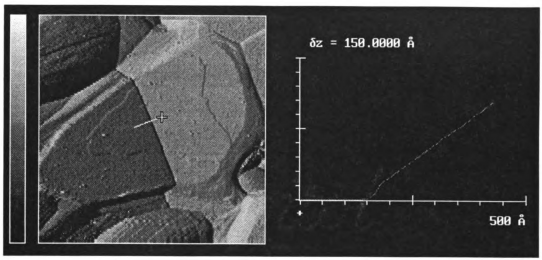

(b)

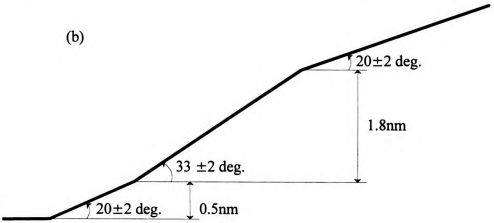

Figure 6.14 (a) A surface profile of the boundary line of the image shown in Figure 6.13 (f). (b) A close-up view of the boundary line. The surface profile along the line on the image is displayed in the plot at right hand side. The cross mark at one end of the line corresponds to the origin of the plot. A close-up view of the boundary line reveals that there are actually three boundary lines.

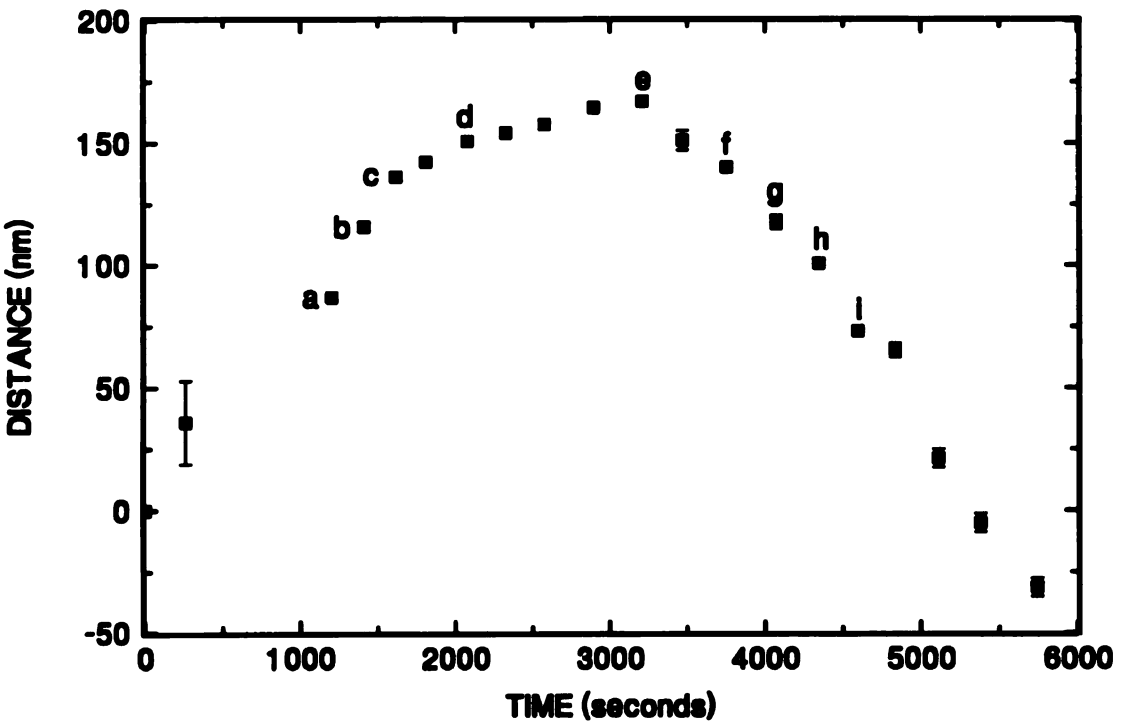

Figure 6.15 A plot of the distance that the low angle grain boundary in Figure 6.13 moves vs. time. The letters for data points correspond to the sequence of images in Figure 6.13.

angle boundary case. Actually, a close look of the surface profile near the intersection reveals that there are in fact three kinks in the intersection. (See Figure 6.14.)

Surprisingly enough, we find that the boundary line proceeds from lower left corner of the image toward upper right corner until it stops and moves backward. A heart-shaped monatomic island on top of the grain provides a nice steady reference mark relative to the motion. (See Figure 6.15 for a plot of distance vs. time.) From Figure 6.15, It is observed that the backward motion is about 3 times faster than the motion before the reverse.

A more striking feature of this observation is that, as the low-angle grain boundary proceeds, the portion of the sample where the low-angle grain boundary has passed stretches about three times toward the opposite direction of the motion. This stretch occurs not only in a horizontal plane but also in a lateral direction. The surface profile of the stretched part shows that the monatomic step becomes about three times higher after the boundary line passes. Moreover, during the backward motion of the intersection, the original unstretched shape is restored as soon as the intersection passes again.

One might raise an issue that there is a problem of mass conservation since the tilted part of the sample requires a large inflow of mass. Although a precise explanation is unavailable at present, we can think of several possible reasons for this. The atoms inside the bulk can be exposed by the climb of dislocations or an extrusion of a slip band.[12] Other possibilities are buckling of the glass substrate or peeling off the gold film from the substrate.

Sequential STM images in Figure 6.16 demonstrate another observation showing that low-angle grain boundary motion reverses (actually oscillates) its direction. Six images in this Figure are part of a sequence of 59 images of an 80nm-thick sample taken over 3 hours and 20 minutes. From the vertical view of the images, we find that two

Figure 6.16 Sequential images showing that two low angle grain boundaries show an oscillatory behavior. Six images are part of a sequence of 59 images. Scan size = $(300nm)^2$. From the top down view of the image, the distance in the plot of Figure 6.17 increases when the low angle grain boundary 1 moves to the left or when low angle grain boundary 2 moves upward. The boundary line running in the vertical (horizontal) direction is due to the low angle grain boundary 1 (2). The time index of the images is (hour: minute:second).

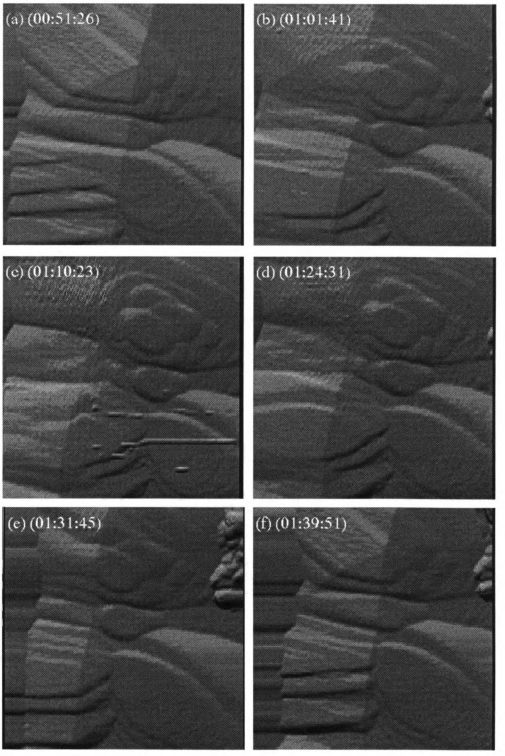

Figure 6.16

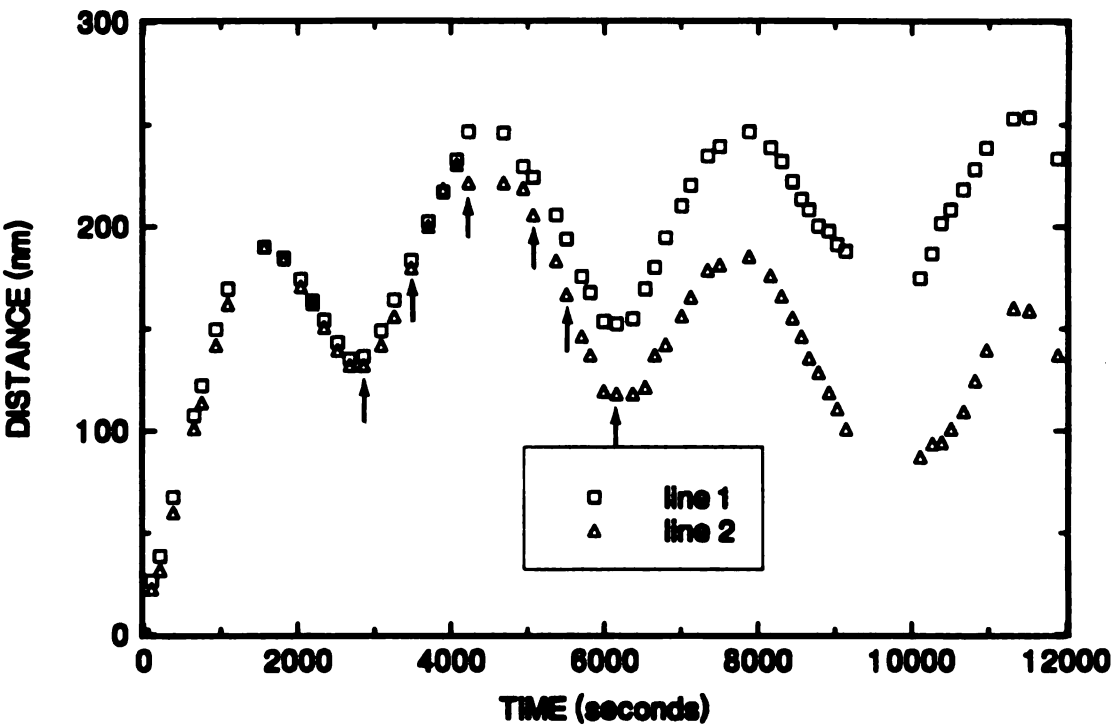

Figure 6.17 A plot of the distance that each low angle grain boundary in Figure 6.16 moves vs. time. Line1 and line2 represent the motion of boundary lines due to the motion of low angle grain boundaries 1 and 2 respectively. The data points are from the original sequence of the Figure 6.16. Six data points corresponding to images in Figure 6.15 are indicated with 6 arrows.

convex (surface is buckling upward from the top view) boundary lines are crossing each other at an angle of about 60 degrees. This implies that two sub boundaries with a same sign are crossing each other inside the bulk. When two dislocations with opposite signs meet, they tend to annihilate each other to relieve a internal stress. In this case, however, they do not annihilate since they are of the same sign.

The plot of the position of these two sub boundaries move vs. time is displayed in Figure 6.17. The boundary line due to the low-angle grain boundary running in the vertical direction (from top-down view) are named as line1 and the other is line2. The data points indicated by arrows correspond to images displayed in Figure 6.16 in sequence. In this plot, we find that the motion is oscillating with a period of about 1 hour and with an amplitude of 100nm. The observation was stopped while the motion was continuing. It is worth noting that this oscillatory behavior is not induced by the tip scanning effect since the oscillation is continuing even when we are not imaging during a coffee break. (See the break near at t=9500 seconds.)

I now present a possible explanation of the reversible motion of the low-angle grain boundary. A series of dislocations constantly emitted from a dislocation source (due to an applied stress) can be piled up against an obstacle barrier such as grain boundary so that they interact elastically with each other by reducing the spacing. Consequently, there will be an internal backward stress due to the repulsion of the dislocations. When the applied stress is eliminated, the backstress might initiate the dislocation motion backward. This explanation is nothing but speculation at present. Further experiments such as an STM observation on an atomic scale might reveal a precise mechanism.

Although the observations in this Chapter still need more rigorous explanations, we conclude this Chapter by raising following questions based on the observations.

- How are the dislocations introduced during the film growth so that they collect into a low-angle grain boundary plane during the annealing process?
- In a thin film, how does the velocity of a moving dislocation depend on the applied stress?
- What causes the abrupt change in a surface feature (the factor of 3 stretch) after a low-angle grain boundary passes?
- How can a moving dislocation stop and reverse the direction of its motion?
- What is the driving force of the oscillatory behavior of a low-angle grain boundary?
- How can we explain the motion of the high angle grain boundary showing the shape memory and the stretching behavior?

Possible answers for some of these questions have already been discussed in the text. To give a clear answer of those questions, however, we may need more experimental investigations which involve observations during the annealing, atomic scale observations of the dislocation, a stress controlled experiment, and the study of the effect of the substrates with an AFM.

REFERENCES FOR CHAPTER 6

1 D. Hull and D.J. Bacon, **Introduction to Dislocations**, 3rd. ed., Pergamon Press, 1984

2 W.L. Bragg, Proc. Physical Soc. **52**, 54 (1940)

3 J.M. Burgers, Proc. Physical Soc. **52**, 23 (1940)

4 R. Gronsky, **Images of Materials**, Oxford, 1991

5 C. Kittel, **Introduction to Solid State Physics**, 6th. ed., John Wiley & Sons, 1986

6 J. Washburn and E.R. Parker, Trans. AIME (1952); **Journal of Metals** (October 1952)

7 W. Schockley, **Cold Working of Metals**, Amer. Soc. Metals (1949)

8 W. Schockley, Trans. AIME (1952); **Journal of Metals**, (August 1952)

9 R.W.K. Honeycombe, **The plastic Deformation of Metals**, 2nd. ed., Edward Arnold, 1984

10 R. Peierls, Proc. Phys. Soc., **52**, 34 (1940); F.R.N. Nabarro, Proc. phys. Soc., **59**, 256 (1947)

11 E.A. Avallone and T. Baumeister, **Mark's Standard Handbook for Mechanical Engineers**, 9th. ed., McGraw-Hill, 1978

12 John E. Dorn, **Mechanical Behavior of Materials at Elevated Temperatures**, McGraw-Hill, 1961

Chapter 7

STM STUDIES OF SMALL METAL PARTICLES ON FLAT SUBSTRATES

7.1 ABSTRACT

A variable temperature STM is used to study discrete charging effects in small normal metal particles on substrates which are so flat that the particle shape can be clearly imaged with an STM. Samples consist of a support substrate (cleaved mica, etched Si, glass), a base electrode (Au, Ag, In, Sn, Pb, etc.), a tunneling barrier (Al_2O_3, InOx, PbOx, etc.), and finally small particles of Au. Several attempts to make a flat metal-oxide barrier substrate are presented. Our most successful recipe involves oxidized Pb on top of Au film evaporated on SiO_2. Finally, small gold particles are prepared by thermal evaporation of a discontinuous film onto the PbOx-Au-SiO_2 substrate. A home-built STM, operating in the range 4K-300K, both images the particles and performs I-V spectroscopy. I show I-V curves which exhibit a coulomb staircase at room temperature and a coulomb blockade at 83K.

7.2 INTRODUCTION

Understanding the electronic properties of small metal samples is a subject of growing importance as the microelectronics industry pushes toward smaller and smaller circuitry. As the size of a block of metal diminishes, new effects, not visible in larger samples, arise and eventually dominate the simple ohmic metallic behavior. For sizes less than roughly 1000Å, at least three small size effects must be considered: weak localization, discrete charging effects, and quantum size effects. In this small size

regime, the distinction between bulk and surface physics fades away: nearly every atom is on or near the surface.

Each of the three small size effects - weak localization, discrete charging effects, and quantum size effects - becomes apparent in distinct regimes of sample size and temperature.

Weak localization effects become apparent when the sample dimensions are smaller than the electron inelastic diffusion length (about 0.1 - 1μm at 4K). This "mesoscopic regime" has come under intense scrutiny (for a review, see reference 1) and a fairly clear picture of coherent backscattering and universal conductance fluctuations has emerged. The work here focuses on the study of particles and structures smaller still (typically 10-100Å) than this mesoscopic regime. Discrete electron charging effects appear when the coulomb charging energy exceeds the thermal energy, k_BT. This charging energy is the energy required to add an extra electron to a metal particle or, more generally, the energy to transfer an electron across a capacitive junction. The charging energy is $e^2/2C$ where C is an appropriate capacitance, a particle-substrate capacitance, for instance. The condition $e^2/2C > k_BT$ is satisfied for a 1000Å particle at $T < 10K$. In this regime, charge fluctuations via tunneling are suppressed. The charging energy is then the dominant energy scale, determining the tunneling dynamics of small particle systems and of small-area Josephson junctions.[2,3]

In very small particles, of size less than 100Å, the discreteness of the electronic energy level spectrum is expected to produce a variety of unusual effects, commonly referred to as quantum size effects (QSE). The separation in energy between adjacent energy eigenstates is roughly $\delta=E_F/N$ where E_F is the fermi energy and N is the total number of conduction electrons in the sample. When the sample is so small that $\delta > k_BT$, one expects the particle to act more like a big molecule than a metal with a quasi-continuum of states. At T=4K the condition $\delta>k_BT$ is met for particles less than 100Å

in diameter.

Most experiments to date on small particle systems have involved many-particle samples and an inevitable smearing of measured properties over the particle distribution. In contrast, the main goal of this Chapter is to investigate small size effects in single small metal particles with the variable temperature STM described in Chapter 2. The STM can both image the particles and perform electron energy-level spectroscopy, allowing investigation of a size regime (10-1000Å) as yet inaccessible to lithography while avoiding the ambiguities of ensemble averaging.

Such efforts as described here are essential to further our understanding of tunneling dynamics and transport in granular materials and other small electronic systems. This knowledge will be necessary for the design of future quantum electronic devices -- devices whose function involves movements of single electrons. Quantum devices now envisioned will rely on the field effect to detect single electronic charges, and will lead to new extremes in packing density and speed of integrated circuits. Examples already being developed are a quantum electrometer which measures current by counting the passage of electrons one-by-one, or a small particle memory element whose quantum charge state, controlled by tunneling, defines the memory.

7.3 SAMPLE PREPARATION

Searching for the Recipe to Fabricate Flat Metal-Oxide Barrier Substrates

The experimental arrangement of the small particle experiment is illustrated in Figure 7.1. Samples consist of a support substrate (cleaved mica, etched Si, glass), a base electrode (Au, Ag, In, Sn, Pb, etc.), a tunneling barrier (Al_2O_3, InOx, PbOx, etc.), and finally small particles of Au which are prepared by thermal evaporation of a

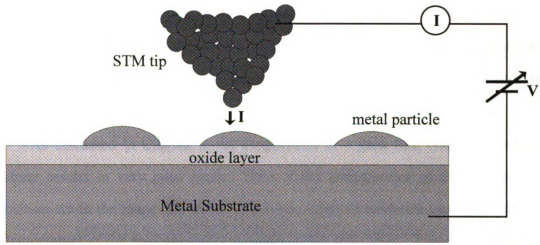

Figure 7.1 The experimental arrangement of the small particle experiment. This is a N-I-N-I-N double tunnel junction with the upper junction being the adjustable vacuum gap (between the STM tip and the small metal particle).

discontinuous film on top of the oxide layer. Fixed in space above a particular particle is the tunneling tip of an STM. We then have a N-I-N-I-N double tunnel junction with the upper junction the adjustable vacuum gap (between the STM tip and the small metal particle), the lower junction the fixed oxide barrier, and the small particle in between. We then investigate the I-V characteristics of this two-terminal structure.

To locate the STM tip above a particular particle, the substrate must be flat so that the particle shape can be clearly imaged with the STM. Several attempts were made to achieve the flat metal-oxide barrier substrates.

Our first attempt involved the fabrication of an atomically flat gold film evaporated on a hot mica substrate. After we obtain an atomically flat gold film on a mica substrate, we then evaporate a few monolayers of aluminum to be oxidized.

As discussed in Chapter 3, the evaporation of a gold film onto a heated mica substrate results in very poor quality films if the temperatures of the pre-bake and deposition are in the range 320-500C. However, films of moderate quality result when the temperature of the pre-bake and deposition is less than 280C. Figure 7.2 is an STM image of 120nm-thick gold film evaporated on 240C mica substrate. The images shows that the flat-top gold grains with an average grain size of about 100 nm are formed on the mica substrate. The freshly cleaved mica substrate was baked in vacuum for 16 hours in the temperature range 235-265C. During the evaporation the pressure remained below 2 x 10^{-6} mbar. (The base pressure was 1 x 10^{-7}.)

After the gold film has cooled to room temperature in vacuum, another 1nm of aluminum is evaporated at a rate of 0.1-0.3nm/sec. The aluminum film is then exposed to a pure oxygen gas at a pressure of about $5x10^{-2}$ mbar for a few minutes. We chose aluminum expecting it to wet gold since aluminum has the same crystal structure (fcc) and it has a similar lattice parameter as gold (Au: 4.08 Å, Al: 4.05Å). However, the SEM picture of the resulting film shows that Al does not wet the gold surface. (Figure

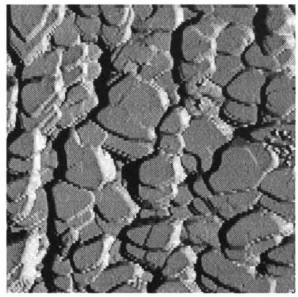

Figure 7.2 Topographic mode STM image of a 12nm thick gold film evaporated on a 240C mica. Scan size = $(750nm)^2$. Sample bias = 255mV, tunneling current = 0.3nA.

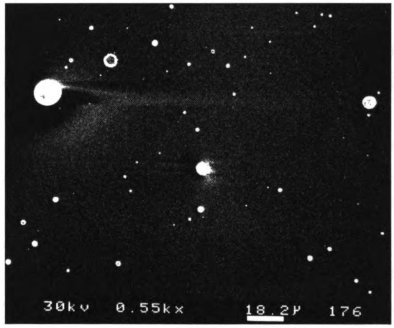

Figure 7.3 SEM photograph showing that evaporated Al does not wet the gold surface. The evaporated aluminum forms spherical droplets (bright dots in the picture) with diameter of a few tens of nanometers to a few micrometers.

7.3) We find that the evaporated aluminum forms isolated spherical droplets with diameters of a few tens of nanometers to a few microns.

Our second attempt was inspired by the morphology of indium evaporated on an oxidized Si wafer. Below a critical thickness, an indium film evaporated onto SiO_2 at room temperature produces isolated, compact islands (droplets) with flat faceted tops. The SEM photograph in Figure 7.4 illustrates such a film which consists of faceted droplets prepared by evaporating 111nm of indium at a rate of 10nm/sec. Our hope was that, after oxidizing the surface of the indium sample, the faceted surface could be used as a platform for small metal particles.

The oxide barrier must be thin enough to conduct the tunneling current of the STM. Otherwise, the isolated metal particles are not observable since they would be placed on top of insulator which does not provide a conducting path to the particles. To see the possibility of tunneling, a 450nm thick indium film (beyond the percolation limit) was evaporated on room temperature SiO_2 and oxidized by the same procedure as in the case of aluminum. We found that a very high bias (sample voltage> 3.3 volt) was required to obtain a tunneling current of 1.0 nA. Moreover, the tunneling current was suspiciously stable and did not respond to acoustic noise or mechanical vibrations. We believe that the tunneling tip was buried in the oxide layer. Consequently, we found that this recipe is not useful since the oxide layer of the indium is too thick to tunnel through.

We also tried to fabricate a flat SnOx surface by oxidizing Sn evaporated on a silicon substrate at room temperature. We found results similar to those of indium.

A commercially available silicon wafer has a native oxide layer on its surface with a thickness of about 4 nanometers. This oxide layer is usually too thick to obtain a tunneling current on a silicon substrate with an STM. The technique of hydrogen passivation has been widely used[4,5,6] to remove the surface oxide so that an STM can image a bare Si surface. Several studies show that the etching process results in not only

(a)

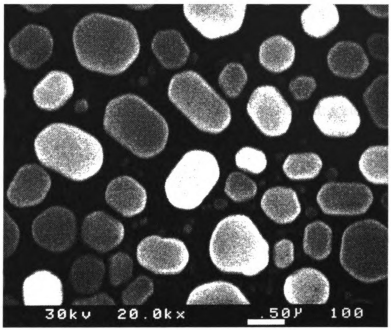

(b)

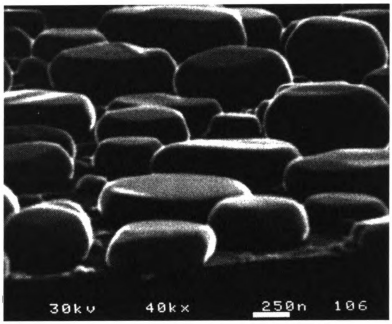

Figure 7.4 SEM photographs of well isolated compact indium islands with faceted tops. The sample is 111nm of indium evaporated on a room temperature oxidized Si substrate. (a) top view. (b) side view of the same sample. Note the difference in the scales in two photographs. (This sample and pictures were produced by G. Jeffers.)

the removal of the surface oxide but also leaves a flat surface terminated by hydrogen atoms.[7]

Our substrate was a n-doped (Arsenic) Si(111) wafer with resistivity varying from 0.01 to 0.02 Ωcm. Before the etching process, the silicon wafer was cut into 10mmx10mm squares and cleaned by an ultrasonic wash in acetone, methanol, and deionized water (DI), followed by cleaning in hot MICRO solution[8] for about 5 minutes and recleaning with DI for several minutes. The sample was then dipped into a dilute HF (36% in H_2O) for 1 minute to etch the oxide layer. These concentrations and the dipping time were confirmed to be appropriate by observing how the etched surface becomes hydrophobic. (After dipping the etched substrate into DI and we remove and observe the surface of the substrate. If DI wets the surface, then we need to immerse the substrate in the HF solution again since the oxide surface is hydrophilic.).

Higashi et al. reported that samples etched in basic buffered HF (pH=9-10) produces an ideal hydrogen-passivated Si(111) surface which is microscopically smoother than samples etched in an acidic HF solution.[7] We followed their recipe to prepare a smooth Si surface. Ammonium fluoride was added to 10% HF solution as a buffering agent (NH_4F:HF = 7:1) to increase the pH and maintain it constant at pH~5.0. Using this buffered HF solution as the starting point, the pH was raised by adding ammonium hydroxide (NH_4OH) or lowered by hydrochloric acid (HCl).

Now we give a step-by-step procedure for etching Si wafers with the buffered HF solution.[9]

The etching procedure uses three beakers. One contains the buffered HF solution and the other two contain DI for sequential rinses and are referred to as DI-1 and DI-2. Use plastic beakers and plastic tweezers since the HF is so strong that it etches glass beakers and metal tweezers.

1. Immerse the wafer into the buffered HF solution. The etch rate depends on the concentration of the solution (typically 100nm/min). To avoid overetching, initially leave the wafer in the solution for somewhat less than the estimated required time based on the oxide thickness.
2. Remove the wafer from the etching solution and immerse it in DI-1 for a few seconds, to stop the etching procedure, and then in DI-2. Observe the surface. If it is wet, then SiO_2 is still remains since the oxide is hydrophilic. However, if the SiO_2 is completely etched away, there will be only a few isolated drops since the silicon is hydrophobic.
3. If SiO_2 remains, immerse the wafer in the buffered etch again for another 30 seconds. Check the surface of the wafer as before. Continue until the oxide is removed.
4. Rinse in running DI.
5. Dry with N_2 gas.

Following the procedure above, the silicon wafer was etched in the buffered HF solution for 45 seconds. The etched samples were then stored in methanol until the STM imaging was performed. The surface profiles of STM images shown in Figure 7.5 compare the results between the etching in HF solution and in buffered HF solution. While a HF etched surface shows the surface corrugation of about 4nm (Figure 7.5(a)), a buffered HF etched sample displays the surface corrugation of 1.0-1.5nm (Figure 7.5(b)). Our result that etching in buffered HF solution results in a smoother surface is consistent with the results in reference 7.

To grow a thin oxide layer on the etched surface, the etched sample is stored in DI for 10 hours since half a monolayer equivalent of oxygen is known to be taken up by the etched surface after expose to DI for ~3 hours.[10] The sample is then transferred to a vacuum chamber to evaporate 5nm of gold at room temperature so that the evaporation produces isolated gold particles on the surface. (We expect the formation of isolated

(a)

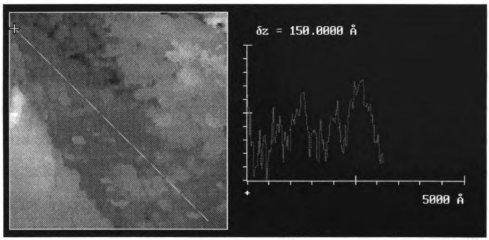

(b)

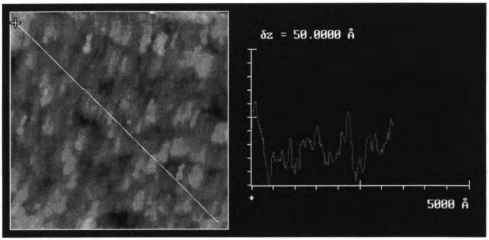

Figure 7.5 (a) STM image of the surface of Si wafer etched with a HF solution. Scan size = $(250nm)^2$, topographic mode (sample bias = -3.757V, tunneling current = 0.52nA). The surface profile along the line has a corrugation of about 4nm. (b) A STM image of the surface of an etched Si wafer with a buffered HF solution. Scan size = $(250nm)^2$, topographic mode (sample bias = -2.274V, tunneling current = 0.26nA). The surface profile along the line has a variation of about 1.0-1.5nm.

islands since metal usually does not wet an insulating surface at room temperature.) However, as displayed in Figure 7.6, the STM image shows that the gold islands are very small (~7 nm in diameter) and form a percolating network.

Our final successful recipe involves the fabrication of small gold islands on an oxidized thin lead film. An SEM photograph in Figure 7.7(a) shows 10 nm of lead evaporated on an oxidized Si wafer, producing small islands on the surface. On the other hand, the SEM photograph in Figure 7.7 (b) shows that 5nm of evaporated lead wets the gold surface produced by evaporating 30nm of gold onto a room temperature oxidized Si wafer. If lead did not wet gold, it would form spherical droplets and would show up as in the case of aluminum on gold. (See Figure 7.3.)

For the sample preparation, 30nm of gold was evaporated onto a room temperature Si wafer at a rate of 0.2nm/sec, followed by evaporating 5nm of lead at a rate of 0.1nm/sec. The pressure was maintained below $1x10^{-6}$ during the evaporations. The base pressure was $2x10^{-7}$ mbar. The sample is then exposed to a pure oxygen gas at a pressure about $5x10^{-2}$ mbar for 5 minutes. The vacuum chamber was then pumped down until it returned to the original base pressure. Finally, an additional 0.5nm of gold was evaporated at a rate of 0.1nm/sec. (The pressure was maintained below $6x10^{-7}$ mbar for this evaporation.)

An STM image of this sample is illustrated in Figure 7.8. In this Figure, gold islands with diameters of 5-7 nm and heights of 3-5nm are visible on the lead oxide surface. The existence of the oxide layer is signaled by a moderately high sample bias (1.35 V) required to obtain a tunneling current of 1.09nA. (i.e. The tunneling resistance in this case is an order of magnitude larger than the case of imaging an oxide-free metal surface.)

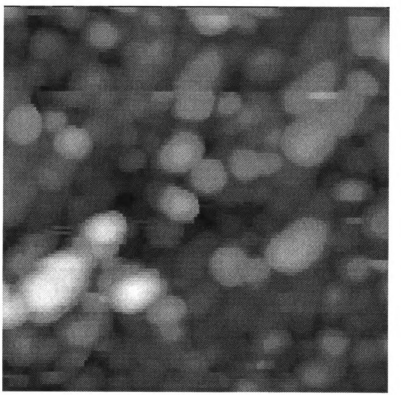

Figure 7.6 A STM image of percolating gold islands on a Si surface. This image shows that 5nm of gold evaporated on Si etched with a buffered HF solution forms percolating islands with an average diameter of 7nm and a height of 8nm. Scan size = $(104nm)^2$, topographic mode (sample bias = -1.509 V, tunneling current = 0.21nA).

(a)

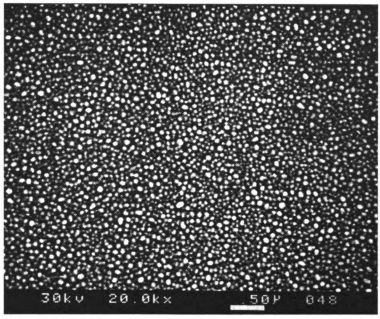

(b)

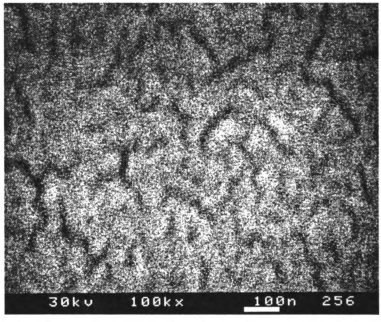

Figure 7.7 (a) A SEM photograph of isolated lead islands on SiO_2. The sample is 10nm of lead evaporated on a room temperature oxidized Si substrate. (b) A SEM photograph showing how thermally evaporated lead wets a gold surface. The sample is 5nm of lead evaporated on gold on oxidized Si wafer.

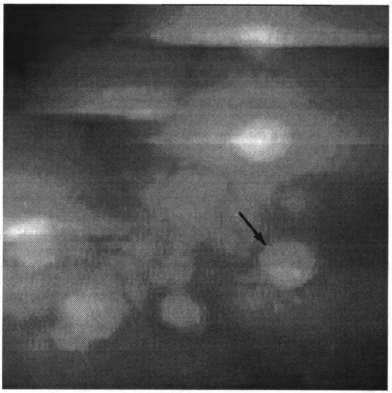

Figure 7.8 A STM image of isolated gold islands on PbOx. Scan area = $(55.5nm)^2$, topographic mode (sample bias = -1.35V, tunneling current = 1.09nA). An I-V characteristics were measured on the gold island indicated with an arrow.

7.4 RESULTS OF STM SPECTROSCOPY AND DISCUSSIONS

7.4.1 Coulomb Staircase

After obtaining the image of small metal islands, I-V characteristics were measured by the STM on an interesting island. For the I-V measurement, a special voltage waveform is applied to the sample while the feedback circuit is disabled momentarily. Figure 7.9 illustrates a schematic diagram of the waveform in the time domain. At the moment (point A) when the I-V measurement starts, the feedback circuit is disabled and the bias voltage starts ramping up from a preset minimum value (B) with small steps of size ΔV. During the ramping-up of the voltage, the tunneling current is measured after every Δt time step. (Here, the sampling frequency is given by $1/\Delta t$.) If more than one sampling is required, the ramping voltage is held at every step for a moment while a desired number of measurements is reached. (In Figure 7.9, the black dots between the points B and C represent the measuring points, and 4 samplings per voltage are shown in this case.) The measurements obtained at every step are averaged. Once the voltage reaches a preset maximum value, it starts ramping down again and the same measurements are performed. When the voltage returns to point C, the feedback circuit is reactivated and stabilizes the tip-sample distance. The same measurement repeats from point F if more than one spectrum is needed.

After obtaining the image displayed in Figure 7.8, at room temperature in air, we measured the I-V characteristics on the gold island indicated with an arrow in the Figure 7.8. The resulting I-V measurement is displayed in Figure 7.10. The measurement was performed with a sampling rate of 40kHz averaging 16 samplings per voltage step and 4 consecutive spectra. The tip-sample distance was stabilized during every time interval between the spectra for 5 msec. In this I-V measurement, two curves are presented since

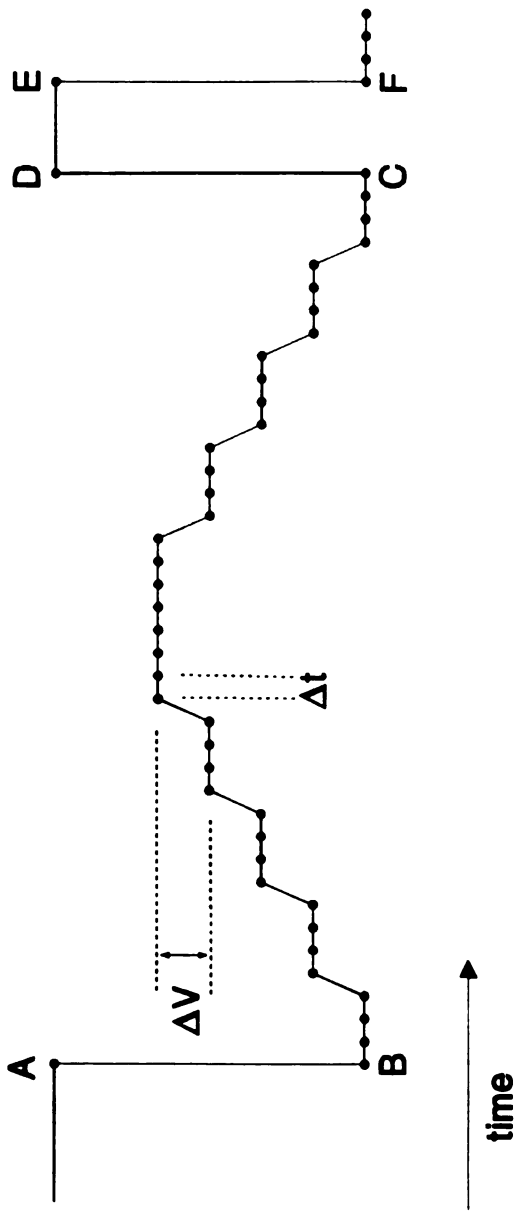

Figure 7.9 A schematic illustration of the variation in sample bias during the I-V measurement. Black dots represent data taking points except the dots at A, D, E, and F.

each case for ramping up and ramping down is plotted separately.

In the I-V spectrum in Figure 7.10, a few steps with widths of about 170mV are observed. The signal is rather noisy, probably due to a contamination of surface contamination and vibration.

The samples in this experiment can be modeled with the equivalent circuit consisting two junctions[11] in series as shown in Figure 7.11(b). C_t and R_t are the capacitance and tunneling resistance, respectively, between particle and tip. C_b and R_b are the capacitance and tunneling resistance between particle and substrate. To obtain a current through the circuit, the capacitances of the junctions must first be charged up to certain threshold voltages so that an electron can tunnel through the junctions thereafter. The threshold voltage is,[12]

$$V_t = e / 2 \max\{C_t , C_b\} = e/2C. \tag{7.1}$$

From the experimental data in Figure 7.10, we obtain V_t = 85mV which is half of the step width. From this we get $C = e/2V_t = 9.41\text{x}10^{-19}$ F.

The capacitance, C in this expression corresponds to capacitance of a small metal particle separated by an oxide barrier from the metal substrate[13] as

$$C = \kappa\epsilon_0 A/d \tag{7.2}$$

where ϵ_0 is a permittivity of free space, κ is the dielectric constant of the oxide barrier, A is the area of the particle, and d is the oxide barrier thickness. From the STM image in Figure 7.8, we can measure the dimensions of the island from which the I-V characteristic was obtained. Using $A = \pi(35\text{Å})^2$, d =20Å, and κ = 10, we obtain $C = 2.4\text{x}10^{-18}$ which is in good agreement with the measured value. It is not surprising to

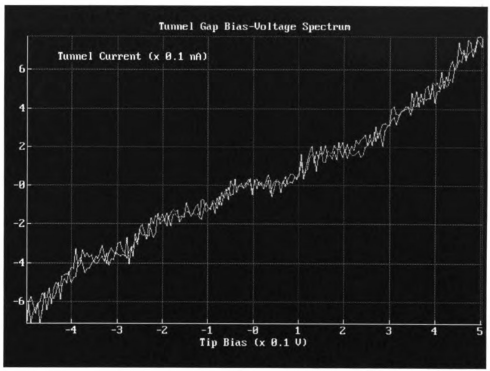

Figure 7.10 I-V spectrum of the coulomb staircase at room temperature.

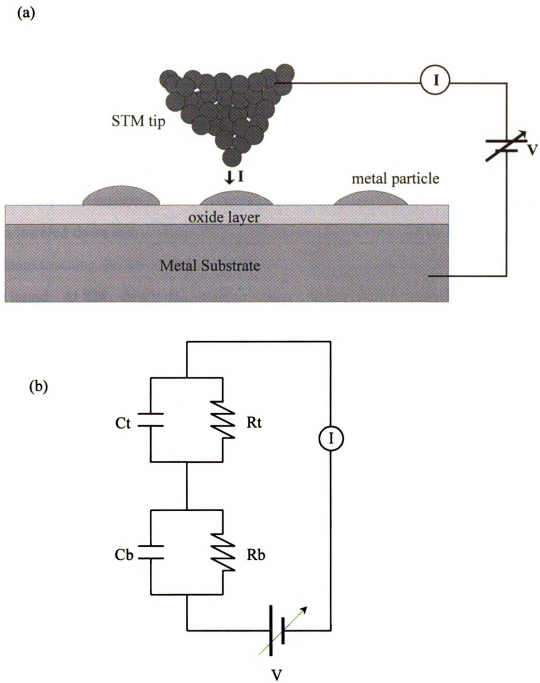

Figure 7.11 (a) The experimental arrangement of the small particle experiment. This is a N-I-N-I-N double tunnel junction with the upper junction being the adjustable vacuum gap (between the STM tip and the small metal particle). (b) The equivalent circuit of the N-I-N-I-N double junction.

see the coulomb staircase at room temperature in this system since the thermal energy corresponding to room temperature ($k_BT = 2.5x10^{-2}$ eV) is less than the fundamental macroscopic charging energy of the small particle ($e^2/2C = 3.3x10^{-2}$ eV, with C = $2.4x10^{-18}$ F for this system).

7.4.2 Coulomb Blockade

We also measured the I-V characteristics of the same sample at 83K. The STM was lowered down into a dewar filled with liquid nitrogen and placed in the cold vapor without touching the liquid surface to prevent mechanical vibration due to the boiling of the liquid. At 83K, during the attempt to image, the tip crashed into the sample surface several times and we were unable to obtain an image. Just maintaining the tip in the tunneling range, I-V measurements were performed with a sampling rate of 1kHz averaging the of 16 samples per voltage step and 4 consecutive spectra. The resulting I-V is displayed in Figure 7.12. The I-V curve in this figure shows that the curve is quadratic in V at low voltages. At high voltages, the curve tends to converge to an asymptotic line which is displaced from the origin by $\Delta V = 60.5$ mV.

This behavior has already been observed by Fulton and Dolan[13,14] and explained by Averin and Likharev[15] who model the system as a current biased single electron tunnel junction. Adopting this model, the displacement in the asymptotic line can be considered as a result of coulomb blockade due to a charging of the capacitance junction. The capacitance of the junction is estimated from $C = e/\Delta V = 2.6 \times 10^{-18}$ F. Note that the charging energy of this capacitance junction, $e^2/2C = 3.1x10^{-2}$ eV is larger than the thermal energy , $k_BT = 7.2x10^{-3}$ eV at T=83K so that the condition $e^2/2C > k_BT$ is satisfied.

For a signal small current -biased tunnel junction, the analytical solution of I(V)

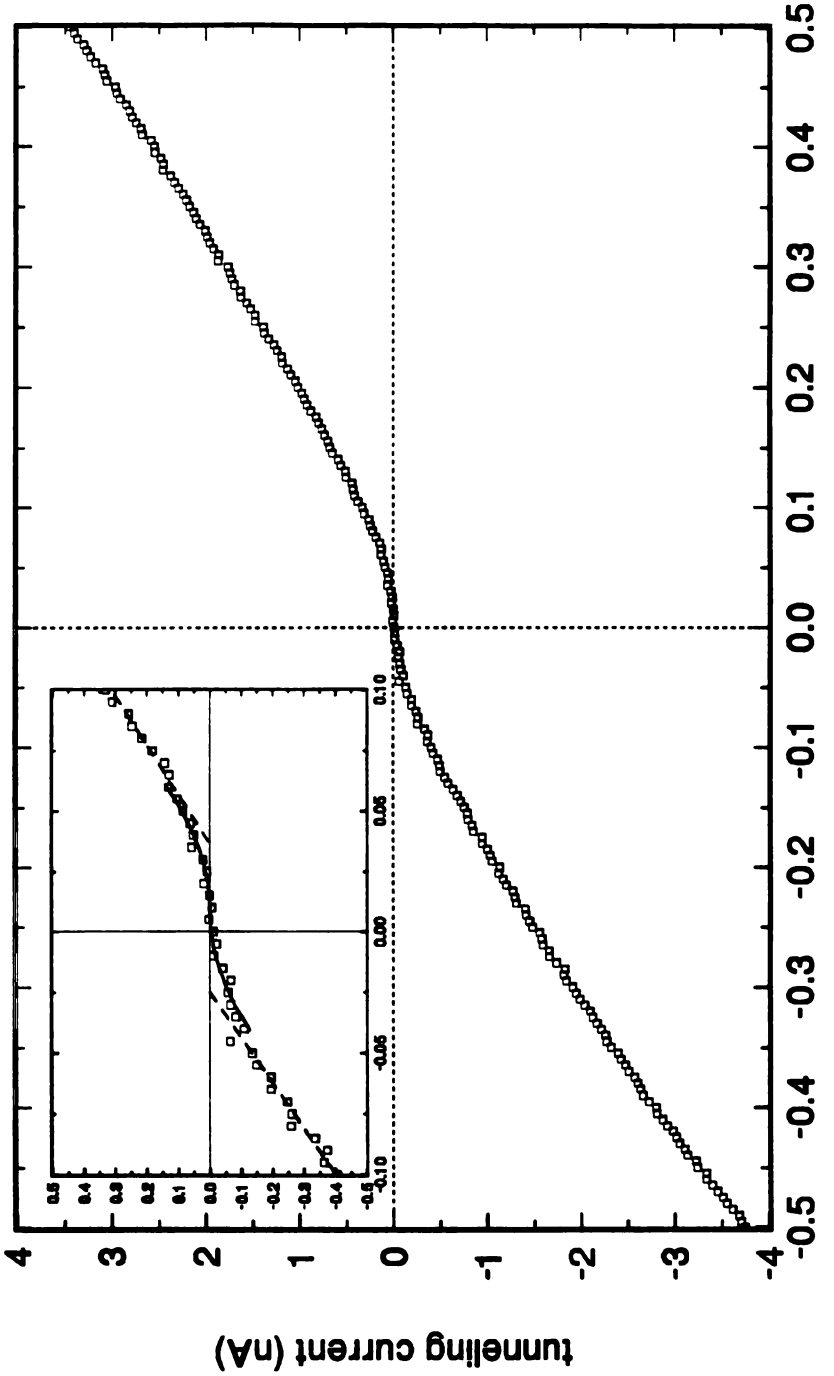

Figure 7.12 I-V spectrum of the coulomb blockade at T = 83K. The inset displays the close-up view of the plot at low voltages. In the inset plot, the dotted straight line represent the asymptote to which the data converges and the solid line represents the predicted I(V) according to the Equation (7.3).

is available at small voltages as[15]

$$I(V) = (2C/\pi R_t e)V^2 \tag{7.3}$$

where C is the capacitance of the junction and R_t is the tunneling resistance. From the experimental I-V plot in Figure 7.12, $R_t = 2.0 \times 10^8\ \Omega$ is obtained by measuring the slope of the asymptotic line to which the I-V curve converges at high voltages. (See dotted lines shown in the inset of the figure.) Using our values of C and R_t, equation (7.3) yields the predicted I(V) as $I(V) = 52.5\ V^2$ in nanoamperes.. The inset of the I-V plot in Figure 7.12 displays this predicted I(V) fit as a solid line at low voltages and shows good correspondence to the data.

However, this picture of single capacitance junction seems problematic since the real circuit is voltage biased and the stray capacitances due to the leads to the junction are typically much larger than the junction capacitance. Why then is the charging energy effect not destroyed by the stray capacitance? One proposed answer is that the stray capacitance is effectively decoupled from the system if the impedance of the leads is larger than the quantum of resistance, $R_H = h/e^2 = 4.1\ k\Omega$.[16,17] This condition is satisfied in the case that the STM tip forms a point contact junction with a sample surface.

On the other hand, Wilkins *et al.*[18] found that any metal oxide involved in the junction region can have a dominant effect on the observed tunneling characteristics. They observed that a double junction system in series which has a single metallic impurity embedded in the oxide layer sometimes imitate a single junction coulomb blockade. Unfortunately, we cannot say which model is compatible with our system since we do not have the information on the state of the sample and the STM tip location.

7.4.3 Other I-V measurements

Figure 7.13 displays a STM I-V spectrum taken over a gold sample at 82K in cold nitrogen vapor. The gold sample is 25nm thick film evaporated onto 77K glass substrate. This I-V curves shows a typical behavior in a normal metal-insulator-normal metal (NIN) tunneling junction. At low voltages the curve shows a linear ohmic behavior. As the voltage becomes comparable to the work function voltage, the I-V becomes non-linear. The I-V was measured at a sampling frequency of 40kHz and averaged over 16 samplings and 8 spectra. Pt-Rh (10%) wire was used as the STM tip.

Figure 7.14 is an I-V curve of the buffered HF etched Si sample taken at T = 82K with a sampling rate of 40kHz. The signal was averaged over 16 samplings. The sample is a **n-type** Arsenic doped Si wafer with a resistivity of 0.010-0.020 Ωcm. The diodelike curve shows characteristic of the normal metal-insulator-semiconductor (NIS) tunneling junction[19] and illustrates the expected dependence of the doping.

While experiments described in this chapter were being performed, we discovered a reliable technique to fabricate atomically flat gold films on glass substrates as described in Chapter 3. The fabrication of small metal particle samples using this technique to make large flat platform substrates is very promising for future experiments.

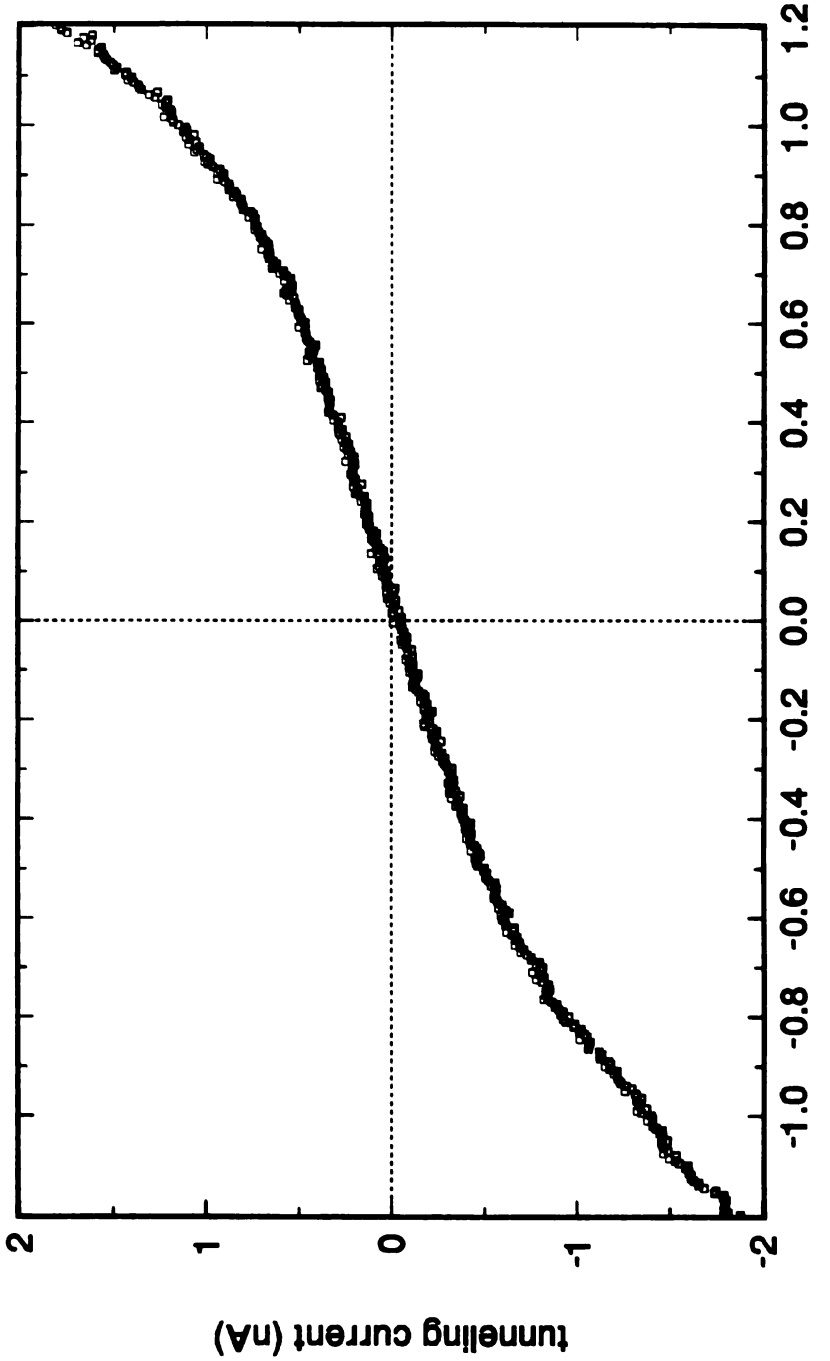

Figure 7.13 A STM I-V spectrum of a NIN tunnel junction. The spectrum was measured over a gold sample at T = 82K.

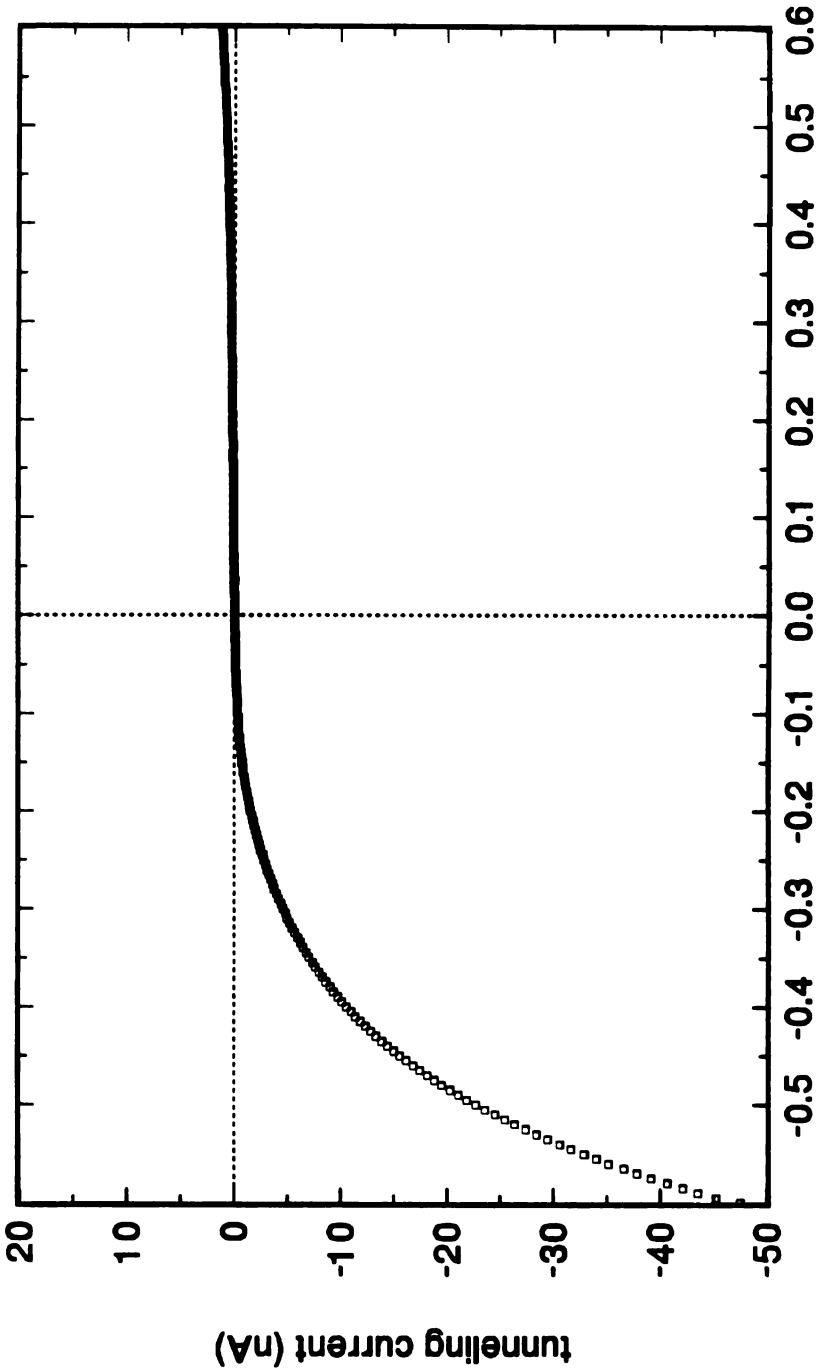

Figure 7.14 A STM I-V spectrum of a NIS tunnel junction. The spectrum was measured over a Si surface etched with a buffered HF solution.

REFERENCES FOR CHAPTER 7

1 S. Washburn and R.A. Webb, Adv. Phys. **35**, 375 (1986)

2 B. Abeles, P. Sheng, M.D. Coutts, and Y. Arie, Adv. Phys. **24**, 407 (1975)

3 M. Iansiti, A.T. Johnson, W.F. Smith, H. Rogalla, C.J. Lobb, and M. Thinkam, Phys. Rev. Lett. **59**, 489 (1987)

4 W. Kern, Semicond. Int. **April**, 94 (1984)

5 F.J. Grunthaner and P.J. Grunthaner, Mater. Sci. Rep. **1**, 69 (1986)

6 M. Grundner and H. Jacob, Appl. Phys. **A 39**, 73 (1986)

7 G.S. Higashi, Y.J. Chabal, G.W. Trucks, and Krishnan Raghavachari, Appl. Phys. Lett. **56**, 7 (1990)

8 MICRO solution is supplied by the Micro International Products Co., P.O. Box 70 Burlington, NJ 08016 (Ph: (609) 386-8770). The supplier claims that the solution removes grease residue on the surface and dissolves oxide layers of various metal surfaces.

9 D.K. Reinhard, **Introduction to Integrated Circuit Engineering**, Houghton Mifflin, 1987

10 M. Grundner, D. Graf, P.O. Hahn, and A. Schnegg, Solid State Technology, **February**, 1991.

11 The analytic solution for the I-V characteristics of this circuit is presented in M. Amman, R. Wilkins, E. Ben-Jacob, P.D. Maker, and R.C. Jaklevic, Phys. Rev. **B 43**, 1146 (1991)

12 P.J.M. van Bentam, R.T.M. Smokers, and H. van Kempen, Phys. Rev. Lett. **60**, 2543 (1988)

13 T.A. Fulton and G.J. Dola, Phys. Rev. Lett. **59**, 109 (1987)

14 P.J.M. van Bentum, H. van Kempen, L.E.C. van de Leemput, and A.A. Teunissen, Phys. Rev. Lett. **60**, 369 (1988)

15 D.V. Averin and K.K. Likharev, J. Low Temp. Phys. **62**, 345 (1986)

16 K.K. Likharev, IBM J. Res. Develop. **32**, 144 (1988)

17 S.M. Girvin, L.I. Glazman, M. Jonson, D.R. Penn, and M.D. Stiles, Phys. Rev. Lett. **64**, 3183 (1990)

18 R. Wilkins, M. Amman, E. Ben-Jacob, and R.R. Jaklevic, Phys. Rev. **B 42**, 8698 (1990)

19 S.M. Sze, **Physics of Semiconductor Devices**, 2nd. ed., John Wiley & Sons (1981)

Chapter 8

OTHER OBSERVATIONS AND FUTURE EXPERIMENTS

8.1 A sample cleaning technique at low temperature

As discussed in Chapter 2, the quality of images taken at low temperatures depends on the cleanliness of the sample surface. The surface of gold acquires one or more monolayers of water and hydrocarbon contamination after several minutes exposure to air. When an air contaminated sample is cooled to below about 240K the STM images becomes noisy.

To circumvent this problem, a high or ultra high vacuum system for the STM is under construction. The scheme is to transfer samples from the evaporator to the STM in air. The STM vacuum system is then pumped down to 10^{-7} torr at room temperature and sealed. When cooled to low temperature, residual gases condense on the inside walls of the vacuum system so that cryopumping produces a high vacuum (less than 10^{-13} torr at liquid helium temperature).

After the system is cryopumped, a heater wire wrapped around the STM sample stage briefly heats the sample to higher temperature, driving off surface contamination which condenses on the cold surrounding surfaces.

Under these circumstances, G-10 (glass fiber reinforced epoxy) is not an appropriate material for a sample stage since it outgases in the vacuum and can not survive high temperature. There is a good substitute called 'lavite' (an aluminum silicate ceramic). Lavite is a soft, machinable ceramic that we can easily use to make the STM sample stage. After machining, it is fired at high temperature so that it hardens. To fire

lavite, we first bake it at 200F for 1 hour. Then the temperature is increased by steps of 200F degrees every hour to maximum temperature of 2000F. (For a thick block, an extra bake for one more hour at 1100F is needed.) When the temperature reaches 2000F, hold it at that temperature for 1 hour for each 0.25 inches of thickness. This firing recipe is from the MacMaster-Carr catalog.

8.2 STM observations of graphite surfaces radiated by high energy charged nuclei

In early experiments, point defects or dislocations caused by neutron radiation were observed by conventional methods such as the etchpit techniques and diffraction electron microscopy.[1,2] The dynamic behavior of defects in radiation damaged samples can also be monitored by several indirect measurements which include the change of electrical resistance during the annealing of the defects or the change in mechanical properties of the crystal under applied stresses.

Highly oriented pyrolytic graphite (HOPG) is a material which easily yields an atomic resolution image with a STM in air. Its layered structure is also of great use since we can easily expose the internal structure by peeling off the outermost layers without damaging the bulk structure.

To observe the radiation damage in a HOPG sample, the HOPG with a thickness of 1.28 mm is cut into 10mmx10mm size and exposed to an 84Kr (with a charge of +17) beam for 52 min using the K1200 machine at the National Superconducting Cyclotron Laboratory (NSCL). The total number of charged Kr nucleons, the beam energy, and the beam intensity were measured to be 2.2×10^{13}, 35MeV/nucleon, and 17nA respectively. The beam energy was chosen so that the Kr ion stopped in the sample. The STM images were taken over the central region of the surface where the beam was incident. The

beam diameter was approximately 2mm. Before imaging the sample with the STM, several layers of irradiated side HOPG were peeled off 20 times with a piece of scotch tape to expose the fresh surface in the bulk and to reduce the radioactivity of the sample by removing those layers exposed to high energy Kr beam. Typically 1-10 microns are lost every time the surface is peeled.

STM images were made at several spots on the resulting graphite surface on both sides of the sample. Most of the images showed a perfect undamaged hcp lattice. However, one spot on the sample exhibited a strange triangle pattern shown in Figure 8.1. The regular triangular pits with a depth of 1nm and a side of 40-80 nm are clearly visible in the figure. Note that the density of the pattern is inhomogeneous. A more interesting feature in this sample is that the triangular pits disappear after peeling off several more layers of HOPG.

It is possible that the Kr-damaged layer of the sample was completely removed during the peeling procedure. Further STM measurements on irradiated graphite are currently underway.

(a)

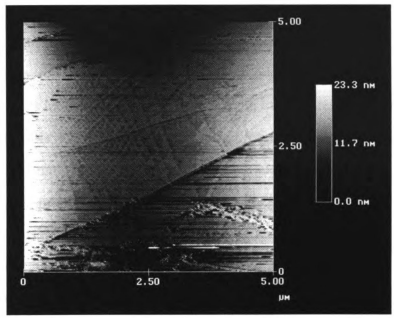

(b)

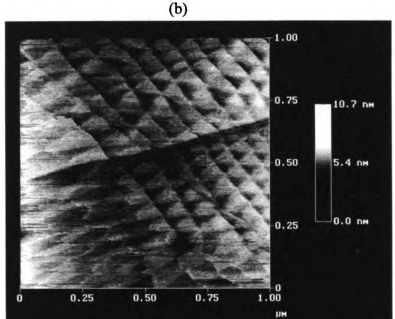

Figure 8.1 (a) A STM image of HOPG bombarded with high energy ionized Kr nucleons. (b) A close-up view of the regular triangular pits. The images were obtained with a topographic mode (sample bias = 227mV, tunneling current = 1.3nA). Images were obtained with a NanoscopeIII STM. The sample was prepared by Michael Thoennessen, at the National Superconducting Cyclotron Laboratory, Michigan State University.

8.3 High resolution AFM images of a submicron Au wire

Submicron size metal wires fabricated by photolithography or electron beam lithography have many applications. Understanding failure mechanisms involving electromigration or local Joule heating in these small metal wires are of great importance in designing reliable VLSI circuits with a long lifetime. Direct imaging of defects or grain boundary motion along with electrical measurements may provide this understanding. Using the STM for this application is problematic since the bias voltage can have an undesirable effect on measurements of interest. Another technical problem arises from the fact that locating the STM tip over the sample is very hard since the small wire is fabricated on an insulating surface.

An AFM image displayed in Figure 8.2 shows a submicron gold wire with a width of 0.3 micrometer and a height of 80nm. Note that the gold grains are clearly visible on top of the wire. These grains are a few tens of nanometers in width and about 7-8 nanometers in height.

To make an electrical measurement on a submicron wire, we have to attach thick electrical leads to make good electrical contact. A very useful lithographic technique called the triple layer method can alleviate this problem.

Figure 8.3(a) displays an AFM image of a thin wire and thick leads. The thin film wire was evaporated after the leads were fabricated by the triple layer method (sample made by D. W. Hoadley). The bright, thick features in the image are 120nm thick gold leads fabricated by the triple layer method and the thin film sample with a thickness of 50nm is visible between the leads. A close-up view of one of the thick leads, displayed in Figure 8.3(b), shows that the lead has a tapered edge with an angle of about 9 degrees to the horizontal plane.

(a)

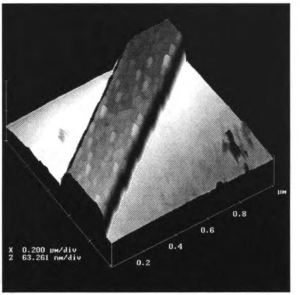

(b)

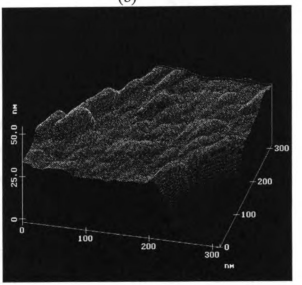

Figure 8.2 (a) An AFM image of a submicron gold wire fabricated by electron beam lithography. (b) A close-up view of top of the wire clearly showing gold grains. The image was taken with a NanoscopeIII AFM. The sample was made by Qifu Zhu.

(a)

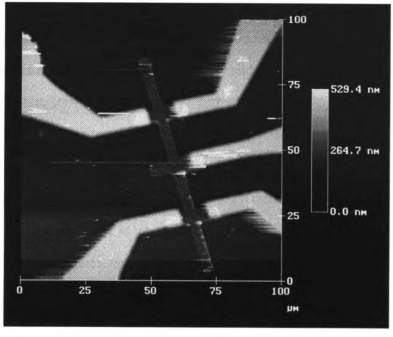

(b)

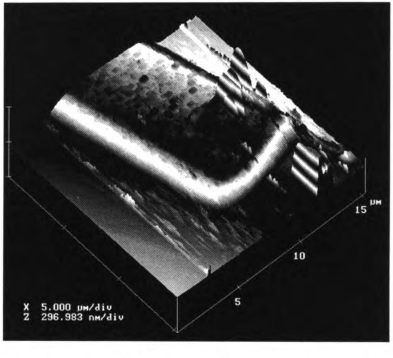

Figure 8.3 (a) An AFM image of a thin gold film and thick gold leads which was fabricated by the triple layer method. (b) A close-up view of the thick lead with tapered edge. Note the visibility of the grains on top of the lead. The sample was prepared by David William Hoadley.

8.3 STM observations of recrystallized gold on W boat.

During thin film fabrication by thermal evaporation, a piece of pure gold wire is melted in a tungsten boat by resistive heating and evaporated onto a substrate. We briefly heat the tungsten boat in order to turn the solid gold into a liquid form and stopped applying current through the boat. The tungsten boat then was cooled down to room temperature in the vacuum chamber so that the gold recrystallizes. After several minutes, the recrystallized gold on the boat was transferred in air to the STM and imaged. Figure 8.4 shows a STM image of the gold surface. This image shows the clear hexagonal faceting which is characteristic of the (111) closed packed plane of FCC metals.[3,4] This result is similar to that obtained by evaporating gold on heated mica at 500C (reference 4).

Figure 8.5 is another STM image taken at a different spot on the gold surface. The image shows evidence of the uniform shear motions in the crystal. (In the figure, the slip planes are bright surfaces parallel to the horizontal plane of the staircase structure.) In Chapter 6 we found that, under a reasonably small stress, the slip motion in a crystal is induced by local rearrangements of atoms along the slip plane instead of uniform shearing of the crystal as observed in this case.

As in Chapter 6, we can estimate the thermal strain introduced in the gold film. During the cooldown, the strain, ϵ of the gold film due to a differential thermal expansion coefficient is

$$\epsilon = (\alpha_{Au} - \alpha_{W})\,\Delta T$$

where α_{Au} and α_{W} are the thermal expansion coefficients of gold and of tungsten, respectively, and ΔT is the temperature change during the cooldown. Using α_{Au}

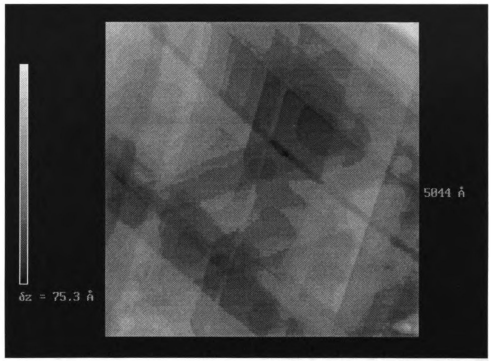

Figure 8.4 A STM image of recrystallized gold surface on a W boat. The discreteness in the grayscale in the image represents each (111)Au planes separated by a monatomic step. The image was obtained with our STM in a topographic mode (sample bias = 240mV, tunneling current = 1.3 nA).

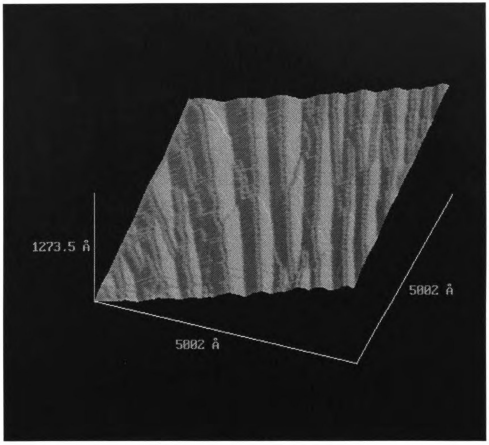

Figure 8.5 A STM image of recrystallized gold surface on W boat. The image shows the uniform shear caused by slip in the crystal. The slip planes are bright surfaces parallel to the horizontal plane. The sample was imaged with our STM in a topographic mode (sample bias = 240mV, tunneling current = 1.2nA).

$=14.2\times10^{-6}$, $\alpha_W = 4.5\times10^{-6}$, and ΔT=1337K(melting point of gold)-293K(room temperature) = 1044K, we obtain $\epsilon = 1.00\times10^{-2}$ which is an order of magnitude larger than the case of Au on glass. We speculate that this large strain combined with the sudden temperature change might have caused a catastrophic shearing of the crystal.

REFERENCES FOR CHAPTER 8

1 J.J. Gilman and W.G. Johnston, J. Appl. Phys. **29**, 877 (1958)

2 I.G. Greenfield and H.G.F. Wilsdorf, J. Appl. Phys. **32**, 827 (1961)

3 K. Reichelt and H.O. Lutz, J. Crystal Growth **10**, 103 (1971)

4 J.A. DeRose, T. Thundat, L.A. Nagahara, and S.M. Lindsay, Surface Sci. **256**, 102 (1991)

Chapter 9

SUMMARY OF CONCLUSIONS

- We have described the design and operation of a simple STM which functions reliably from room temperature to 4K. The STM is assembled without glues and solders and can be quickly and easily disassembled for repair or modification.

- Thermal evaporation of Au onto heated glass substrates is an extremely reliable technique for the production of films with large, atomically flat regions. We find that 80nm thick Au films evaporated onto glass substrates held at temperatures of 300C exhibit large faceted grains of about 250nm diameter. The tops of the grains are atomically flat with step-free terraces as large as 200nm x 200nm. The grains are separated by trenches 10-20nm deep and 50-100nm wide, leading to an overall rms surface roughness of 6nm or greater. In comparing the our films with the best reported results for gold films grown on mica, our films exhibit larger step-free, atomically flat regions, but have an average roughness that is greater than the Au-on-mica films. We find that mica is unreliable as a substrate, apparently because of the variable quality of commercial supplies.

- We fabricated small gold islands and pits on an atomically flat gold surface by a voltage pulse. The sequential STM images of the fabricated structures show that the area of the monolayer gold island decays linearly in time at room temperature in air.

- We have shown, by Monte Carlo simulation, that the linear decay of monolayer islands on metal surfaces arises from a competition among the rate of emission of adatoms by kink sites, the rate of absorption by an outer ledge, and the rate of reattachment to the home mesa. Linear decay is found when the distance to the outer absorbing ledge is more than 2 or 3 times the starting radius of the mesa, and it is rather insensitive to variations in the probability of reflection from the outer ledge.

- To measure the surface diffusion constant, the relaxation of the stepped gold surface toward equilibrium is observed. From the series of images showing moving monatomic steps, we obtain a diffusion constant of $6.2 \times 10^{-17} cm^2/sec$ for the clean samples, while the heavily contaminated sample yields 8.6×10^{-16} $cm^2/seconds$.

- With an STM, at room temperature in air, low angle grain boundaries and other dislocation arrays are observed in thermally stressed gold films evaporated on heated glass substrates. We find that these low angle grain boundaries move under an applied stress introduced either by handling the sample or by crashing an STM tip on the sample surface. From time lapse STM images, we also observe that the motion may slow to a stop, reverse direction, or show oscillatory behavior. These dynamic features usually accompany a deformation of a part of the sample.

- The STM was used to study discrete charging effects in small normal metal particles on substrates which are so flat that the particle shape can be clearly imaged with an STM. Our most successful recipe involves oxidized Pb on top of Au film evaporated on SiO_2. Small gold particles are prepared by thermal evaporation of a discontinuous film onto the PbOx-Au-SiO_2 substrate. The STM, operating in the range 4K-300K, both images the particles and performs I-V spectroscopy. We

showed I-V curves which exhibit a coulomb staircase at room temperature and a coulomb blockade at 83K.

APPENDIX

Appendix
Shop drawings for STM Body

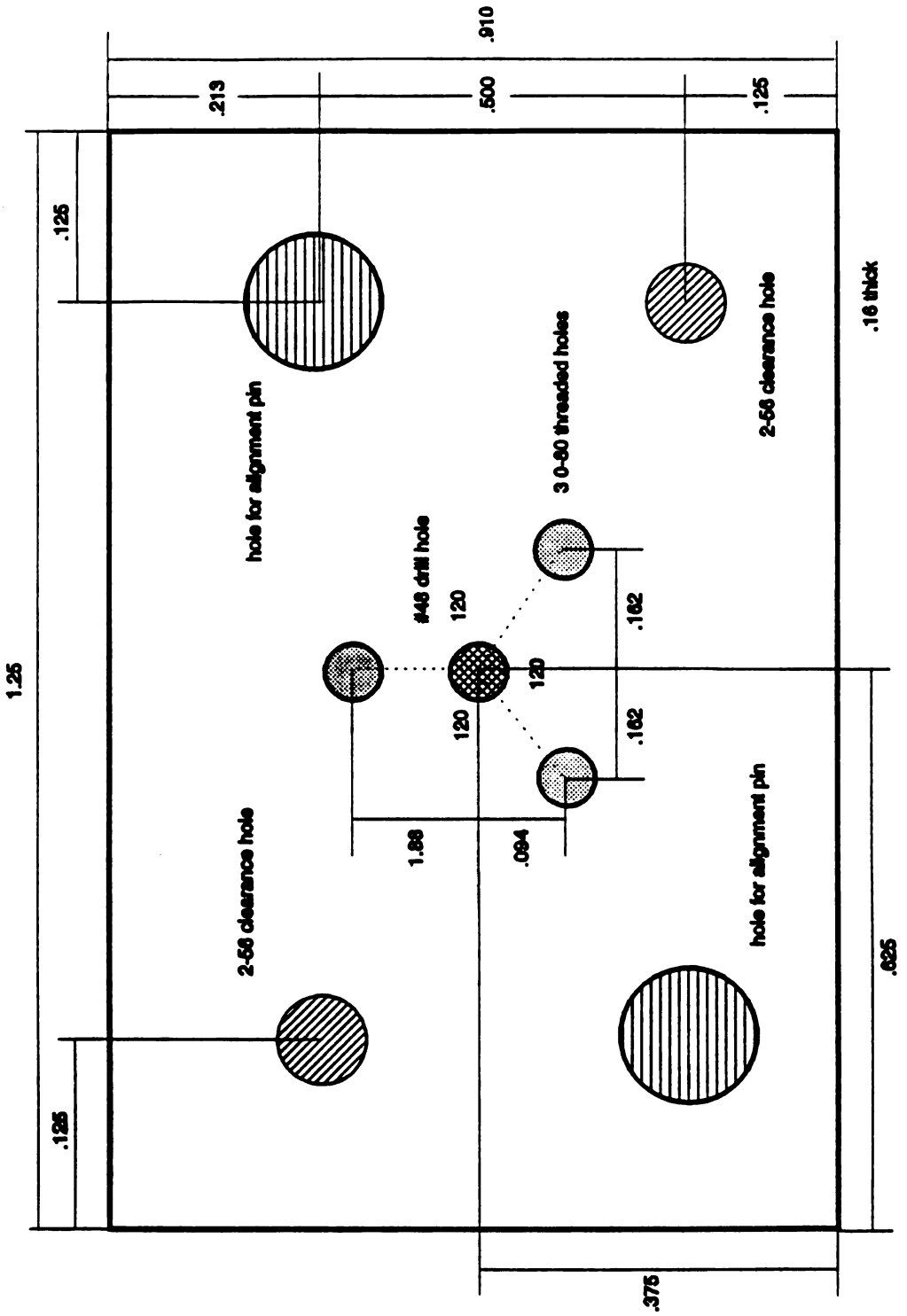

Figure A.1 STM bottom plate. Three 0-80 threaded holes near the center are for leveling screws which support the sample stage. An extra hole in the center is for a spring to hold the sample stage against the leveling screws. The units are inches.

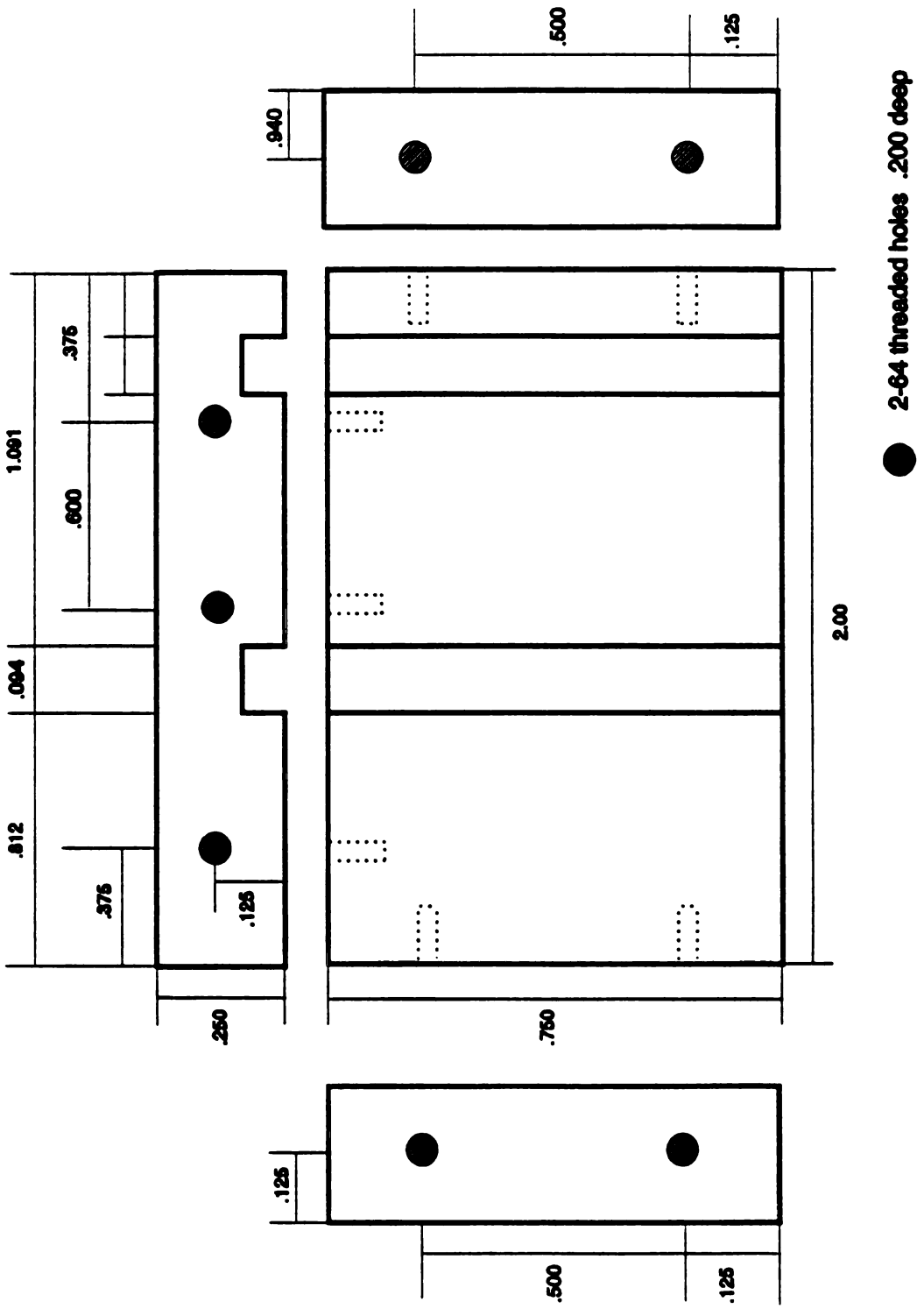

Figure A.2 STM right hand side plate. The plate on the left hand side is a mirror image of this plate.

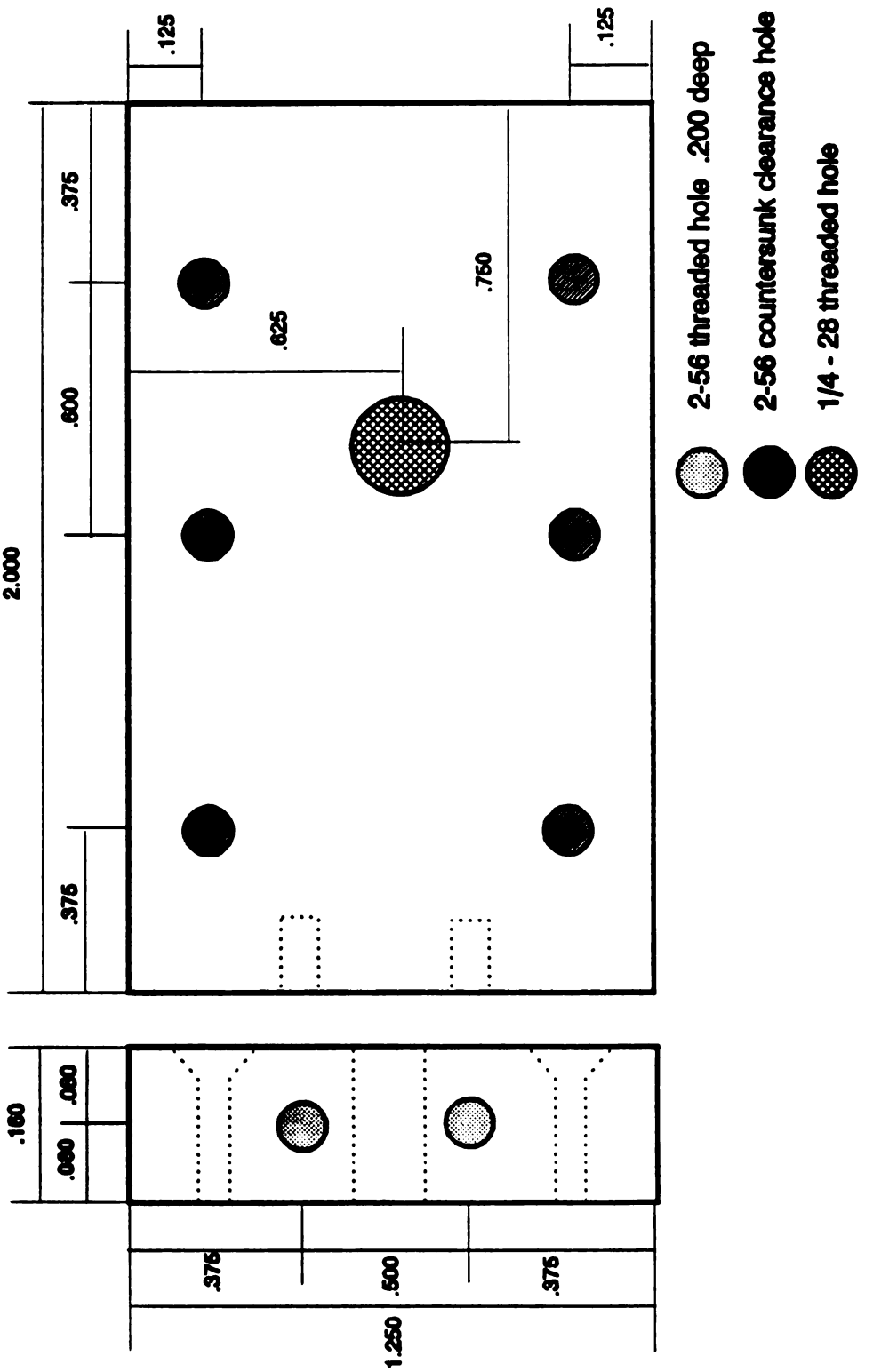

Figure A.3 STM back plate. The 1/4-28 threaded hole is for a thermometer. A thermometer is embedded inside the 1/4-28 bolt and screwed into this hole

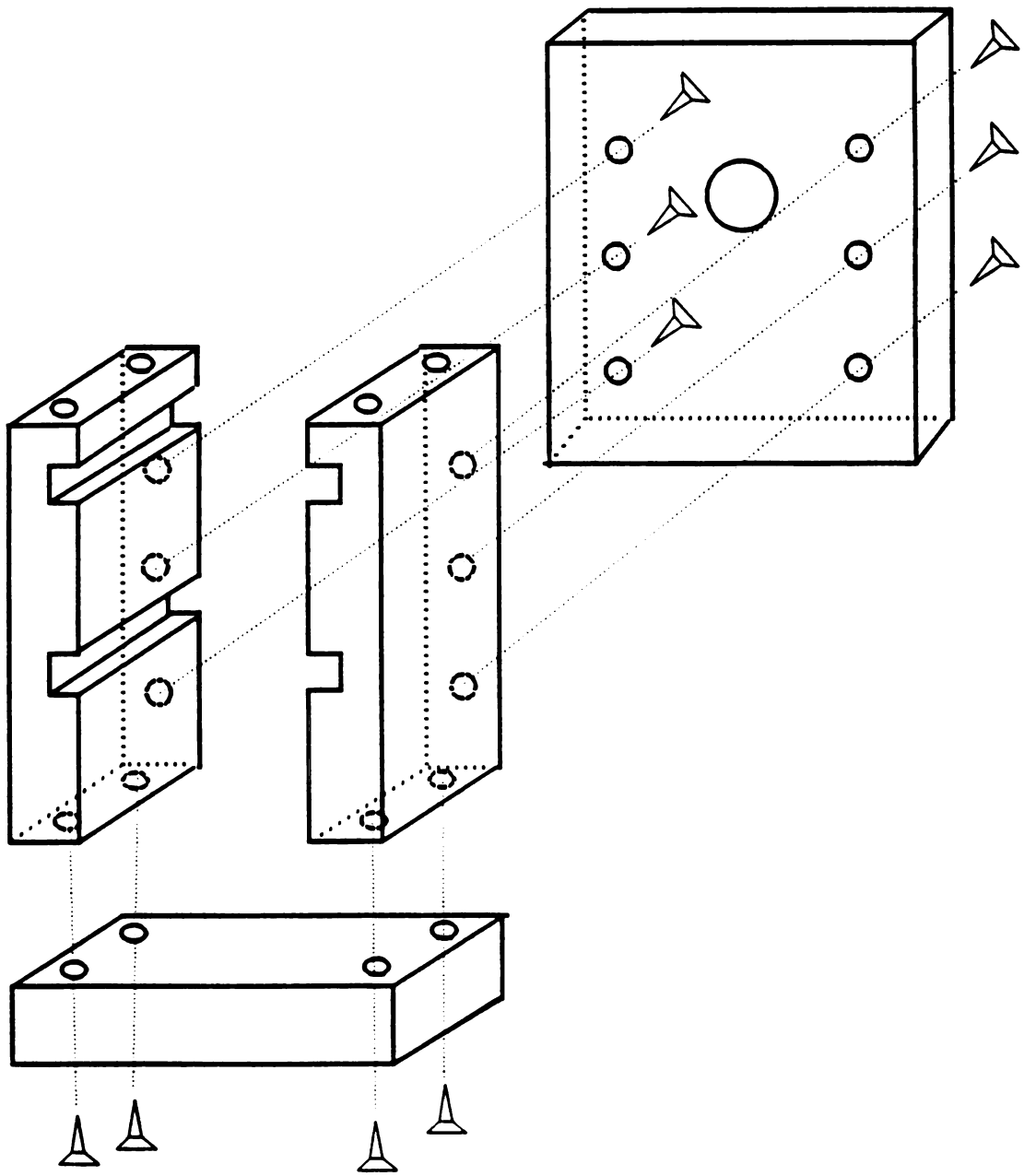

Figure A.4 The final assembly of the STM body.

B. List of Publications

B.1 "Simple, variable-temperature scanning tunneling microscope", M.A. Dubson and J. Hwang , Rev. Sci. Instrum. **63**(7), 1992 .....(described in chapter 2)

B.2 "Atomically flat gold films grown on hot glass", J. Hwang and M.A. Dubson, J. Appl. Phys. **72**(5), 1992 .....(described in chapter 3)

B.3 "The linear decay of islands on metal surfaces", M.A. Dubson, Martine Kalke, and Jeeseong Hwang (to be published in Phys. Rev. B) .....(described in chapter 5)

B.4 "STM observations of surface diffusion of gold on Au (111)", J. Hwang and M.A. Dubson (in preparation) .....(described in chapter 4)

B.5 "STM observations of dynamics of low-angle grain boundaries and dislocations in stressed thin gold films on glass substrates", J. Hwang and M.A. Dubson (in preparation) .....(described in chapter 6)

B.6 "An atomic view of mass transport by surface diffusion", M.A. Dubson, J. Hwang (in preparation)

Contributed Papers

B.7 "STM study of atomically flat Au on glass", J. Hwang and M.A. Dubson, Bull. Am. Phys. Soc. **37**, 112 (1992)

B.8 "STM study of small metal particles on flat substrates", J. Hwang and M.A. Dubson, Bull. Am. Phys. Soc. **35**, 505 (1991)